

学位論文

**Structure and Variability of Surface Layer Salinity  
in the Subtropical Pacific**

(太平洋亜熱帯域における表層塩分の構造と変動)

平成 28 年 7 月博士 (理学) 申請

東京大学大学院理学系研究科

地球惑星科学専攻

桂 将太

**Doctoral Dissertation**

**Structure and Variability of Surface Layer Salinity  
in the Subtropical Pacific**

**Shota Katsura**

**Department of Earth and Planetary Science**

**Graduate School of Science**

**The University of Tokyo**

**July 2016**

# Abstract

Salinity, along with temperature, is one of the most fundamental parameters in physical oceanography. The knowledge of the seasonal and interannual variations of salinity and their mechanisms is important not only for understanding air-sea heat and freshwater exchanges but also for accurate estimation of long-term salinity changes that likely reflect those of the hydrological cycle. In addition, salinity anomalies on isopycnal surfaces subducted in the subtropics are thought to propagate to the tropics and cause decadal climate variability through modulation of sea surface temperature there. Exploration of salinity variabilities on seasonal and interannual time scales had been possible only at limited regions due to the lack of salinity data, but recently became possible for most parts of the global ocean owing to the construction of Argo profiling float network. In this thesis, the structure and variability of the North Pacific Tropical Water (NPTW) and barrier layer (BL), which are representative surface salinity structure in the subtropical Pacific, were investigated mainly by analyzing Argo profiling float data.

Formation, subduction, and advection of NPTW, their interannual variability, and the associated mechanisms were investigated by using gridded Argo profiling float data and various surface flux data. The NPTW has two formation sites in the center of the North Pacific subtropical gyre, corresponding to two regional sea surface salinity maxima. Mixed layer salinity variations in these two NPTW formation sites were significantly different. While seasonal variation was prominent in the eastern formation site, interannual variation was dominant in the western site. The mixed layer salinity variation in the eastern site was controlled mainly by evaporation, precipitation, and entrainment of fresher water below the mixed layer, and was closely related to the seasonal variation of the mixed layer depth. In the western site, the effect of entrainment was small due to small vertical difference in salinity across the mixed layer base, and excess evaporation over precipitation was likely to be balanced

by eddy diffusion, whose variations may be related to the Pacific Decadal Oscillation. After subduction, denser NPTW formed in the eastern site dissipated quickly, while the lighter one formed in the western site was advected westward as far as the Philippines Sea, transmitting the interannual variation of salinity away from its formation region.

Seasonal and interannual variations of BL and its formation mechanism, possibly in relation to the tropical water (TW) subduction, in the subtropical North and South Pacific were investigated by using raw and gridded Argo profiling float data and various surface flux data, hydrographic section data from the World Ocean Circulation Experiment Hydrographic Programme, and the output data of an ocean general circulation model (OGCM). BLs detected by raw Argo profiles, which existed within the sea surface salinity (SSS) front located on the equator side of SSS maxima, were thickest and most frequent in winter and had a temporal scale around 10 days, indicating their transient nature. Subsurface salinification due to the subduction of TWs and surface freshening suggested as formation mechanism of BLs by previous studies were evaluated. High salinity water within BL was not directly associated with subduction of TWs. Meridional Ekman advection was dominant as the surface freshening process, but it could not explain the seasonal variation of BLs. Temporal scale of BLs was also too short for their growth during cooling period. These results strongly suggest that BLs in the subtropical Pacific are formed mainly through tilting of the SSS front due to the poleward Ekman flow near the sea surface. This idea is supported by dominant contribution of the meridional SSS gradient to the meridional sea surface density gradient within the SSS front and the correspondence between the seasonal variations of BL and isothermal layer depth. It was also confirmed by the analysis of an OGCM that the vertical shear of salinity advection within isothermal layers tends to occur where BLs are formed and that the vertical shear of flow results from that of ageostrophic one. On interannual time scale, the winter BL thickness in the North and South Pacific was related to the Pacific Decadal Oscillation and the El Niño-Southern Oscillation, respectively, through their influence on the intensity of trade winds controlling isothermal layer depth.

# Contents

<b>Abstract</b>	<b>i</b>
<b>1 General Introduction.....</b>	<b>1</b>
1.1 Salinity Variability and Its Implication.....	1
1.2 Hydrography in the Subtropical Pacific.....	3
1.2.1 Surface Circulation.....	3
1.2.2 Salinity Structure.....	4
1.3 Overview of This Thesis.....	5
<b>2 Formation and Subduction of North Pacific Tropical Water and Their Interannual Variability.....</b>	<b>14</b>
2.1 Introduction.....	14
2.2 Data and Method.....	15
2.2.1 Data.....	15
2.2.2 Mixed Layer Salinity Budget.....	16
2.3 Result.....	17
2.3.1 Mixed Layer Salinity Variation.....	17
2.3.2 Mixed Layer Salinity Budget.....	18
2.3.3 Subduction of NPTW.....	20
2.4 Discussion.....	21

2.5 Summary .....	24
<b>3 Seasonal and Interannual Variability of Barrier Layers in the Subtropical Pacific and Their Formation Mechanism.....</b>	<b>46</b>
3.1 Introduction.....	46
3.2 Data and Method.....	48
3.3 Seasonality and Persistence of Barrier Layer .....	50
3.4 Formation Mechanism of Barrier Layer .....	52
3.4.1 Contribution of Tropical Water Subduction .....	52
3.4.2 Surface Freshening.....	53
3.4.3 Possibility of BL Formation through the Tilting of SSS Front.....	55
3.4.4 Verification of the Tilting of SSS Front by a High Resolution OGCM .....	56
3.5 Interannual Variability of Winter Barrier Layer .....	58
3.6 Discussion .....	60
3.7 Summary .....	60
<b>4 General Conclusion and Discussion.....</b>	<b>88</b>
4.1 Conclusion .....	88
4.2 Future Works .....	90
<b>Appendix Residual of the Mixed Layer Salinity Budget with the Usage of Various Freshwater Flux Data.....</b>	<b>93</b>
<b>Acknowledgements .....</b>	<b>95</b>
<b>References.....</b>	<b>97</b>

# Chapter 1

## General Introduction

### 1.1 Salinity Variability and Its Implication

Salinity, along with temperature, is one of the most fundamental parameters in physical oceanography. In open oceans, its variations are mostly controlled by surface processes, especially the surface freshwater flux, and its long-term changes reflect those in climate and hydrological cycle. At the same time, salinity also determines water density and controls the ocean circulation, particularly at high latitudes where water temperature is low. The knowledge of the salinity changes is important for better understanding of climate and hydrological cycle, particularly because evaporation and precipitation, which occur mostly over the ocean (Schmitt 1995), have not been fully quantified.

Long-term salinity changes have been investigated by previous studies despite observations of salinity in the past limited compared to those of temperature. Wong et al. (1999) and Curry et al. (2003) contrasted the World Ocean Circulation Experiment Hydrographic Program (WHP) section data around 1990 with the historical data roughly twenty years earlier to indicate freshening of intermediate waters characterized by salinity minimum and salinification of tropical waters characterized by salinity maximum in the Pacific, Indian, and Atlantic Oceans. Their results implied intensification of the global hydrological cycle. Similar intensification of salinity contrast between the subtropical and subarctic world ocean has been presented by comparing Argo profiling float data after 2000 and historical measurements before 2000 (Boyer et al. 2005; Hosoda et al. 2009; Roemmich and Gilson 2009; Durack and Wijffels 2010; Helm et al. 2010). Isopycnal freshening in the North Pacific permanent thermocline was also reported through comparison between the Argo and WHP data (Ren and Riser 2010).

In addition to the long-term changes, salinity variations on shorter time scales and their mechanisms have been explored using available data at limited locations. At the station ALOHA in the subtropical North Pacific, monthly shipboard observations during 1991–97 showed freshening of upper thermocline water in association with a decadal increase in net freshwater flux (Lukas 2001). In the tropics, mooring observations under the Tropical Ocean-Global Atmosphere Coupled Ocean-Atmosphere Response Experiment (TOGA-COARE) and Pilot Research Array in the Tropical Atlantic (PIRATA) projects made it possible to investigate seasonal to interannual variations of salinity in the western equatorial Pacific (Sprintall and McPhaden 1994; Feng et al. 1998; Cronin and McPhaden 1998) and the tropical Atlantic (Segschneider et al. 2000; Foltz et al. 2004), respectively. Observations along repeat hydrographic sections and shipping tracks have also clarified broad scale salinity variations and their zonal differences in each tropical ocean (Delcroix and Hénin 1991; Qiu and Joyce 1992; Dessier and Donguy 1994; Donguy and Meyers 1996; Delcroix et al. 1996; Delcroix and Picaut 1998).

In recent years, such exploration of salinity fields has become possible for most parts of the global upper ocean, owing to the accumulation of Argo profiling float data since 2000 (e.g., Roemmich et al. 2001). Ren and Riser (2009) used these data to estimate the mixed layer salinity (MLS) budget in the northeastern North Pacific where precipitation exceeds evaporation, and pointed out the importance of entrainment of saltier water below the mixed layer for the increase of MLS in fall to winter. Similar analyses demonstrated that not only entrainment but also horizontal advection and sea ice processes are important for MLS variations in the Southern Ocean (Dong et al. 2009; Ren et al. 2011). Motivated further by the recent launches of the Soil Moisture and Ocean Salinity (SMOS) satellite with Multicolor InfraRed Alerting Sensor (MIRAS) by the European Space Agency (Kerr et al. 2001) and the Satellite de Aplicaciones Científicas-D (SAC-D) satellite with Aquarius sensor by the National Aeronautics and Space Administration (NASA; Le Vine et al. 2007), upper-ocean salinity variability has attracted increasing attention, which led to the initiation of intensive studies such as the ongoing Salinity Processes in the Upper Ocean Regional Study project by NASA (e.g., Lindstrom et al. 2015). Clarification of the seasonal and interannual variations of salinity and their mechanisms is important not only for understanding air-sea heat and freshwater exchanges but also for accurate estimation of

long-term salinity changes.

## **1.2 Hydrography in the Subtropical Pacific**

### **1.2.1 Surface Circulation**

Surface circulation in subtropics is characterized by anticyclonic subtropical gyre forced by anticyclonic wind stress curl (Fig. 1.1). Within the subtropical gyre, water is subducted from the seasonally-varying surface layer to the permanent thermocline due to Ekman pumping, and then water is advected along isopycnal surfaces by gyre circulation (Fig. 1.2). In the North Pacific, subducted water is advected southwestward by the North Equatorial Current. When it reaches the Philippine coast, a part of it is transported northward by the Kuroshio and spreads over the subtropical gyre, while the other part is advected southward by the Mindanao Current to the equatorial Pacific. One part of the latter passes the Celebes Sea (Fine et al. 1994) and is then advected to the Indian Ocean (Ffield and Gordon 1992) or back to the North Pacific (Lukas et al. 1991; Kashino et al. 1996). In the South Pacific, subducted water is advected northwestward by the South Equatorial Current, reaching equatorial region directly.

It has been hypothesized that through such subduction and advection processes, temperature anomalies in the subtropics propagate along isopycnal surfaces to the tropics, modulate sea surface temperature (SST) there, and cause decadal to inter-decadal climate variability (Gu and Philander 1997). Temperature anomalies on isopycnal surfaces are associated with density-compensated salinity anomalies. They are called spiciness anomalies, based on the idea of spiciness (Munk 1981), and advected as a passive tracer after subduction. Evolution and propagation of spiciness anomalies from the subtropics to the tropics and its impact on the atmospheric condition through modulation of SST in the tropics have been investigated by modeling studies (e.g., Nonaka and Sasaki 2007; Schneider 2004).

To separate spiciness anomalies and the vertical displacement of isopycnal surface governed by planetary waves (Liu 1999) from subsurface temperature anomalies, it is necessary to know the variability of density structure and hence that of salinity structure. In the North Pacific, downward and equatorward propagation of decadal temperature anomalies were reported based on the basin-wide network of expendable bathythermograph data (Deser et al. 1996; Schneider et al. 1999). However, due to the

lack of salinity data, it was impossible to divide observed temperature anomalies into spiciness anomalies on isopycnal surfaces and those caused by the vertical displacement of isopycnal surfaces. Recently, observation by Argo profiling floats makes it possible to detect the propagation of spiciness anomalies on isopycnal surfaces (Fig. 1.3; Sasaki et al. 2010; Kolodziejczyk and Gaillard 2012). To further investigate the formation and propagation of these observed spiciness anomalies and their impact on SST in the tropical region, the knowledge of the structure and variability of surface layer salinity in the subtropics is vital.

### **1.2.2 Salinity Structure**

In the subtropics where evaporation exceeds precipitation, surface layer salinity is higher than other regions. Sea surface salinity (SSS) maxima lie on the center of subtropical gyre in each ocean basin (Fig. 1.4). Water subducted from these SSS maxima forms subsurface salinity maximum called Tropical Water (TW), which is the most characteristic salinity structure in the subtropics. After subduction, TW is advected and spread over the subtropical gyre.

In the subtropical Pacific, the North Pacific Tropical Water (NPTW) and the South Pacific Tropical Water (SPTW) are formed in each hemisphere and subduct. After subduction, NPTW and SPTW are advected equatorward and westward to the tropics by the North Equatorial Current and the South Equatorial Current, respectively (Fig. 1.5), transmitting spiciness anomalies from the subtropical regions to the tropical region. They can also affect the stratification in the downstream regions, such as the western tropical Pacific (Lukas and Lindstrom 1991). NPTW advected northward by the Kuroshio may influence stratification in the subtropical gyre, especially the formation of mode waters in the Kuroshio extension region.

Another important salinity structure in the subtropics is barrier layer (BL; Sprintall and Tomczak 1992). BL is the layer between the bases of mixed layer and isothermal layer defined in terms of potential density and temperature, respectively, when the former is shallower than the latter due to shallow salinity stratification (Fig. 1.6; Lukas and Lindstrom 1991). When BL exists, the difference of temperature between the mixed layer and the underlying layer is small, which obstructs mixed layer cooling through entrainment of lower-layer water (Godfrey and Lindstrom 1989; Lukas and Lindstrom 1991). In addition, momentum flux from the atmosphere to the ocean is

trapped within shallow mixed layer associated with barrier layer, resulting in accelerated flow within mixed layer (Vialard and Delecluse 1998a). Thus, BL acts as ‘barrier’ of heat and momentum flux from the sea surface to the ocean interior and has been thought to affect air-sea interaction.

In the subtropical Pacific, BLs are distributed in winter in association with SSS fronts lying on the equatorward side of SSS maxima, that is, NPTW and SPTW formation regions (Fig. 1.7; Sato et al. 2004; 2006). They can influence the formation of spiciness anomalies by modulating SST. Since the subtropical Pacific is characterized by net freshwater loss, precipitation is not responsible for the BL formation there. It has been suggested that the subduction of NPTW and SPTW across SSS fronts contributes to the BL formation in the North and South subtropical Pacific, respectively (Sato et al. 2004; 2006). Thus, evaluating the contribution of TW subduction to subtropical BLs is important for understanding its impacts on downstream regions.

Mean property of NPTW and SPTW and their formation rates were investigated based on climatological data and chlorofluorocarbon data from the World Ocean Circulation Experiment Hydrographic Programme, respectively (O’Connor et al. 2002; 2005). However, because of insufficiency of salinity observation, their variability could not be investigated except along meridional repeat hydrographic sections in their downstream regions (Kessler 1999; Suga et al. 2000). Thus, their variability in formation region and their subduction and advection processes had been poorly examined as well as their contribution to the formation of subtropical BLs. Recent accumulation of Argo profiles makes it possible to investigate not only variability of North Atlantic Tropical Water and SPTW in their formation regions and their subduction and advection processes (Zhang and Qu 2014; Qu et al. 2016) but also interannual variability of BLs in the tropical Pacific (Qu et al. 2014). It motivates me to study NPTW and BLs in the subtropical Pacific using Argo profiling float data for better understanding of the structure and variability of subtropical surface layer salinity.

### **1.3 Overview of This Thesis**

The aim of this thesis is to clarify the structure and variability of surface layer salinity in the subtropical Pacific by investigating those of NPTW and BLs in the subtropical North and South Pacific mainly based on Argo profiling float data. In

Chapter 2, formation, subduction and advection of NPTW and their interannual variability are investigated. In Chapter 3, seasonal and interannual variability of subtropical BLs in the North and South Pacific are investigated, and their formation mechanism as well as the contribution of TW subduction is explored. General conclusion and discussion are given in Chapter 4. Contents of Chapter 2 and a part of Chapter 3 have been published as Katsura et al. (2013) and Katsura et al. (2015), respectively.

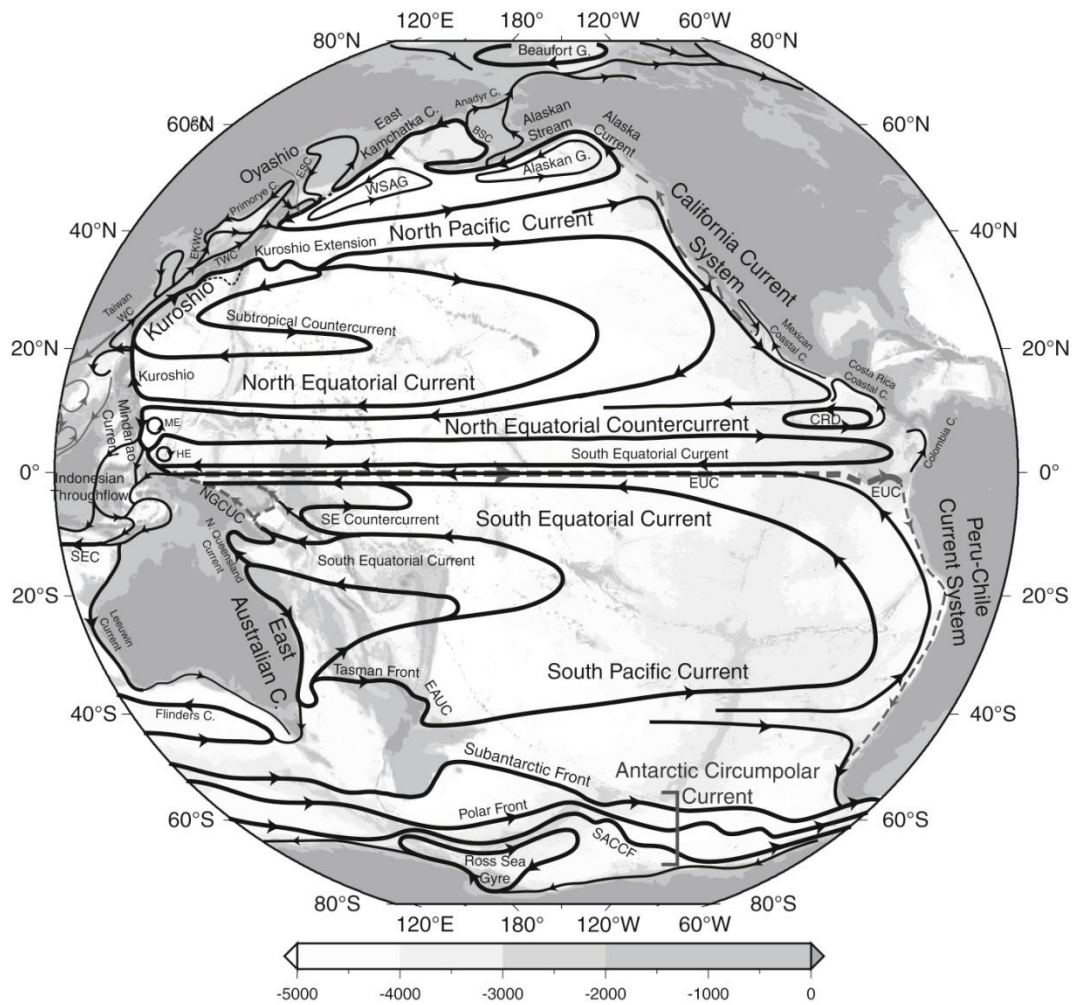


Fig. 1.1. Schematic of surface circulation in the Pacific Ocean. From Talley et al. (2011). Reprinted from *Descriptive Physical Oceanography: An Introduction*, Sixth edition, Lynne D. Talley, George L. Pickard, William J. Emery, and James H. Swift, Chapter 10 – Pacific Ocean, 304p, Copyright 2011, with permission from Elsevier.

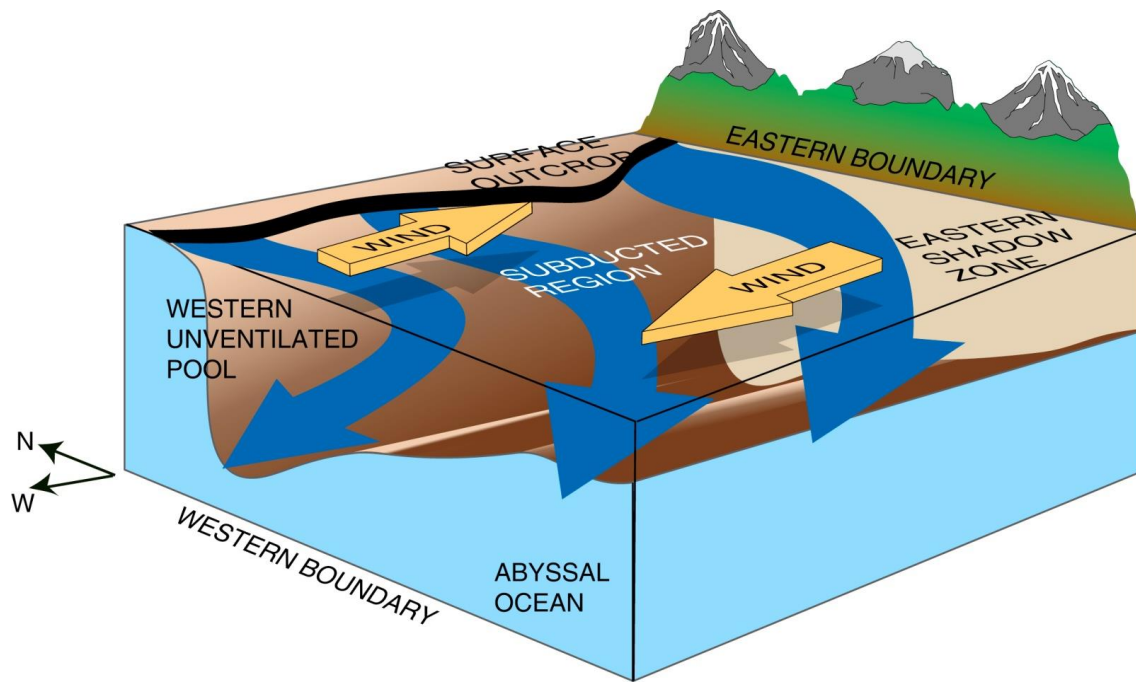


Fig. 1.2. Schematic of subduction in the Northern Hemisphere. From Talley et al. (2011). Reprinted from *Descriptive Physical Oceanography: An Introduction*, Sixth edition, Lynne D. Talley, George L. Pickard, William J. Emery, and James H. Swift, Chapter 7 – Dynamical Processes for Descriptive Ocean Circulation, 216p, Copyright 2011, with permission from Elsevier.

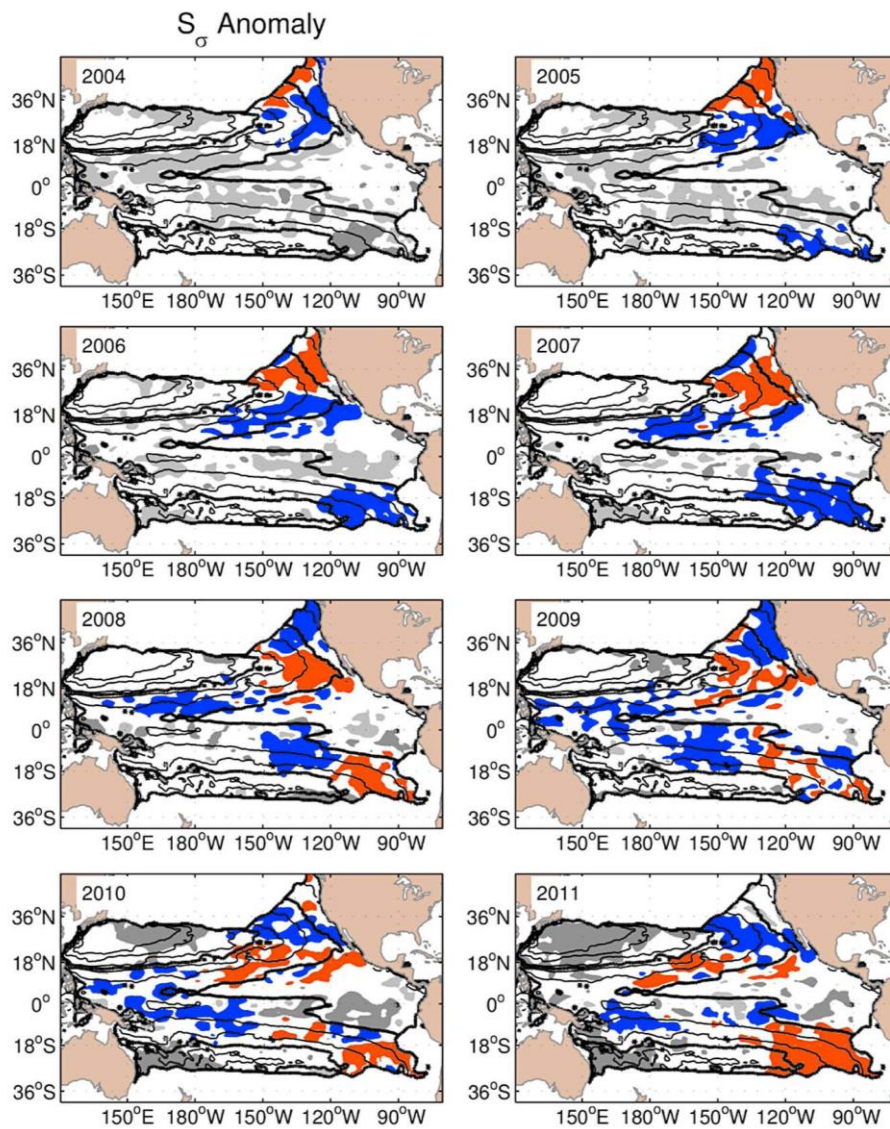


Fig. 1.3. Mean annual isopycnal negative (dark gray and blue) and positive (light gray and red) salinity anomalies greater than  $0.03$  on the isopycnal surface  $\sigma_\theta = 25.5 \text{ kg m}^{-3}$ . The thick black streamlines represent the  $5.5$  and  $8 \text{ m}^2 \text{ s}^{-2}$  isopleths. From Kolodziejczyk and Gaillard (2012).

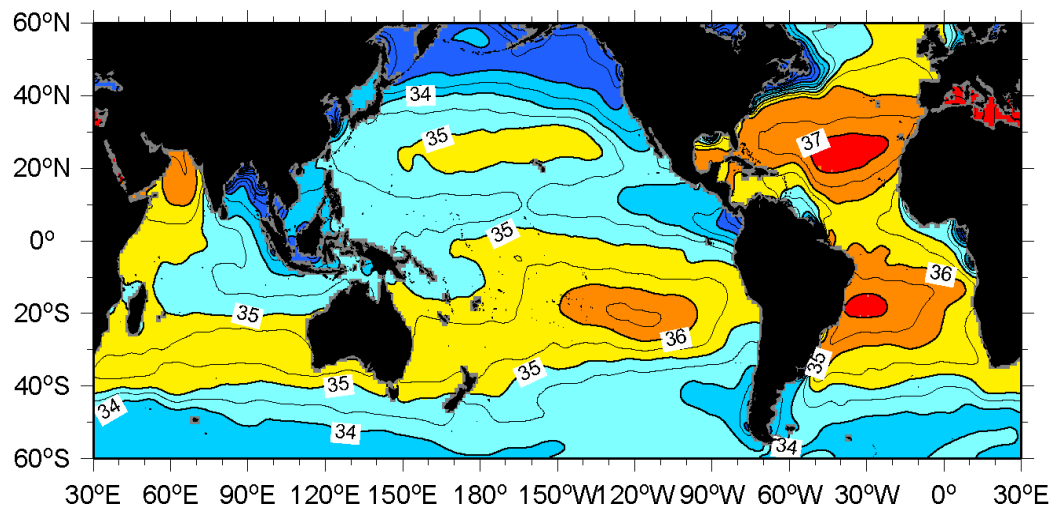


Fig. 1.4. Mean sea surface salinity distribution based on World Ocean Atlas 2001.

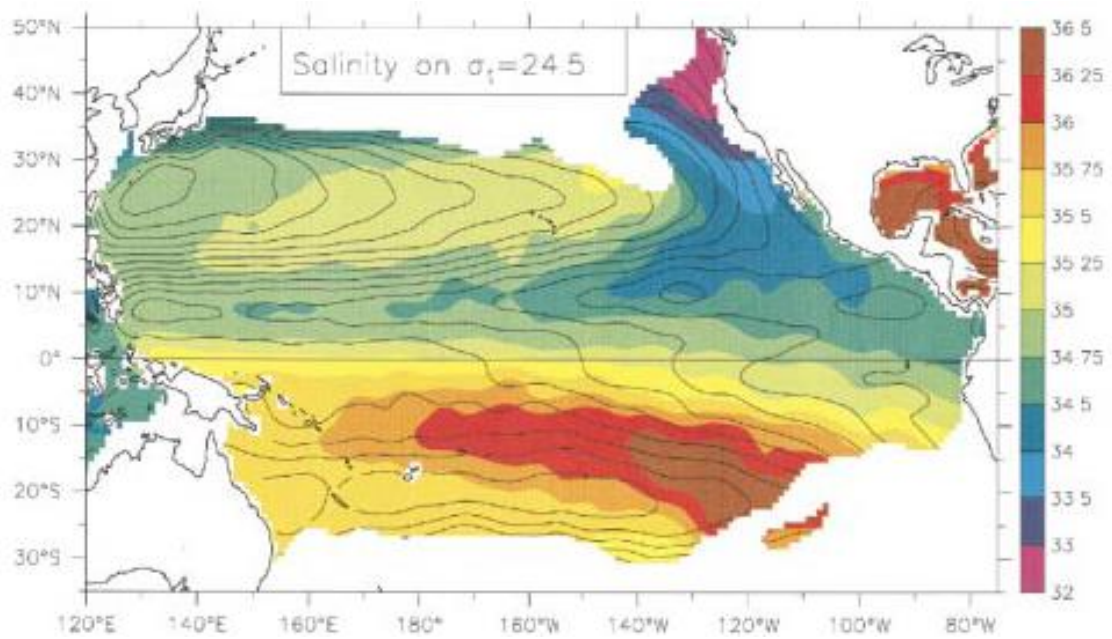


Fig. 1.5. Mean salinity (color) and geostrophic streamlines relative to 1000 dbar (contour) on the surface  $\sigma_\theta = 24.5 \text{ kg m}^{-3}$  from the Levitus et al. (1994) World Ocean Atlas. From Kessler (1999). ©American Meteorological Society. Used with permission.

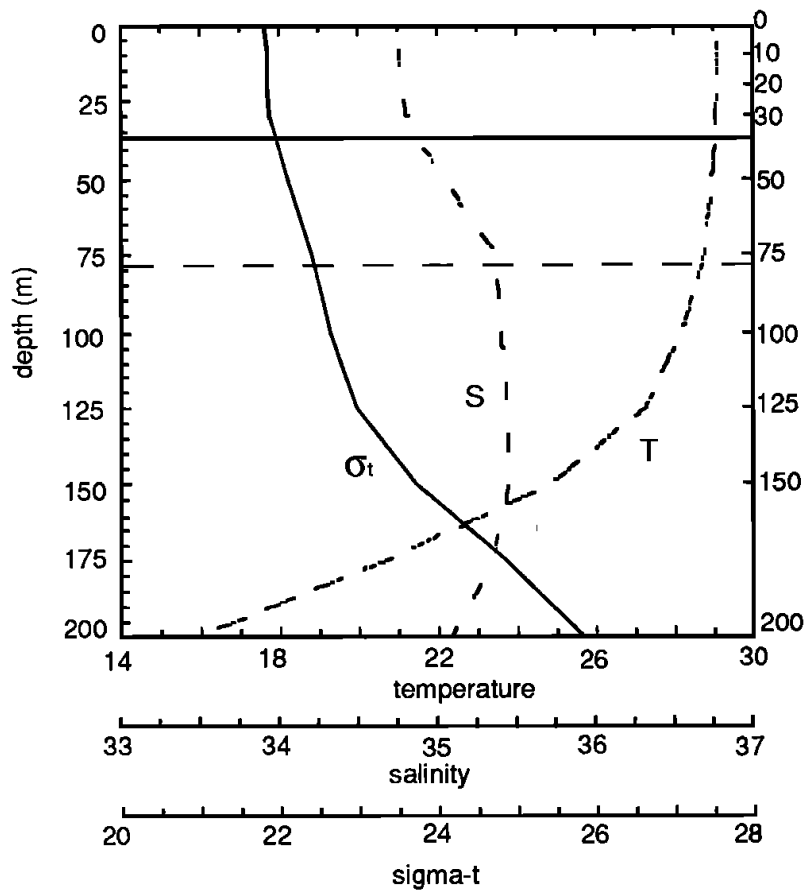


Fig. 1.6. Vertical profile of temperature, salinity, and  $\sigma_t$  at 158.5°E, 2.5°S during February-April from the Levitus (1982) data set. (Standard depth levels of the Levitus data are given on the right axis.) Horizontal solid and dashed lines indicate mixed and isothermal layer depths, respectively, and the layer between them is referred to as the barrier layer. From Sprintall and Tomczak (1992).

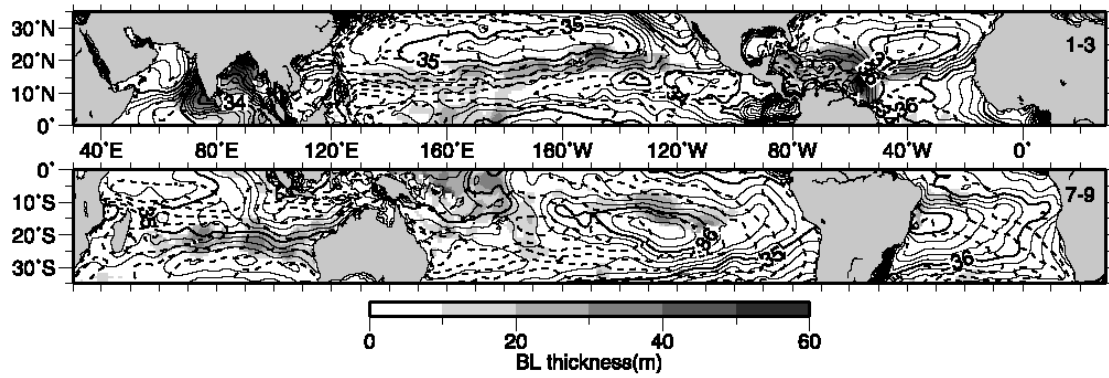


Fig. 1.7. Distribution of barrier layer thickness (shading), sea surface salinity (solid contour), and dynamic height at 50 dbar (dashed contour) in the Northern Hemisphere during January-March (upper panel) and in the Southern Hemisphere during July-September (lower panel) based on World Ocean Atlas 2001. From Sato et al. (2006).

## **Chapter 2**

# **Formation and Subduction of North Pacific Tropical Water and Their Interannual Variability**

### **2.1 Introduction**

North Pacific Tropical Water (NPTW) is a water mass characterized by surface ocean salinity maximum. NPTW is formed at the sea surface in the subtropics where evaporation exceeds precipitation (Cannon 1966), and is then subducted and advected westward by the North Equatorial Current as a subsurface salinity maximum (Tsuchiya 1968; Qu et al. 1999). When NPTW reaches the Philippine coast (Li and Wang 2012), it is split into two parts. One part is advected northward by the Kuroshio, while the other part flows southward in the Mindanao Current. The latter part partly passes the Celebes Sea (Fine et al. 1994) and then flows into the Indian Ocean (Field and Gordon 1992) or back to the North Pacific (Lukas et al. 1991; Kashino et al. 1996). When NPTW reaches the equatorial region carrying salinity or spiciness anomalies from the formation region in the subtropics, it can influence the sea surface temperature variability through the formation of barrier layer (Lukas and Lindstrom 1991) and climate variability in the Pacific (Gu and Philander 1997; Schneider et al. 1999; Sasaki et al. 2010). NPTW carried northward by the Kuroshio can affect the salinity/spiciness distribution in the permanent pycnocline of the subtropical gyre through the formation of mode waters in the Kuroshio Extension region (Oka 2009; Oka et al. 2011; Oka and Qiu 2012).

Long-term variation of NPTW was investigated by Suga et al. (2000), who analyzed repeat hydrographic section data along 137°E during 1967–1995, which is

located to the west (downstream) of the NPTW formation region. They demonstrated salinification of NPTW in association with the climate regime shift in the 1970s (Nitta and Yamada 1989; Trenberth 1990) that is characterized by a southward shift and intensification of the Aleutian Low in winter. More specifically, salinity and thickness of NPTW in the northern part of 137°E increased, while only salinity decreased in the southern part. By using limited surface flux data, Suga et al. (2000) argued that the southern salinification is possibly due to the changes of evaporation over precipitation and Ekman salt convergence in the NPTW formation region, while the northern one may be due to the increase of the NPTW formation rate in the formation region. Since climatological stream function implies that the northern (southern) part of NPTW at 137°E is formed in the western (eastern) site of the formation region, the different pattern of NPTW change within the 137°E section in the 1970s suggests that the NPTW signals varied between the western and eastern sites of their formation region.

In this study, seasonal and interannual variations of NPTW in the two sites of its formation region and their mechanisms are investigated using Argo data and the latest surface flux data. Also explored is how NPTW is subducted and advected to the downstream as the subsurface salinity maximum, transmitting salinity anomalies generated in the formation region. The results of this chapter are important for understanding not only air-sea interaction but also sea surface salinity (SSS) variations that are now continuously monitored by the SMOS/MIRAS and SAC-D/Aquarius satellites. The data and method are described in Sec. 2.2. Variations of NPTW in its formation region and after subduction as well as their mechanism are examined in Sec. 2.3. The NPTW formation mechanism and its zonal difference between the western and eastern sites of the formation region are further discussed in Sec. 2.4. Summary is given in Sec. 2.5.

## **2.2 Data and Method**

### **2.2.1 Data**

Monthly mean temperature and salinity data based on Argo profiling float, moored buoy, and shipboard observations, named MOAA\_GPV (Hosoda et al. 2008), in 2003–11 were used. This dataset was prepared by optimally interpolating the observed temperature and salinity anomalies from the World Ocean Atlas 2001 climatology (Conkright et al. 2002) onto  $1^\circ \times 1^\circ$  grid points at each standard depth. In

this study, the temperature and salinity data between 10 and 2000 dbar at each grid point were vertically interpolated at an interval of 1 dbar using the Akima spline (Akima 1970). The analysis period is determined by the fact that the interpolation error of MOAA\_GPV salinity in the subtropical North Pacific decreased rapidly after 2001 and stayed small after 2003 corresponding to the improved Argo float coverage (Fig. 2.1).

Evaporation from the Objectively Analyzed air-sea Heat Fluxes project (Yu and Weller 2007; Yu et al. 2008), precipitation from the Climate Prediction Center Merged Analysis of Precipitation (CMAP; Xie and Arkin 1996; 1997), and wind stress from the National Centers of Environmental Prediction (NCEP; Kistler et al. 2001), whose horizontal resolution is  $1^\circ \times 1^\circ$ ,  $2.5^\circ \times 2.5^\circ$ , and  $1.875^\circ \times \sim 2^\circ$ , respectively, were also used. Sea surface height data from the Archiving, Validation, and Interpretation of Satellite Oceanographic Data (AVISO) at  $0.25^\circ \times 0.25^\circ$  grid were also used. These data for each month from 2003 through 2011 were linearly interpolated onto the same grid points as MOAA\_GPV, after averaging the daily data from NCEP and AVISO for each month.

It should be mentioned that the analysis of this study was repeated using the evaporation data from NCEP and the precipitation data from NCEP and the Global Precipitation Climatology Project (Huffman et al. 1997; Adler et al. 2003). The results with the usage of these freshwater flux data were not significantly different, as discussed in Sec. 2.4.

### 2.2.2 Mixed Layer Salinity Budget

To investigate the mechanism of mixed layer salinity (MLS) variation, the budget equation of Ren and Riser (2009) was used;

$$\frac{\partial S}{\partial t} = \frac{(E - P)S}{h_m} - \mathbf{u}_e \cdot \nabla S - \mathbf{u}_g \cdot \nabla S - \frac{w_e \Delta S}{h_m}, \quad (2.1)$$

where  $S$  is MLS,  $t$  is time,  $E$  is evaporation,  $P$  is precipitation,  $h_m$  is mixed layer depth (MLD),  $\mathbf{u}_e$  is Ekman velocity,  $\mathbf{u}_g$  is geostrophic velocity,  $w_e$  is entrainment velocity through the mixed layer base,  $\nabla$  is the horizontal differential operator, and  $\Delta S$  is the salinity difference between the mixed layer base and 20 dbar below (former minus latter; e.g., Hayes et al. 1991). Here, MLD at each grid point was determined as the

depth at which potential density ( $\sigma_\theta$ ) increases by  $0.125 \text{ kg m}^{-3}$  from the 10-dbar depth (Levitus 1982).

Ekman velocity  $\mathbf{u}_e$  was estimated from wind stress data as

$$\mathbf{u}_e = \frac{1}{\rho_0 f h_m} (\tau^y, -\tau^x), \quad (2.2)$$

where  $\tau^x$  and  $\tau^y$  are zonal and meridional wind stresses (positive eastward and northward),  $f$  is the Coriolis parameter, and  $\rho_0$  is the reference density of seawater, taken to be  $1025 \text{ kg m}^{-3}$ . Geostrophic velocity  $\mathbf{u}_g$  was calculated from sea surface height data assuming geostrophy.

Entrainment velocity  $w_e$  was estimated as

$$w_e = \left( \frac{\partial h_m}{\partial t} + \nabla \cdot h_m \mathbf{u} \right) H \left( \frac{\partial h_m}{\partial t} + \nabla \cdot h_m \mathbf{u} \right), \quad (2.3)$$

where  $\mathbf{u}$  is the sum of geostrophic and Ekman velocity, and  $H$  is the Heaviside step function,

$$H(x) = \begin{cases} 1, & x \geq 0 \\ 0, & x < 0 \end{cases}. \quad (2.4)$$

Here, the net positive entrainment velocity is only considered because detrainment does not affect the property of mixed layer.

## 2.3 Result

### 2.3.1 Mixed Layer Salinity Variation

The mean SSS distribution in the North Pacific during 2003–11 shows a maximum exceeding 35.0 in the subtropics at  $20^\circ\text{--}30^\circ\text{N}$ ,  $155^\circ\text{E}\text{--}135^\circ\text{W}$  (Fig. 2.2a). NPTW is formed in this region as a winter surface mixed layer with high salinity (Cannon 1966; Suga et al. 2000; O'Connor et al. 2002). A further inspection of Fig. 2.2a reveals two separate SSS maxima exceeding 35.35 centered at  $25^\circ\text{N}$ ,  $180^\circ$  and  $27^\circ\text{N}$ ,  $155^\circ\text{W}$ . The double SSS maxima are also seen in the surface salinity maps of previous works (e.g.,

Suga et al. 2000; 2004; O'Connor et al. 2002; Delcroix et al. 2005). The double maxima are located just to the north/northwest of those of evaporation minus precipitation (E-P) (Fig. 2.2b). These double E-P maxima have different evaporation and precipitation contributions; the western maximum collocates with the evaporation maximum, while the eastern one corresponds to low precipitation and relatively high evaporation (Figs. 2.2c and 2.2d). This difference suggests that the salinity variations and their mechanisms may be distinct between the western and eastern sites of the NPTW formation region.

To investigate the regional difference in the NPTW variation around the formation region, four boxes were selected in association with the double SSS and E-P maxima (Fig. 2.2): northwestern (NW) box ( $21^{\circ}$ – $28^{\circ}$ N,  $165^{\circ}$ E– $172^{\circ}$ W), northeastern (NE) box ( $24^{\circ}$ – $30^{\circ}$ N,  $165^{\circ}$ – $140^{\circ}$ W), southwestern (SW) box ( $15^{\circ}$ – $20^{\circ}$ N,  $165^{\circ}$ E– $170^{\circ}$ W) and southeastern (SE) box ( $16^{\circ}$ – $24^{\circ}$ N,  $150^{\circ}$ – $125^{\circ}$ W). For each box, MLS was calculated for each month by averaging salinities at all  $1^{\circ} \times 1^{\circ}$  grid points within the box from the sea surface to MLD.

The obtained MLS variations were significantly different between the two SSS-maximum boxes (Figs. 2.3a and 2.3b). Interannual variation was dominant in the NW box, while seasonal change was prevalent in the NE box. MLS in the NE box was lowest in late winter around March and highest in late summer around September–October almost every year (Figs. 2.3b and 2.4b). The MLS in the NW box was not significantly different among months, although semiannual variation is discernible (Figs. 2.3a and 2.4a). Its interannual variation was characterized by a rapid increase of more than 0.2 in 2008–2010.

MLS in the SW and SE boxes (Figs. 2.3c and 2.3d) showed similar variations to the NW and NE boxes, respectively. MLS in the SE box changed seasonally, being lowest around March and highest in November (Fig. 2.4d). In the SW box (Fig. 2.3c), interannual variation was dominant as in the NW box, and MLS increased rapidly in 2007–2009, preceding that in the NW box by about one year. MLS in this box also changed seasonally, being highest in December and lowest in May on the seasonal average (Fig. 2.4c).

### **2.3.2 Mixed Layer Salinity Budget**

To investigate the mechanism of MLS variation in each box, variations of the

terms in Eq. (2.1) were estimated. In the NE box, the rate of change in MLS on the left hand side of Eq. (2.1) and the sum of the forcing terms on the right hand side of Eq. (2.1) corresponded well to each other in terms of amplitude and phase, showing a high correlation both on the full time series (coefficient  $R = 0.68$ ; Fig. 2.5a) and on the seasonal average ( $R = 0.85$ ; Fig. 2.5b). The effect of Ekman and geostrophic advection was small due to the small horizontal salinity gradient in the SSS-maximum area, and the variation of MLS was mainly forced by vertical processes, that is, evaporation, precipitation, and entrainment (Figs. 2.5c and 2.5d). In this box, evaporation almost always exceeded precipitation. The excess evaporation increased MLS during the warming period from March through September, when the mixed layer shoaled and then stayed shallow (Fig. 2.6b). On the other hand, during the cooling period from October through February when the mixed layer deepened, the effect of entrainment of underlying fresher water into the mixed layer exceeded that of the excess evaporation, decreasing MLS. Thus, MLS fluctuated in association with MLD, being highest (lowest) in September–October (March) when the mixed layer was shallow (deep), as demonstrated in Fig. 2.4b. Such an MLS variation and its budget are contrasted with those in the subarctic North Pacific (Ren and Riser 2009), where salinity increases with depth and, resultantly, MLS is highest (lowest) in March–April (September–October).

In the NW box, the rate of change in MLS showed semiannual variation, while the sum of forcing terms showed annual variation (Figs. 2.7a and 2.7b). As a result, the rate of change in MLS and the sum of the forcing terms were poorly correlated both on the full time series ( $R = -0.02$ ; Fig. 2.7a) and on the seasonal average ( $R = -0.05$ ; Fig. 2.7b). In this box, the effect of entrainment was much smaller than the NE box (Figs. 2.5c, 2.5d, 2.7c, and 2.7d). The MLD and its temporal change in this box were smaller than the NE box (Figs. 2.6a and 2.6b), as previously demonstrated (Delcroix et al. 2005), which makes both  $w_e$  and  $h_m$  in the entrainment term [Eq. (2.1)] smaller. The small entrainment was primarily due to smaller  $\Delta S$  in this box, which will be discussed in Section 2.4. Thus, the forcing terms in this box were dominated by evaporation and precipitation (Figs. 2.7c and 2.7d). Since evaporation was always higher than precipitation, the sum of forcing terms was always positive and the MLS budget did not close.

In the SE box, the sum of the forcing terms was almost always larger than the rate

of change in MLS and had a large value in December (Figs. 2.8a and 2.8b), due to small MLD associated with subtropical BLs in the southern part of the box (Chapter 3). Without the December values, the correlation between the two terms was moderately positive both on the full time series ( $R = 0.40$ ; Fig. 2.8a) and on the seasonal average ( $R = 0.69$ ; Fig. 2.8b). The forcing terms are notably different from the NE box in two aspects. First, the Ekman term had a large contribution to decrease in MLS (Figs. 2.8c and 2.8d), unlike that in the NE box that was negligible (Figs. 2.5c and 2.5d). The large Ekman term is caused by a large northwestward gradient of MLS (Fig. 2.2a) and the strong northeasterly trade winds in this box; it transports salinity northward to the SSS maximum area, that is, the NPTW formation region. Secondly, the entrainment term worked to increase MLS, which was opposite to the NE box, due to high salinity water within BLs. In the SW box, the rate of change in MLS and the sum of the forcing terms did not correspond with each other (Figs. 2.9a and 2.9b), with a low correlation both on the full time series ( $R = 0.08$ ; Fig. 2.9a) and on the seasonal average ( $R = -0.06$ ; Fig. 2.9b), as in the NW box. The Ekman term was important for MLS variation (Figs. 2.9c and 2.9d) and the entrainment term was positive, as in the SE box.

### 2.3.3 Subduction of NPTW

Given the significantly different variations of MLS between the western and eastern sites of the NPTW formation region (Figs. 2.3a and 2.3b), it is natural to ask how NPTW formed in these sites is subducted and then transported westward by the North Equatorial Current to impact the downstream regions such as the one observed by Suga et al. (2000) at 137°E. A winter sea surface density map shows that isopycnals of 24.0 and 24.5 kg m<sup>-3</sup> traversed the center of the SSS maximum in the western and eastern sites of the NPTW formation region, respectively (Fig. 2.10). Consistently, at 150°W in the middle of the NE box, NPTW with  $\sigma_\theta \sim 24.5$  kg m<sup>-3</sup> was subducted (Figs. 2.11a and 2.11b). At 175°E crossing the center of the NW box, NPTW with  $\sigma_\theta \sim 24.0$  kg m<sup>-3</sup> was subducted; however, NPTW of 24.5 kg m<sup>-3</sup>, which is thought to be subducted from the NE box, no longer appeared as the salinity maximum at this longitude (Figs. 2.11c and 2.11d). NPTW subducted from east of Hawaii might be dissipated rapidly, as suggested in a numerical simulation (R. Furue, personal communication). Farther west at 155° and 135°E, NPTW did not outcrop to the surface and became gradually lighter to the downstream centered at  $\sigma_\theta = 23.5$ –24.0 kg

$\text{m}^{-3}$  (Figs. 2.11e-h). In addition, the isopycnal salinity map on  $\sigma_\theta = 24.0 \text{ kg m}^{-3}$  indicates that the high salinity tongue departed from the NW box and extended southwestward along the streamlines (Fig. 2.12). Thus, NPTW observed as the subsurface salinity maximum west (downstream) of the formation region originates mainly in the western site of the formation region.

This is confirmed by comparing interannual variations of maximum salinity of NPTW at each longitude (Fig. 2.13). The interannual variations at  $150^\circ\text{W}$  and  $175^\circ\text{E}$  correspond to that of MLS in the NE and NW boxes (Figs. 2.3a and 2.3b), respectively. Farther west, the interannual variation in the NW box propagated westward, decreasing salinity values due to dissipation. For example, a salinity minimum observed around the end of 2007 at  $175^\circ\text{E}$  was seen in early 2008 at  $165^\circ\text{E}$ , in late 2008 at  $155^\circ$  and  $145^\circ\text{E}$ , and in early 2009 at  $135^\circ\text{E}$ ; a salinity maximum observed mid-2006 at  $175^\circ\text{E}$  was seen in early 2007 at  $165^\circ\text{E}$ , in late 2007 at  $155^\circ\text{E}$ , in early 2008 at  $145^\circ\text{E}$ , and in mid-2008 at  $135^\circ\text{E}$ . This westward propagation was also seen in a salinity anomaly distribution on the  $\sigma_\theta = 24.0 \text{ kg m}^{-3}$  isopycnal (Fig. 2.14). A positive anomaly was generated around  $160^\circ\text{E}$  in 2003 and advected westward, reaching  $135^\circ\text{E}$  in mid-2005. A negative anomaly occurred around  $165^\circ\text{E}$  in early 2008 and arrived at  $135^\circ\text{E}$  in mid-2009. These propagations from the NW box to  $135^\circ\text{E}$  took about two years, being consistent with Fig. 2.13. This advection time is much shorter than that ( $\sim 5$  years) estimated from the World Ocean Atlas climatology (Bingham et al. 2002) and also than that ( $\sim 5$  years) observed on denser isopycnals of  $\sigma_\theta \sim 25.5 \text{ kg m}^{-3}$  (Sasaki et al 2010; Kolodziejczyk and Gaillard 2012). The westward advection speed estimated from the propagations in Figs. 2.13 and 2.14 is  $\sim 10 \text{ cm s}^{-1}$ , which is comparable to the westward current speed of the North Equatorial Current on the isopycnal surface of  $\sigma_\theta = 24.0 \text{ kg m}^{-3}$  estimated from MOAA\_GPV data, for example, one derived from the acceleration potential distribution in Fig. 2.12.

## 2.4 Discussion

MLS showed a clear seasonal cycle in the NE box (Figs. 2.3b and 2.4b) and not in the NW box (Figs. 2.3a and 2.4a). In order for the seasonal cycle to exist, there should be both periods with positive and negative forcing during the course of a year. In the NE box, the effect of entrainment became large due to the increase of MLD and made the sum of the forcing terms negative in fall to winter (Fig. 2.5). In the NW box, on

the other hand, the entrainment term did not become large even in fall–winter, and the sum of the forcing terms was always positive (Fig. 2.7). To clarify the reason of small entrainment term in the NW box, we compared the vertical profile of salinity in these boxes (Fig. 2.15). As these boxes are located in the NPTW formation region, salinity was maximum in the mixed layer and decreased with depth in the underlying layer in both boxes. Although the difference of salinity between these two boxes was small within the mixed layer, salinity in the underlying layer was lower in the NE box. On isobaric levels, water in the NE box was denser than that in the NW box (Fig. 2.15b). Comparing salinity distributions on isopycnal surfaces of  $\sigma_\theta = 25.2$  and  $25.4 \text{ kg m}^{-3}$ , which correspond to the isobaric level of  $\sim 200$  dbar in the NW box and the NE box, respectively, fresher water was advected from farther north outcrop line on the isopycnal surface of  $\sigma_\theta = 25.4 \text{ kg m}^{-3}$  (Fig. 2.16), leading a larger vertical gradient of salinity and hence larger  $\Delta S$  [the salinity difference between the mixed layer base and 20 dbar below; Eq. (2.1)] in the NE box than in the NW box (Fig. 2.17). Such subduction and advection of fresher water must be important for the seasonal variation of NPTW in the eastern part of the formation region.

A similar zonal tendency in SSS variations has been obtained for the equatorial Pacific (Delcroix and Hénin 1991). That is, interannual variation was dominant in the western equatorial Pacific due to the El Niño–Southern Oscillation (ENSO) related precipitation, while seasonal variation was prominent in the eastern equatorial Pacific. The seasonal cycle of SSS in the eastern equatorial region might be related to the entrainment of the South Pacific Tropical Water (Johnson and McPhaden 1999; Kessler 1999) and/or South Pacific Eastern Subtropical Mode Water (Wong and Johnson 2003; Sato and Suga 2009), which are subducted from the eastern South Pacific subtropical gyre and then advected to the equatorial region, in a similar manner that the subduction and entrainment of freshwater are important for the seasonal variation of the NPTW in the eastern part of its formation region.

In the SE box, the entrainment term increased the MLS (Fig. 2.8). Assuming that the underlying high salinity water is the subducted NPTW (Sato et al. 2004; 2006), a part of this NPTW subducted from the NE box is entrained into the mixed layer in the SE box, and is then advected back to the NE box by the Ekman flow, under the positive E–P flux that continuously increases the MLS (Fig. 2.2b). Since the effect of northward Ekman advection is large in the SE box and small in the NE box (Figs. 2.5

and 2.8), salinity convergence occurs between two boxes, leading to the formation of the salinity maximum (i.e., NPTW) to the north of the E-P maximum (Figs. 2.2a and 2.2b). Such a meridional overturning circulation of NPTW in the eastern regions is schematically illustrated in Fig. 2.18. In this circulation, the positive E-P flux that increases the NPTW salinity in the mixed layer is balanced by dissipation and, more importantly, the freshwater flux from the lower, fresher layer in the formation region.

In the NW box, the salinity budget was not closed (Sec. 2.3.2). This may be due to the dissipation term, which is neglected in the MLS budget equation [Eq. (2.1)], and an error of forcing terms in this box. Past observations based on the dispersion of surface drifters demonstrated that lateral diffusivity is about twice larger in the NW box than in the NE box (Zhurbas and Oh 2004). If it is assumed that the lateral diffusivity is  $1 \times 10^4 \text{ m}^2 \text{ s}^{-1}$  based on Zhurbas and Oh's map and use the average  $\nabla^2 S$  of  $5 \times 10^{-12} \text{ m}^{-2}$  in the NW box (Fig. 2.2a), the decrease of MLS by diffusion is estimated to be  $\sim 0.1 \text{ month}^{-1}$ . This matches in magnitude with the discrepancy between the rate of change in MLS and the sum of the forcing terms (Figs. 2.7a and 2.7b). Furthermore, Qiu and Chen (2013) analyzed satellite altimeter data during 1992–2012 and detected that eddy kinetic energy (EKE) in the subtropical North Pacific exhibits a larger variation in the NW box than in the NE box and was stronger in 2004 and 2007, when MLS in the NW box was relatively low (Fig. 2.3a). Hence, I estimated the residual  $A$  of Eq. (2.1) as

$$\frac{\partial S}{\partial t} = \frac{(E - P)S}{h_m} - \mathbf{u}_e \cdot \nabla S - \mathbf{u}_g \cdot \nabla S - \frac{w_e \Delta S}{h_m} - A, \quad (2.5)$$

and EKE, following Qiu and Chen (2013), as

$$EKE = \frac{1}{2} \left[ \left( \frac{g}{f} \frac{\partial h'}{\partial x} \right)^2 + \left( \frac{g}{f} \frac{\partial h'}{\partial y} \right)^2 \right], \quad (2.6)$$

where  $x$  and  $y$  are the zonal and meridional coordinates,  $h'$  is sea surface height anomaly, and  $g$  is the gravity constant. The obtained EKE in the NW box was one and half to two times larger than that in the NE box (not shown) and showed similar interannual variation to  $A$  ( $R = 0.71$ ; Fig. 2.19a). Furthermore, under the assumption

that the variation of the lateral diffusivity in this box is related to that of EKE,  $-EKE \cdot \nabla^2 S$  was calculated and compared to  $A$ . They also showed similar interannual variation and are highly correlated with each other ( $R = 0.70$ ; Fig. 2.19a). Thus, eddy diffusion may play an important role in the interannual variation of MLS in the NW box. It should be mentioned that this result was not sensitive to the choice of freshwater flux data (see Appendix). On a seasonal time scale,  $-EKE \cdot \nabla^2 S$  had two peaks in May and October and they corresponded well to those of  $A$  in June and October, respectively (Fig. 2.19b), suggesting that eddy diffusion may also have a significant contribution on a seasonal time scale and that semiannual variation of MLS in the NW box (Fig. 2.4a) may be due to the decrease of MLS around June by enhanced eddy diffusion.

According to Qiu and Chen (2013), there is a positive correlation between EKE in the western subtropical North Pacific and the Pacific Decadal Oscillation (PDO; Mantua et al. 1997) index at least after 1992, and the latter led the former by one year. This suggests that the interannual variation of MLS in the NW box may also be related to the PDO. To examine the relation for a sufficiently long period, I compared the variation of the salinity maximum value along the 137°E repeat hydrographic section of the Japan Meteorological Agency (Masuzawa 1967; Qiu and Joyce 1992; Suga et al. 2000) and that of the PDO index from [http://www.data.kishou.go.jp/shindan/b\\_1/pdo/winpdo.txt](http://www.data.kishou.go.jp/shindan/b_1/pdo/winpdo.txt). The salinity maximum value at 137°E dropped several years after a period of positive PDO index, showing the strongest negative correlation with a time lag of three years ( $R = -0.43$ ; Fig. 2.20). This time lag agrees with the sum of a one-year lag between the PDO index and the EKE (Qiu and Chen 2013) and a two-year period needed for the MLS variation in the NW box to propagate to 137°E (Fig. 2.13). Thus, the interannual variation of MLS in the NW box is likely to be controlled by the PDO-related eddy diffusion.

## 2.5 Summary

Formation and subduction of NPTW and their interannual variation have been investigated by using the MOAA\_GPV gridded Argo data and the various surface flux data in 2003–11. The MLS variations were significantly different between the western and eastern sites of the NPTW formation region. Interannual variation was dominant in the western site, while seasonal one was dominant in the eastern site.

The MLS variation in the eastern site was controlled mainly by evaporation, precipitation and entrainment, and was closely related to the MLD variation. Specifically, MLS increased from March to September–October due to the excess evaporation when the mixed layer shoaled and stayed shallow, while it decreased due to the entrainment of fresher water in the rest of year when the mixed layer deepened. The existence of fresher water below the mixed layer, which is subducted from the north of the formation region, is important for the clear seasonal variation in the eastern site.

In the western site of the formation region where the effect of entrainment was small due to the small vertical difference in salinity across the mixed layer base, the forcing terms were governed by evaporation minus precipitation that was always positive throughout the year, and the salinity budget equation [Eq. (2.1)] is not closed. This imbalance may be explained by the fact that the effect of dissipation in the budget equation is neglected. The residual term of the equation, defined as the difference between the rate of change in MLS and the sum of the forcing terms [Eq. (2.5)], was highly correlated with EKE in the western North Pacific which, in turn, was correlated with the PDO index. Thus, the MLS variation in the western site is likely to be controlled by evaporation, precipitation, and PDO-related eddy diffusion, at least after 1992.

From the western and eastern sites of the formation region, NPTW with  $\sigma_\theta = 24.0$  and  $24.5 \text{ kg m}^{-3}$  was subducted, respectively. Subsequently the NPTW formed at the eastern site was dissipated quickly, while that formed at the western site was advected westward, transmitting PDO-related salinity anomalies from the formation region to the Philippines Sea. It is an important future task to examine whether these anomalies survive the intensive mixing in the Philippines Sea and how they are further advected and affect upper ocean processes in the tropical Pacific and the Kuroshio Extension regions.

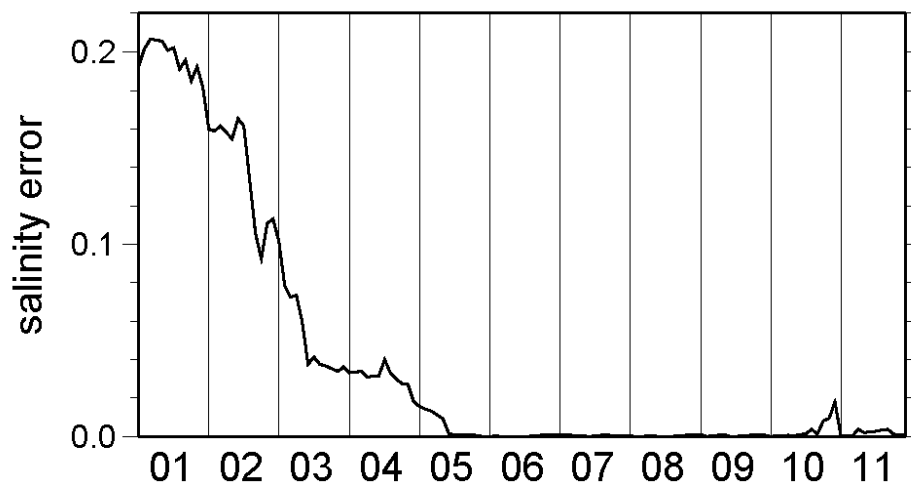


Fig. 2.1. Time series of the interpolation error in 10-dbar salinity of MOAA\_GPV, averaged in the subtropical North Pacific at 15°–30°N, 165°E–125°W. ©American Meteorological Society. Used with permission.

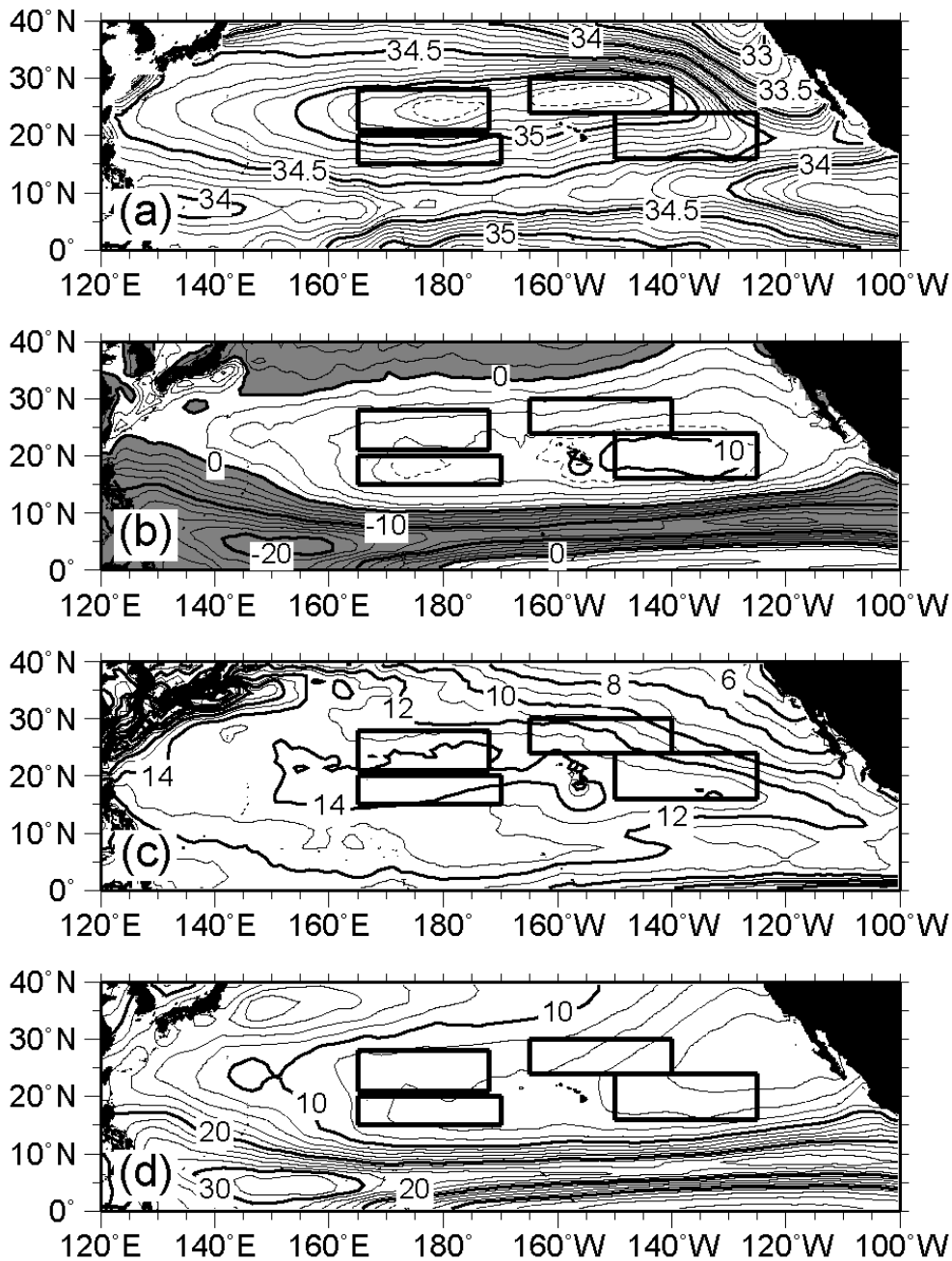


Fig. 2.2. Distributions of (a) salinity at 10-dbar depth and (b) evaporation minus precipitation ( $\text{cm month}^{-1}$ ), (c) evaporation ( $\text{cm month}^{-1}$ ), and (d) precipitation ( $\text{cm month}^{-1}$ ) at the sea surface in the North Pacific, averaged in 2003–11. Dashed contours in (a) and (b) indicate the salinity value of 35.35 and the evaporation minus precipitation value of  $9 \text{ cm month}^{-1}$ , respectively. Gray shading in (b) denotes negative values. Four thick rectangles indicate the NW, NE, SW, and SE boxes. ©American Meteorological Society. Used with permission.

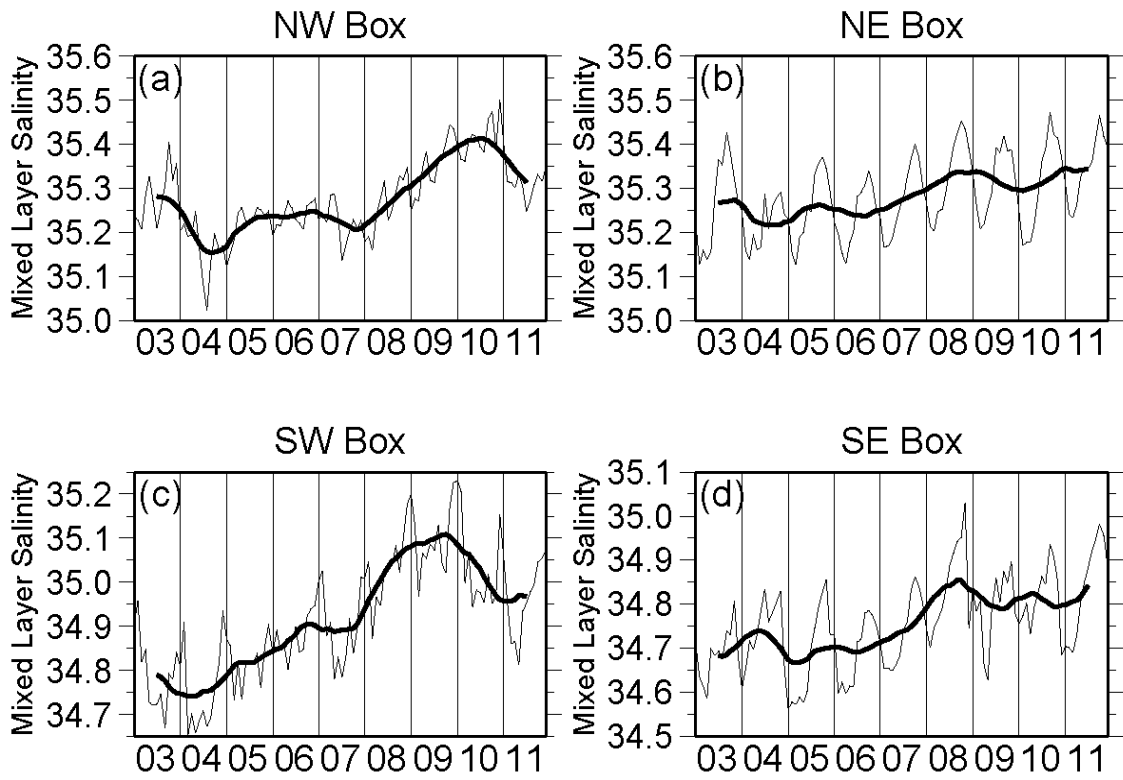


Fig. 2.3. Time series of MLS in the (a) NW, (b) NE, (c) SW, and (d) SE boxes in 2003–11 (thin curve). Thick curve indicates the 12-month moving average.  
 ©American Meteorological Society. Used with permission.

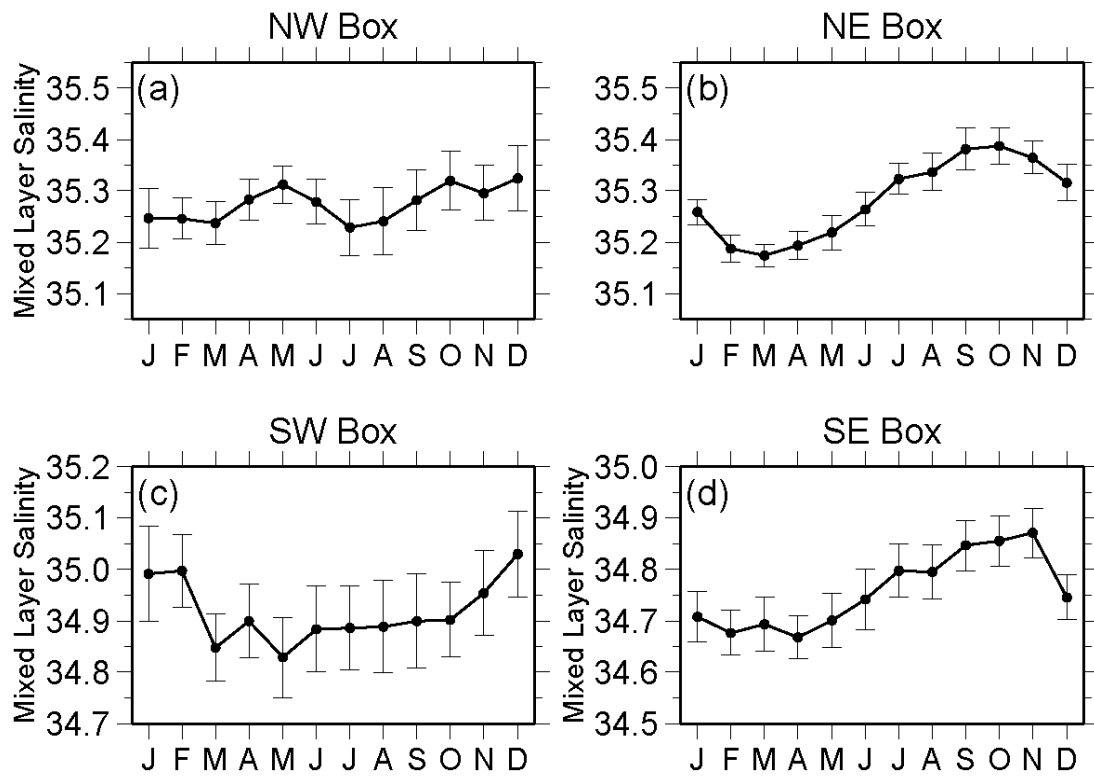


Fig. 2.4. Monthly average of MLS in 2003–11 in the (a) NW, (b) NE, (c) SW, and (d) SE boxes. Vertical bars indicate the 95% confidence interval. ©American Meteorological Society. Used with permission.

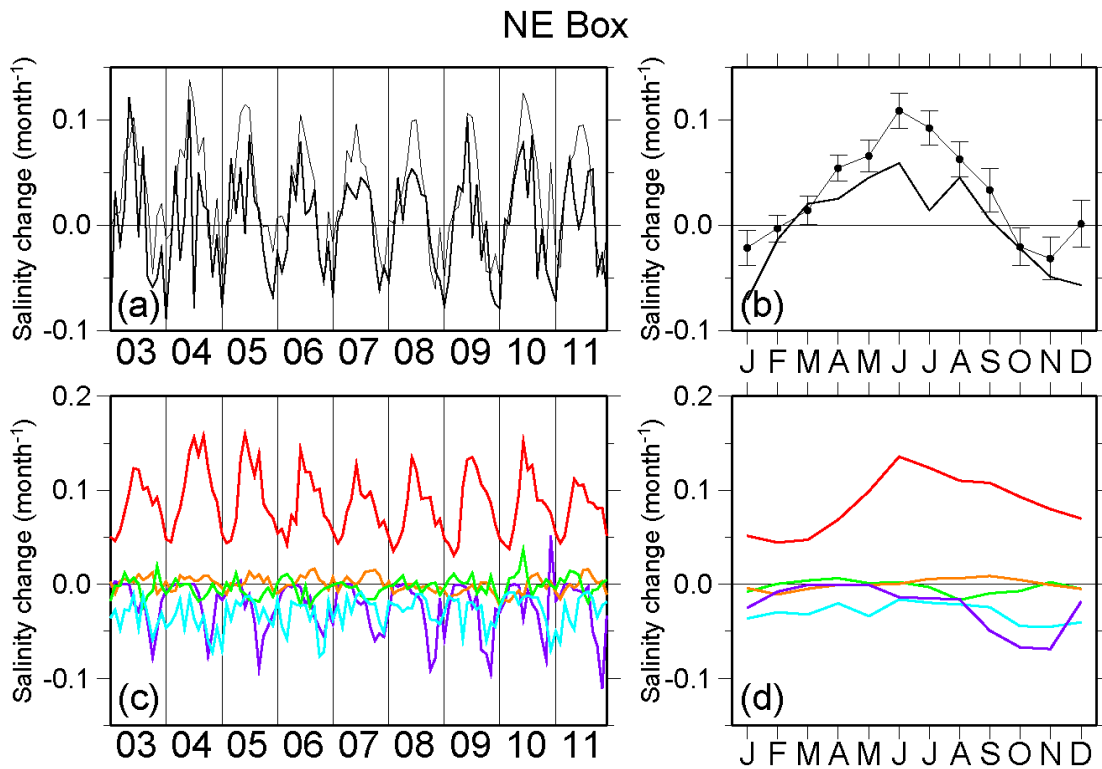


Fig. 2.5. (a) Time series during 2003–11 of rate of change in MLS [left hand side of Eq. (2.1); thick curve] and the sum of forcing terms [right hand side of Eq. (2.1); thin curve] and (b) their monthly average in the NE box. (c) Time series during 2003–11 of each forcing term and (d) their monthly average in the NE box: evaporation term (red curve), precipitation term (blue curve), Ekman advection term (green curve), geostrophic advection term (orange curve), and entrainment term (purple curve). Vertical bars in (b) indicate the statistical error estimated from the 95% confidence interval of the forcing terms. ©American Meteorological Society. Used with permission.

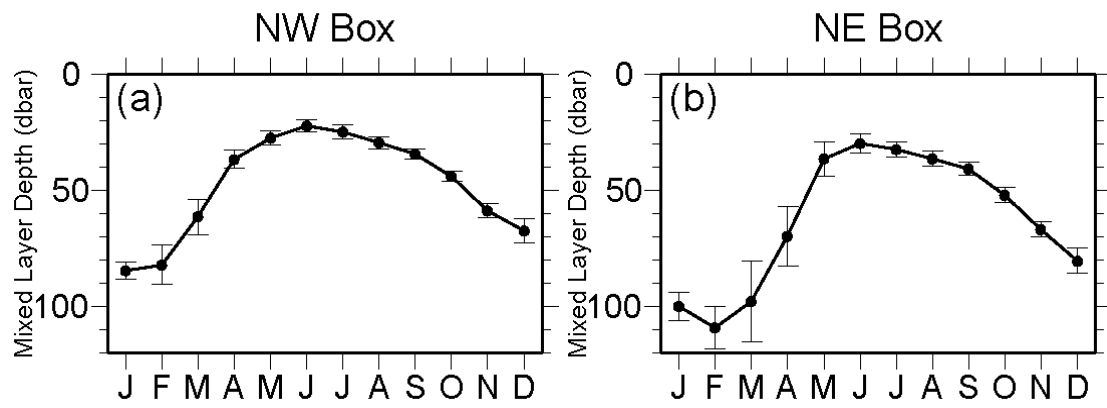


Fig. 2.6. Monthly average of MLD in 2003–11 in the (a) NW and (b) NE boxes. Vertical bars indicate the 95% confidence interval. ©American Meteorological Society. Used with permission.

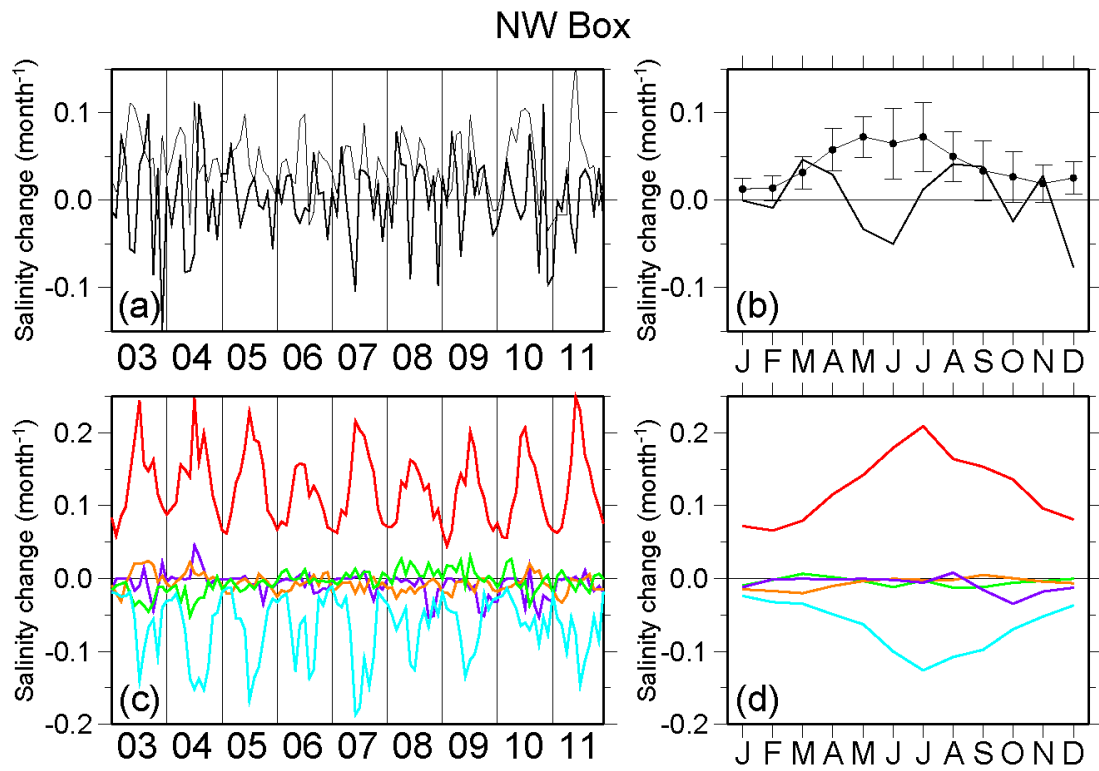


Fig. 2.7. The same as Fig. 2.5 but for the NW box. ©American Meteorological Society. Used with permission.

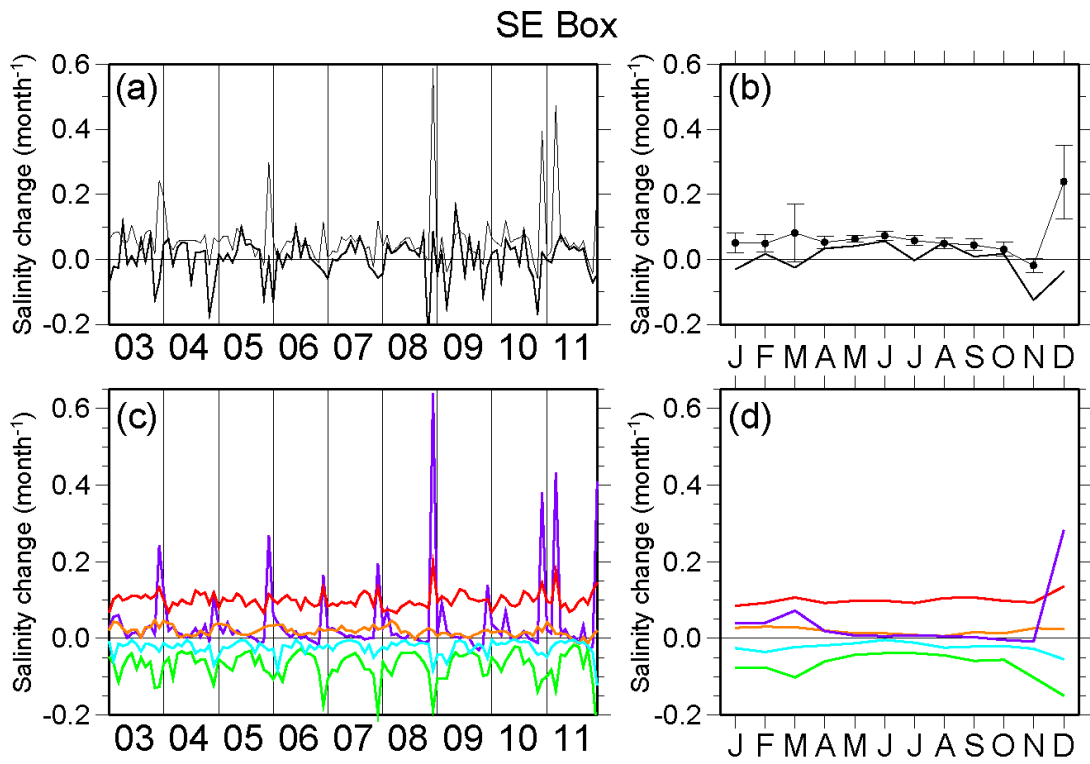


Fig. 2.8. The same as Fig. 2.5 but for the SE box. ©American Meteorological Society. Used with permission.

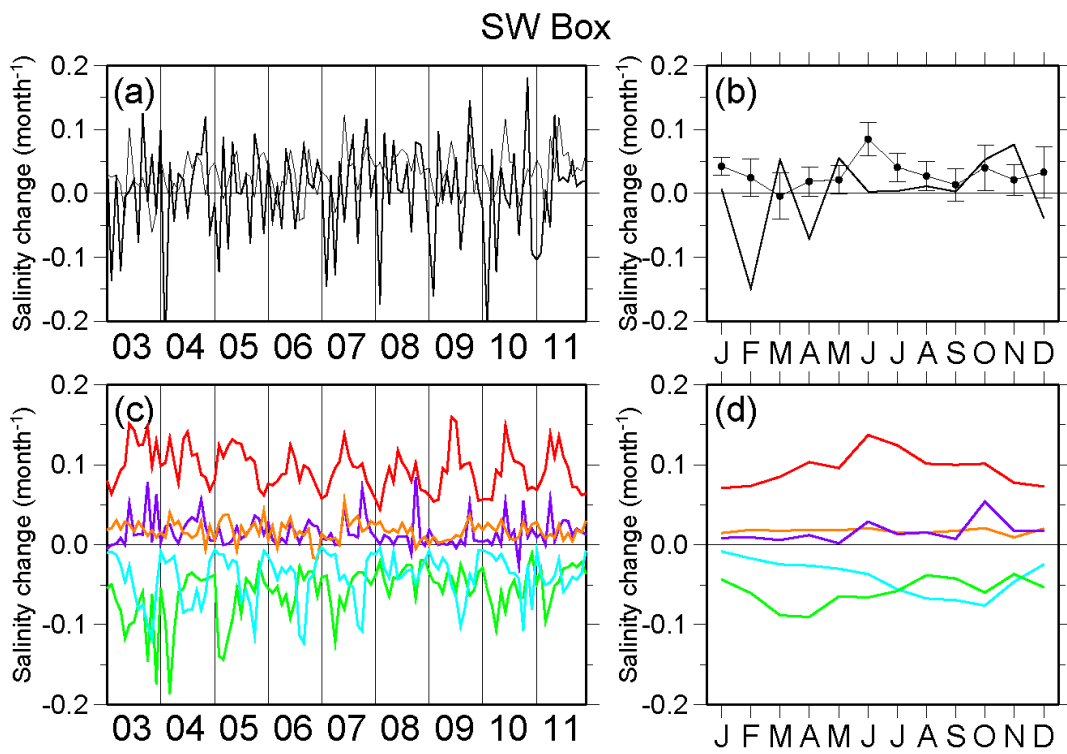


Fig. 2.9. The same as Fig. 2.5 but for the SW box. ©American Meteorological Society. Used with permission.

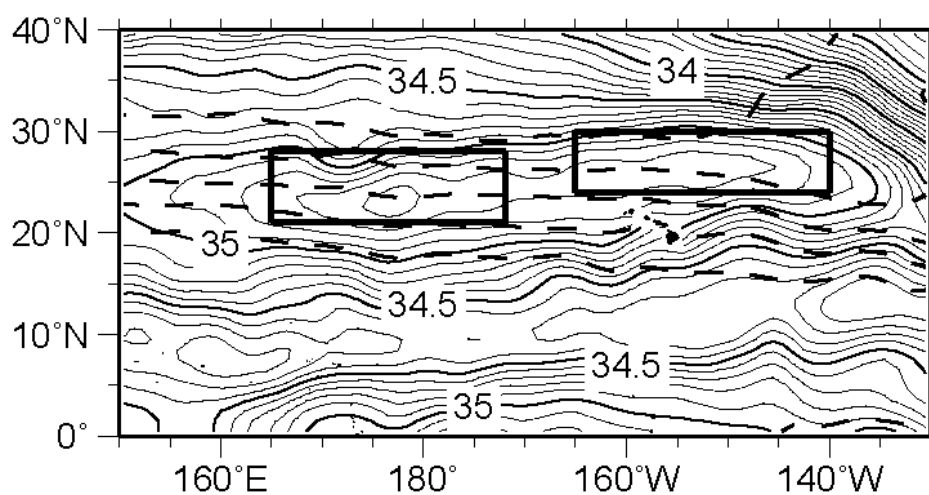


Fig. 2.10. Distribution of 10-dbar salinity (solid contours), averaged in January–March of 2003–11. Dashed contours denote potential density of 23.0, 23.5, 24.0, 24.5, and 25.0  $\text{kg m}^{-3}$  at 10-dbar depth from the south. Two thick rectangles indicate the NW and NE boxes. ©American Meteorological Society. Used with permission.

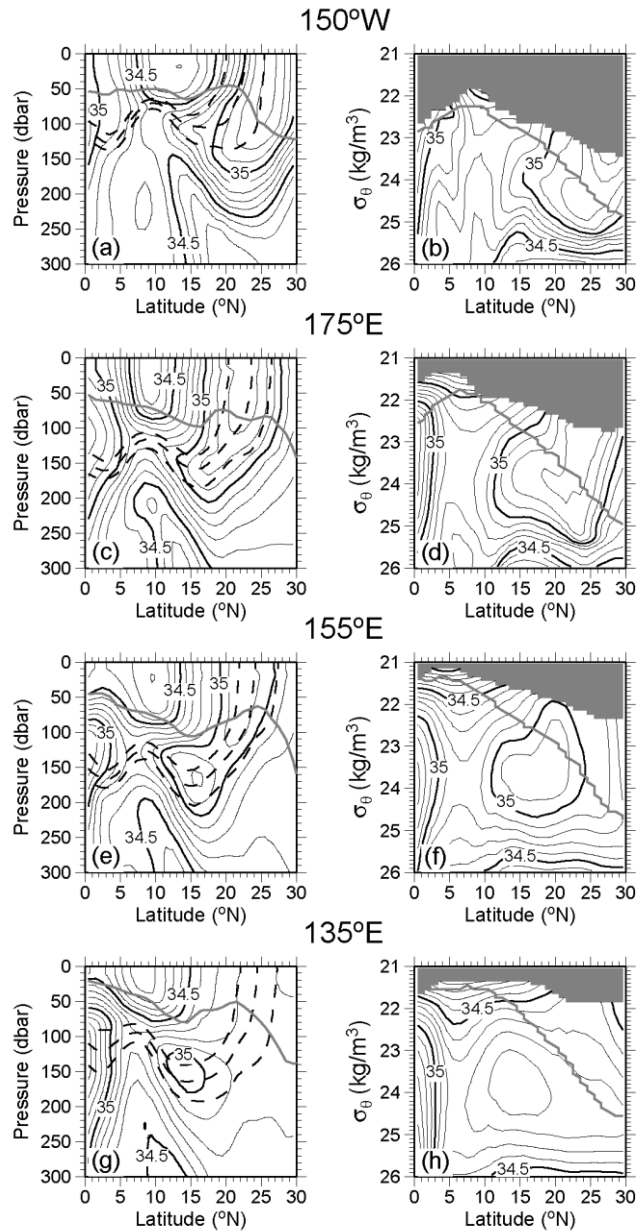


Fig. 2.11. (a, c, e and g) Meridional section of salinity with respect to pressure, averaged in February of 2003–11 along (a) 150°W, (c) 175°E, (e) 155°E, and (g) 135°E (black solid line). Dashed lines indicate isopycnals of  $\sigma_\theta = 23.5, 24.0$  and  $24.5 \text{ kg m}^{-3}$ . Gray solid line denotes the mixed layer base. (b, d, f and h) Meridional section of salinity with respect to  $\sigma_\theta$ , averaged in August of 2003–11 along (b) 150°W, (d) 175°E, (f) 155°E, and (h) 135°E (black line). Gray line indicates the outcrop surface in February. ©American Meteorological Society. Used with permission.

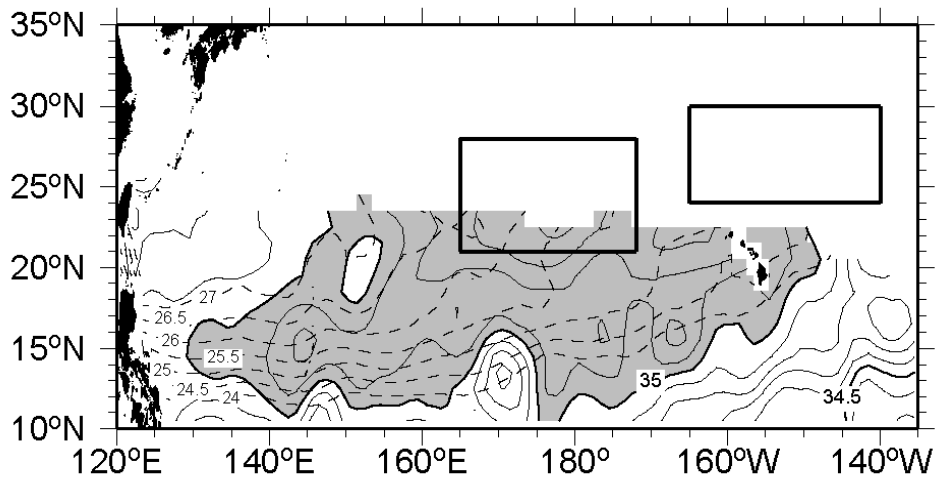


Fig. 2.12. Distribution of salinity (solid contours) and acceleration potential ( $\text{m}^2/\text{s}^2$ ; dashed contours) on the  $\sigma_\theta = 24.0 \text{ kg m}^{-3}$  isopycnal, averaged in March of 2003–11. Gray shading indicates salinity higher than 35. Two thick rectangles indicate the NW and NE boxes. ©American Meteorological Society. Used with permission.

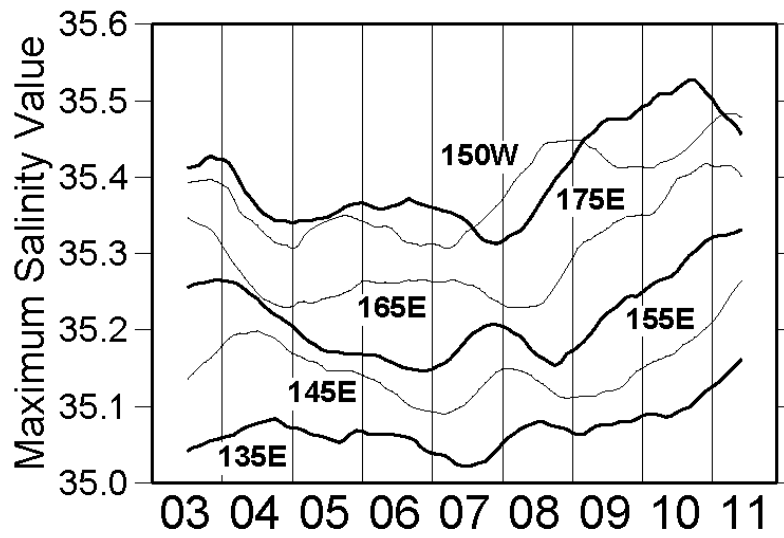


Fig. 2.13. Time series during 2003–11 of the 12-month moving average of the maximum salinity value at each longitude lying north of 7°N and below the mixed layer base. ©American Meteorological Society. Used with permission.

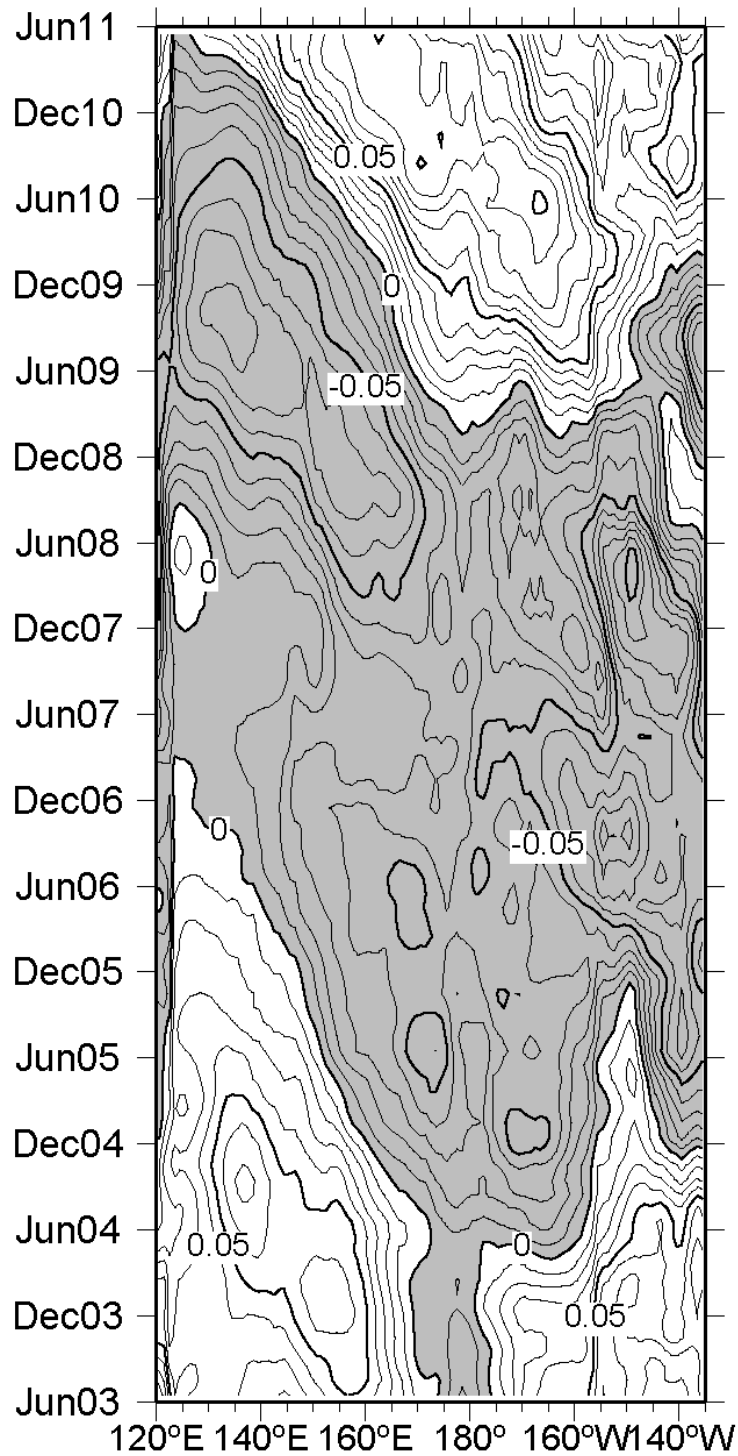


Fig. 2.14. Longitude-time plot of 12-month moving average of salinity anomaly on the  $\sigma_{\theta} = 24.0 \text{ kg m}^{-3}$  isopycnal. The anomaly is relative to the 2003–11 average at each longitude and is averaged between  $15^{\circ}$  and  $20^{\circ}\text{N}$ . Gray shading denotes negative values. ©American Meteorological Society. Used with permission.

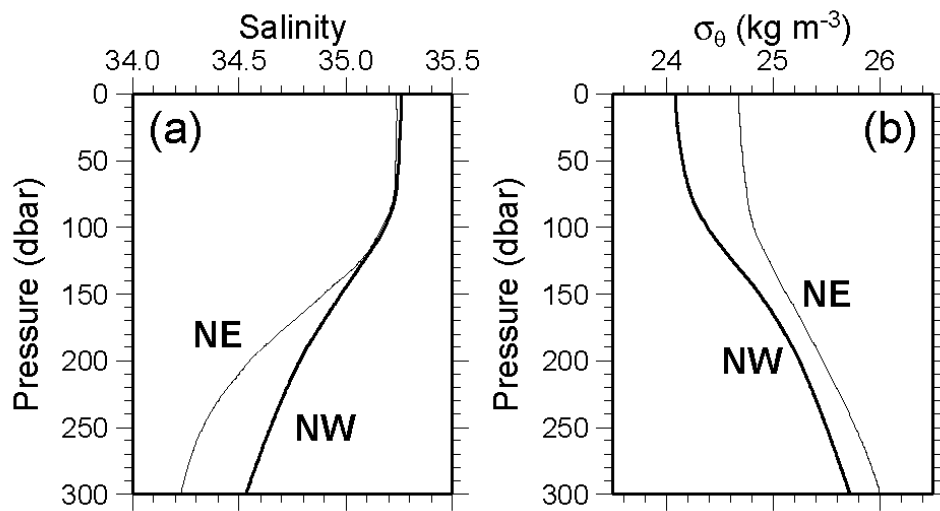


Fig. 2.15. Vertical profile of salinity (a) and  $\sigma_\theta$  (b) averaged in the NW and NE boxes for January–March of 2003–11. ©American Meteorological Society. Used with permission.

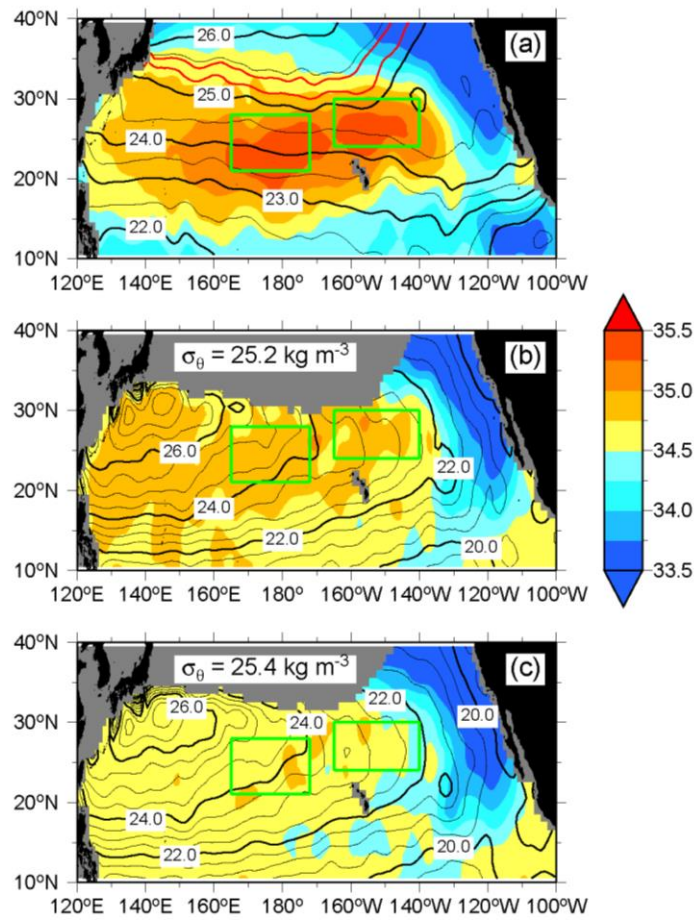


Fig. 2.16. (a) Distribution of 10-dbar salinity (color) and  $\sigma_\theta$  (black contour), averaged in February of 2003–11. Red lines denote the outcrop line of isopycnal surface of  $\sigma_\theta = 25.2$  and  $25.4 \text{ kg m}^{-3}$ . (b and c) Distribution of salinity (color) and acceleration potential ( $\text{m}^2/\text{s}^2$ ; contour) on the  $\sigma_\theta = 25.2$  (b) and  $25.4$  (c)  $\text{kg m}^{-3}$  isopycnal, averaged in February of 2003–11. Two green rectangles indicate the NW and NE boxes.

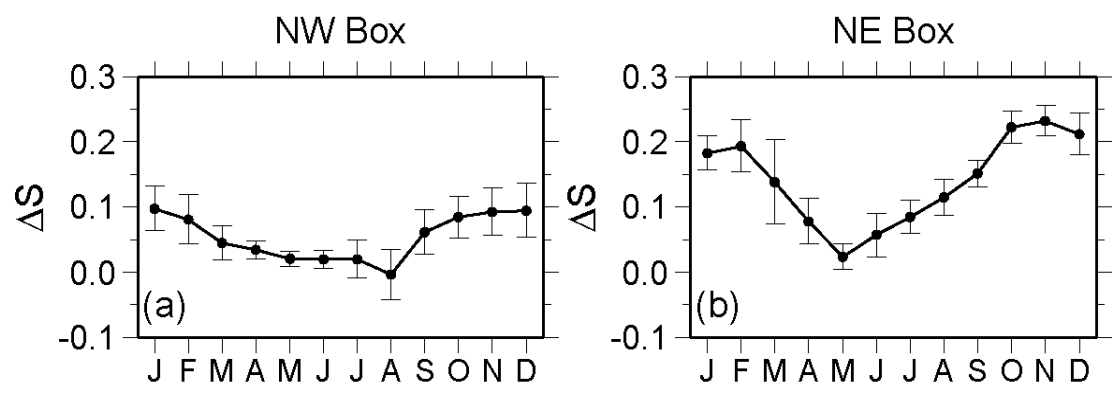


Fig. 2.17. Monthly average of  $\Delta S$  in 2003–11 in the (a) NW and (b) NE boxes. Vertical bars indicate the 95% confidence interval. ©American Meteorological Society. Used with permission.

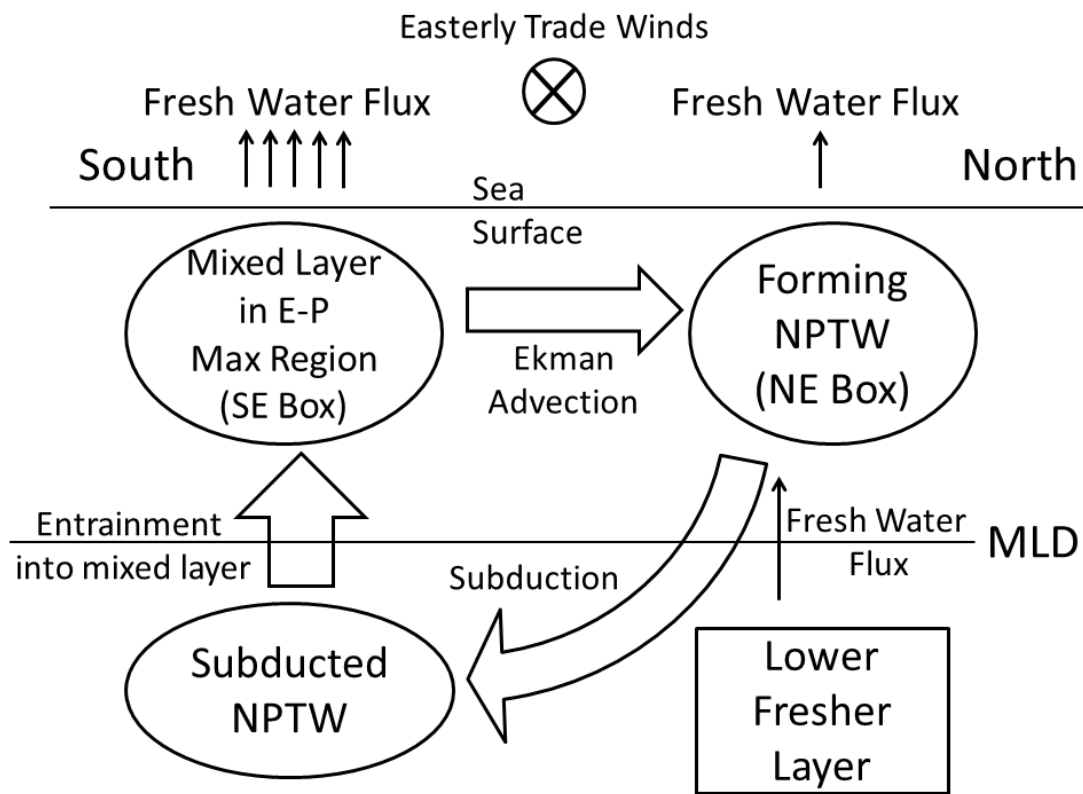


Fig. 2.18. Schematic diagram of the meridional overturning circulation of NPTW in the NE and SE boxes. ©American Meteorological Society. Used with permission.

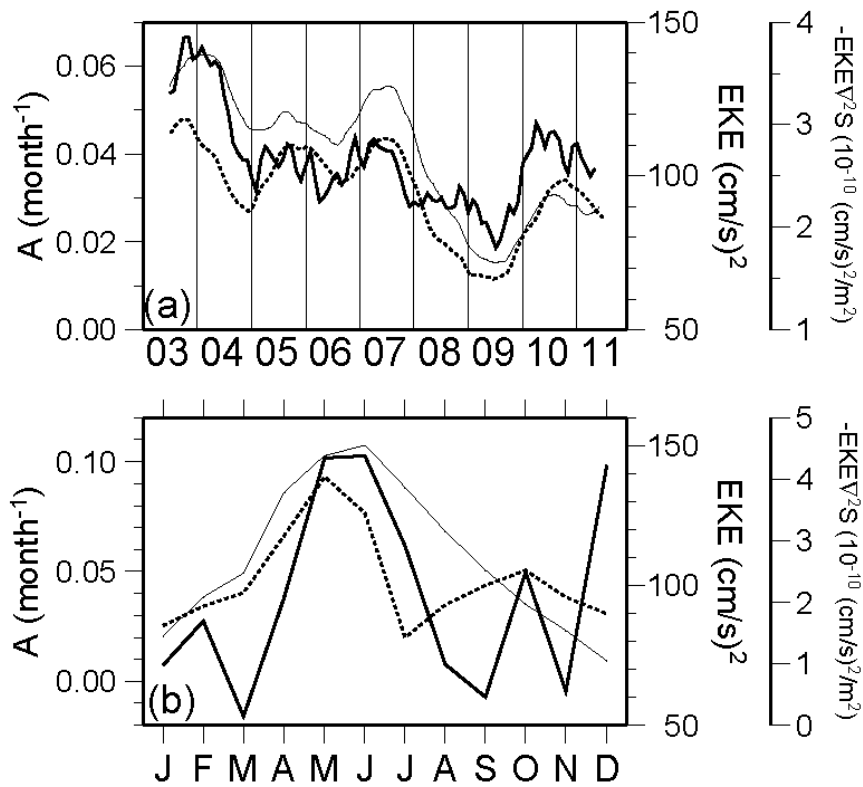


Fig. 2.19. Time series of (a) 12-month moving average and (b) monthly average in 2003–11 of the residual ( $A$ ; thick curve),  $EKE$  (thin curve), and  $-EKE \cdot \nabla^2 S$  (dotted line) in the NW box. ©American Meteorological Society. Used with permission.

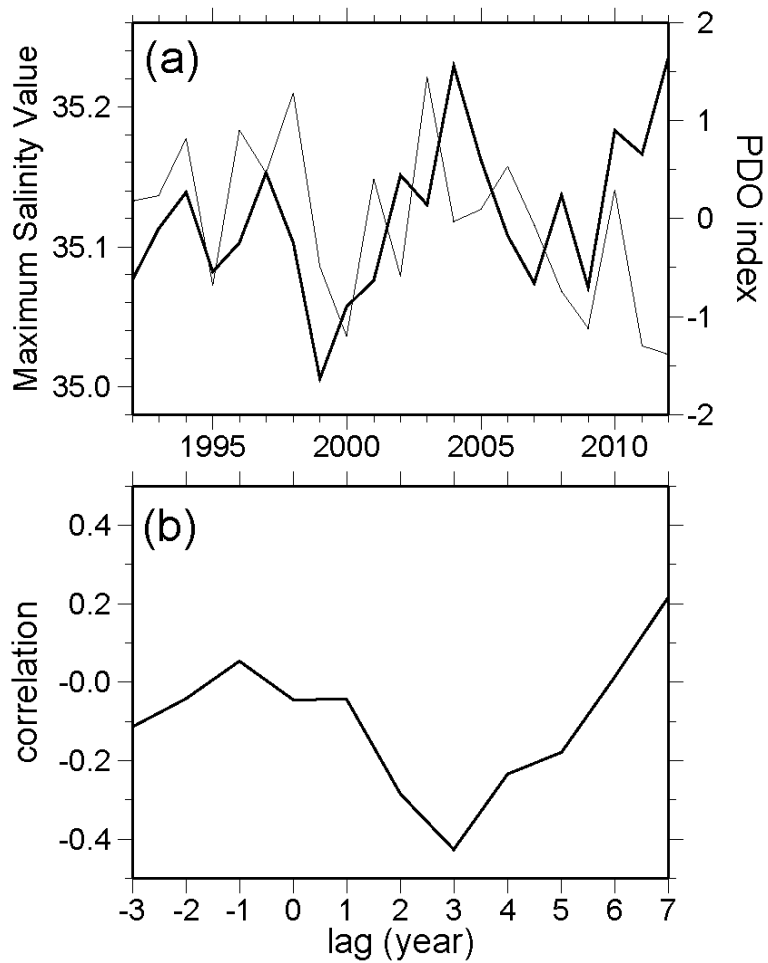


Fig. 2.20. (a) Time series of the winter maximum salinity value north of 7°N and below the mixed layer base in the 137°E repeat hydrographic section (thick curve) and the PDO index (thin curve). (b) Lag correlation between the salinity maximum value at 137°E and the PDO index. A positive lag indicates that the PDO index leads. ©American Meteorological Society. Used with permission.

## **Chapter 3**

# **Seasonal and Interannual Variability of Barrier Layers in the Subtropical Pacific and Their Formation Mechanism**

### **3.1 Introduction**

Barrier layer (BL) is defined as the layer between bases of the mixed layer and the isothermal layer, when the former is shallower than the latter due to salinity stratification (Lukas and Lindstrom 1991). BL is believed to work as a barrier against the heat and kinetic energy input into the ocean interior. When BLs are formed, kinetic energy transported from the atmosphere to the ocean by wind is trapped into the shallowed mixed layer, and accelerates flow only in the mixed layer (Vialard and Delecluse 1998a). In addition, the cooling effect of entrainment is reduced because the underlying BL water that is entrained into the mixed layer has the same temperature as the mixed layer. For these reasons, BL is thought to play an important role in air-sea interactions such as the El Niño-Southern Oscillation (ENSO; Vialard and Delecluse 1998b; Maes and Belamari 2011), the Indian Ocean Dipole (Masson et al. 2004), and tropical cyclones (Balaguru et al. 2012).

The mismatch between the isothermal layer depth (ILD) and the mixed layer depth (MLD), i.e., the presence of BLs, was first reported in the western equatorial Pacific by using shipboard observation data (Godfrey and Lindstrom 1989; Lukas and Lindstrom 1991). Since then, the interannual variation of BLs and its link to the ENSO have been investigated (Ando and McPhaden 1997; Delcroix and McPhaden 2002; Bosc et al. 2009; Qu et al. 2014). The formation of BLs in the western equatorial Pacific has been attributed to freshening near the sea surface by heavy precipitation (Lukas and

Lindstrom 1991; Sprintall and Tomczak 1992) and to the tilting process of the meridional sea surface salinity (SSS) front lying in the eastern edge of the warm pool (Cronin and McPhaden 2002). In the latter process, eastward advection of fresher surface water caused by westerly wind burst plays an important role and is responsible for a dominant time scale of 12–25 days for BLs (Sprintall and McPhaden 1994).

After the discovery of BL in the western equatorial Pacific, it was reported that BLs are also distributed in the northwest equatorial Atlantic based on climatology (Sprintall and Tomczak 1992), and their seasonal variation and impact on sea surface temperature (SST) have been investigated (Foltz and McPhaden 2005; 2008; 2009). Since this region is characterized as net freshwater loss, formation of BLs there cannot be explained by surface freshening caused by precipitation not as in the western equatorial Pacific. Sprintall and Tomczak (1992) hypothesized that subducted high salinity waters from the subtropical regions, that is, Tropical Waters (TWs) are advected from both hemispheres and that they form BLs there through salinification in the subsurface.

BLs are formed not only in the tropical region but also in the subtropical regions (Sprintall and Tomczak 1992). Analyses of Argo profiling float data revealed the existence of BLs in winter in the subtropical region of the North Pacific (Sato et al. 2004) and each ocean basin (Sato et al. 2006) in association with SSS fronts lying on the equatorward side of SSS maxima. These BLs observed by Argo floats (Sato et al. 2004; 2006) and historical (Mignot et al. 2009) temperature and salinity profiles were thick and showed patchy distribution, implying that the spatial scale of BLs is small. They can influence formation of spiciness anomalies and local air-sea interaction by modulating SST in the subtropics.

The formation mechanism of BLs in the subtropical region has been under discussion. Since evaporation exceeds precipitation as in the equatorial Atlantic, precipitation is not responsible for BL formation in the subtropics. Sato et al. (2004) suggested similar formation mechanism as in the tropical Atlantic, that is, winter subduction of North Pacific Tropical Water (NPTW) across SSS front contributes to BL formation in the subtropical North Pacific based on observation by a single Argo float. They also suggested that small spatial scale of BLs reflects that of sharp SSS front. This mechanism is thought to be applicable to subtropical BL formation in global ocean (Sato et al. 2006). On the other hand, Mignot et al. (2007) proposed a different

mechanism of subtropical BL formation and seasonality. They argued that since vertical salinity gradient has dominant contribution to density stratification at the base of mixed layer owing to poleward Ekman advection of fresher water, isothermal layer deepens faster than salinity-stratified mixed layer during cooling period and hence BL grows from autumn to winter. From spring to summer, grown BL becomes thin and disappear in accordance with shoaling mixed and isothermal layers. This growth scenario of subtropical BL is also suggested by general ocean circulation models (Mignot et al. 2012; Veneziani et al. 2014). It is important to clarify the formation mechanism of subtropical BLs for better understanding of not only the BL formation in the other regions, especially in the northwest equatorial Atlantic where the importance of TW subduction was suggested, but also the impact of TW to the downstream regions. However, it had been impossible to verify these suggested mechanisms due to the deficiency of salinity data.

Recent accumulation of Argo profiling float data exceeding 10 years and construction of various surface flux data enabled us to study surface salinity processes such as SSS variation and its mechanism (e.g. Ren and Riser 2009; Bingham et al. 2012), the formation and subduction of NPTW (Chapter 2) and South Pacific Tropical Water (SPTW; Zhang and Qu 2014), and BL variation in the tropical region (Qu et al. 2014). Based on these results, it is worth revisiting the property and seasonality of BLs in the subtropical Pacific and validating their formation mechanism in the subtropical Pacific suggested by previous studies using Argo and other hydrographic data. The aim of this chapter is to investigate the seasonal and interannual variations of BLs and to clarify the mechanism of BL formation in the subtropical North and South Pacific. The data and definition of BL are explained in Sec. 3.2. Seasonality and distribution of BLs in the subtropical Pacific are examined in Sec. 3.3. Formation mechanisms of BLs are investigated in Sec. 3.4. Interannual variation of winter BLs and its relation to climate variations are investigated in Sec. 3.5. Discussion and summary are given in Sec. 3.6 and Sec. 3.7, respectively.

## **3.2 Data and Method**

Temperature and salinity data from Argo profiling floats in the North and South Pacific in 2003–12, which were downloaded from the ftp site of the Argo Global Data Assembly Center (<ftp://usgodae.org/pub/outgoing/argo>; <ftp://ftp.ifremer.fr/ifremer/argo>)

were used. Most of the North Pacific float data, which had been downloaded monthly right after the observation, have passed through only the real-time quality control, while about 80% of the South Pacific data, which were recently downloaded, have also passed through the delay-mode quality control (Wong et al. 2014). These data were edited as outlined by Oka et al. (2007), and selected 13,978 and 9,651 profiles in the SSS front region in the Northern and Southern Boxes (defined in Sec. 3.3), respectively. Typical vertical resolution of these profiles was 2–5 dbar in the upper 200 dbar and was high enough to resolve BLs thicker than 10 dbar. Finally, each profile was vertically interpolated at an interval of 1 dbar using the Akima spline (Akima 1970).

The monthly mean temperature and salinity gridded data based mainly on Argo profiling float observations, named MOAA\_GPV (Hosoda et al. 2008), in 2003–12 were also used. This dataset was prepared by optimally interpolating the anomalies of Argo-based temperature and salinity data from those of the World Ocean Atlas 2001 climatology (Conkright et al. 2002) onto  $1^\circ \times 1^\circ$  grid points at each standard depth. In this study, the temperature and salinity data between 10 and 2000 dbar at each grid point were vertically interpolated at an interval of 1 dbar using the Akima spline.

Reanalysis data of precipitation from the Global Precipitation Climatology Project (Huffman et al. 1997; Adler et al. 2003), and wind stress from the National Centers of Environmental Prediction (Kistler et al. 2001) were also used. These data for each month from 2003 through 2012 were linearly interpolated onto the same grid points as MOAA\_GPV.

The output data of an eddy-resolving ocean general circulation model (OGCM), the CCSR Ocean Component Model (COCO; Hasumi 2006), was also analyzed. The model covers the global ocean with a horizontal resolution of  $0.1^\circ \times 0.1^\circ \cos\theta$  on the spherical coordinate, where  $\theta$  is the latitude. There are 23 vertical levels from sea surface to 198 m, increasing the interval from 2 m to 18 m. Thus, BLs thicker than 20 dbar can be potentially resolved in this model. The initial potential temperature and salinity are based on the Polar science center Hydrographic Climatology (PHC; Steele et al. 2001). The Coordinated Ocean-ice Reference Experiments interannual forcing version 2 from 1950 to 2006 is used to drive the model (Large and Yeager 2009). The potential temperature and salinity are restored to the monthly climatology of PHC on a timescale of 10 days during the first five years of the integration. In this chapter, five-day mean potential temperature, salinity, and zonal and meridional velocities in

2006 were analyzed. The values at each grid point were vertically interpolated at an interval of 1 dbar using the Akima spline.

In this study, ILD is defined as the depth at which potential temperature ( $\theta$ ) changes by 0.2°C from the 10-dbar depth (de Boyer Montégut et al. 2007; Mignot et al. 2007; 2012). MLD is defined as the depth at which potential density ( $\sigma_\theta$ ) increases from the 10-dbar depth by the increment equivalent to a temperature decrease of  $\Delta\theta = 0.2^\circ\text{C}$  at a fixed salinity ( $S$ ), that is,

$$\Delta\sigma_\theta = \Delta\theta \left( \frac{\partial\sigma_\theta}{\partial\theta} \right)_s. \quad (3.1)$$

Barrier layer thickness (BLT) is defined as,

$$BLT = \begin{cases} ILD - MLD & (\text{if } ILD > MLD) \\ 0 & (\text{if } ILD < MLD) \end{cases}. \quad (3.2)$$

### 3.3 Seasonality and Persistence of Barrier Layer

The BLs in the subtropical Pacific from MOAA\_GPV were broadly distributed in winter and showed clear seasonality (Fig. 3.1). In the subtropical North Pacific, BLs thicker than 20 dbar existed in boreal winter at 10°–25°N, 160°E–130°W in association with an SSS front lying on the equator side of the SSS maximum, that is, the NPTW formation region (Fig. 3.1a). The SSS front weakened and BLs disappeared in boreal summer (Fig. 3.1b). Similar seasonality of BL distribution was seen in the subtropical South Pacific. In austral winter, BLs were formed in the SSS front region at 5°–20°S, 150°–110°W, which was located on the equator side of the SSS maximum, that is, SPTW formation region (Fig. 3.1d). These BLs also disappeared in austral summer as in the North Pacific, although the associated SSS front did not weaken (Fig. 3.1c). Such seasonality and distribution of BLs are consistent with the previous results based on the World Ocean Atlas climatology (Sprintall and Tomczak 1992; Sato et al. 2004; 2006). The seasonality of BLs in the tropical region differed from that in the subtropical regions. In the western tropical Pacific, thick BLs (BLT > 20 dbar) were distributed at 10°S–10°N west of the date line throughout a year (Fig. 3.1). Since we focus on BLs in the subtropical Pacific in this study, these BLs in the tropical Pacific

will not be pursued in this thesis. In the South Pacific, BLs were also formed at 25°–40°S, 125°–85°W in the SSS front region poleward of the SSS maximum in austral winter (Fig. 3.1d). These are considered to be artificial BLs produced by interpolation processes of MOAA\_GPV data because most Argo profiles in this region did not detect BLs (not shown).

To further investigate the BLs in the subtropical regions using Argo float profiles, we defined two boxes, the Northern Box at 10°–25°N, 155°E–130°W and the Southern Box at 5°–20°S, 155°–100°W. The distribution of BLs observed by Argo floats in the two boxes corresponded well to the SSS fronts and showed the same seasonality as demonstrated by MOAA\_GPV (Fig. 3.2). In the Northern Box, the SSS front was stronger and was about 5° wide meridionally in boreal winter (Fig. 3.2a). BLs thicker than 10 dbar were observed frequently within the SSS front and much less outside the front. In boreal summer, BLs were observed infrequently both within and outside the SSS front (Fig. 3.2b). In the Southern Box, thicker BLs were observed within the SSS front in austral winter (Fig. 3.2d). The number of BLs decreased greatly in austral summer, although the SSS front did not weaken (Fig. 3.2c).

Based on the close relationship between winter BLs and the SSS front, we examine the seasonal variation of BLs in the SSS front in more detail. Since MOAA\_GPV grid points with horizontal SSS gradient higher than  $6 (5) \times 10^{-7} \text{ m}^{-1}$  in the Northern (Southern) Box mainly corresponded to the winter BLs (Fig. 3.3), these grid points are considered as the SSS front in the following part of this chapter. In the SSS front in the Northern Box, both the number of Argo profiles with BLs and the observed BLT were at a maximum in February (Figs. 3.4a and 3.4b). Note that the frequency of Argo profiles with BLT > 10 dbar was about 35% even in winter (Fig. 3.4a), which indicates that BLs had patchy or porous distribution, as suggested by the previous studies (Sato et al. 2004; Mignot et al. 2009). In addition, Argo floats, which typically repeat observations at 10-day interval (Roemmich et al. 2004), did not observe BLs continuously in about 75% of total cases (Fig. 3.5a). This implies that the typical temporal scale of BLs is around 10 days and is shorter than that of 12–25 days in the western equatorial Pacific (Sprintall and McPhaden 1994).

In the SSS front in the Southern Box, BL frequency was at a maximum in August (Fig. 3.4c). The observed BLT was also largest in August, showing similar seasonality as in the Northern Box (Fig. 3.4d). The frequency of Argo profiles was about 35%

even in austral winter, indicating again the patchiness of BLs distribution. In addition, the time scale of most BLs was around 10 days in about 70% of total cases, as in the Northern Box (Fig. 3.5b).

### **3.4 Formation Mechanism of Barrier Layer**

Previous studies have suggested two processes as the formation mechanism of subtropical BLs: subsurface salinification due to TW subduction (Sato et al. 2004; 2006) and the combination of surface freshening by poleward Ekman transport and BL growth (e.g., Mignot et al. 2007). These two processes were examined individually, and both of them were not likely to be the primal mechanism of subtropical BL formation (Secs. 3.4.1 and 3.4.2). This fact led to the hypothesis that BLs are formed mainly through the tilting of SSS front. Its possibility was examined using Argo data (Sec. 3.4.3) and the output data of an OGCM (Sec. 3.4.4).

#### **3.4.1 Contribution of Tropical Water Subduction**

For the investigation of the relationship between the BL formation and subduction of TWs, the horizontal resolution of Argo profiling floats, which is  $3^{\circ} \times 3^{\circ}$  on average, is not sufficient. Thus, two meridional sections were analyzed, which were obtained under the World Ocean Circulation Experiment Hydrographic Programme (WHP) in winter : the P16N section along  $152^{\circ}\text{W}$  in the North Pacific occupied in February to March, 2006 and the P17S section along  $135^{\circ}\text{W}$  in the South Pacific observed in July to August, 1991. In the P16N section, BLs thicker than 70 dbar were formed at  $18^{\circ}$ – $19^{\circ}\text{N}$  (Fig. 3.6), due to salinity stratification within the isothermal layer (Fig. 3.6b). The vertical profile at  $19^{\circ}\text{N}$  showed that dissolved oxygen within BL was oversaturated and had vertically uniform value including above mixed layer, while salinity increased with depth within BL (Fig. 3.7). If this BL were formed through the salinification in association with the subduction of NPTW as suggested by previous studies, dissolved oxygen would decrease during subduction process. However, such decreasing of dissolved oxygen within BL was not seen from this section (Fig. 3.6c).

In the P17S section, BLs with thickness of 30–70 dbar were formed at  $10^{\circ}$ – $13^{\circ}\text{S}$  and  $15^{\circ}\text{S}$  (Fig. 3.8). Within the BL at  $10^{\circ}\text{S}$  near an SSS front, salinity increased downward, while temperature was almost uniform (Figs. 3.8b and 3.9a). On the other hand, dissolved oxygen was oversaturated (106–111%) throughout the BL and had

almost constant value throughout the isothermal layer (Figs. 3.8c and 3.9b). Thus, high salinity water within BLs is unlikely associated with subduction of SPTW, as in the P16N section.

### 3.4.2 Surface Freshening

The surface freshening in this SSS front region is attributable to precipitation and poleward Ekman advection of fresher water. To examine the contributions of these two effects, we use the mixed layer salinity (MLS) budget equation of Ren and Riser (2009),

$$\frac{\partial S_m}{\partial t} = \frac{-PS_m}{h_m} - \mathbf{u}_e \cdot \nabla S_m + \text{other terms}, \quad (3.3)$$

where  $S_m$  is MLS,  $t$  is time,  $P$  is precipitation,  $h_m$  is MLD,  $\mathbf{u}_e$  is Ekman velocity, and  $\nabla$  is the horizontal differential operator. Ekman velocity  $\mathbf{u}_e$  was estimated from wind stress data as

$$\mathbf{u}_e = \frac{1}{\rho_0 f h_m} (\tau^y, -\tau^x), \quad (3.4)$$

where  $\tau^x$  and  $\tau^y$  are zonal and meridional wind stresses (positive eastward and northward),  $f$  is the Coriolis parameter, and  $\rho_0$  is the reference density of seawater, taken to be  $1025 \text{ kg m}^{-3}$ . “Other terms” include the effects of evaporation ( $ES_m/h_m$ ;  $E$  is evaporation), geostrophic advection ( $-\mathbf{u}_g \cdot \nabla S_m$ ;  $\mathbf{u}_g$  is geostrophic velocity), and entrainment ( $-w_e \Delta S/h_m$ ;  $w_e$  is entrainment velocity, and  $\Delta S$  is the difference between MLS and the salinity at 20 dbar below the mixed layer base). These work to increase MLS in the SSS front region (Chapter 2) and are neglected. Both terms of precipitation and Ekman advection in Eq. (3.3) contain MLD ( $h_m$ ) in their denominator, and these terms multiplied by  $h_m$  represent advection of salt. We estimated the salt advectons by precipitation ( $A_{prec}$ ) and Ekman advection ( $A_{Ek}$ ) as

$$A_{prec} = -PS_m \quad (3.5)$$

and

$$A_{Ek} = -\frac{1}{\rho_0 f} \nabla S_m \cdot (\tau^y, -\tau^x), \quad (3.6)$$

respectively, since it can be expected that the value of  $h_m$  in Eqs. (3.3) and (3.4) depends on whether BL already exists or not.

In the Northern Box, these two effects were always negative and showed seasonal variations (Fig. 3.10a).  $A_{Ek}$  was large in boreal winter (November–January) and small in spring to summer (May–August).  $A_{prec}$  had a smaller amplitude than  $A_{Ek}$  and was large in boreal summer to early winter (August–December).  $A_{Ek}$  exceeded  $A_{prec}$  except in August and September, and was two to four times greater in magnitude than  $A_{prec}$  in boreal winter when BLs were formed.

$A_{Ek}$  was dominated by its meridional component, that is, meridional Ekman salt advection ( $\frac{1}{\rho_0 f} \frac{\partial S_m}{\partial y} \tau^x$ ; not shown). When the two factors contributing to the meridional Ekman salt advection,  $\partial S_m / \partial y$  and  $\tau^x$ , were examined, their amplitudes were at maximum in November and December, respectively (Figs. 3.11a and 3.11b), which resulted in the peak of  $A_{Ek}$  in December. The seasonal variation of  $\partial S_m / \partial y$  in the Northern Box reflected mainly that of MLS in the MLS minimum region south of the SSS front (Figs. 3.12a and 3.12b), which is controlled mainly by precipitation in the Intertropical Convergence Zone (Bingham et al. 2010; Yu 2011). Freshening in the MLS minimum in boreal winter strengthened the SSS front and contributed to the enhancement of the Ekman salt advection.

In the Southern Box,  $A_{Ek}$  was -4 m/month with a small seasonal variation and always exceeded  $A_{prec}$  (Fig. 3.10b). It was dominated by its meridional component (not shown), and the poleward Ekman advection of fresher water ( $\frac{1}{\rho_0 f} \frac{\partial S_m}{\partial y} \tau^x$ ) was dominant as the surface process, as in the North Pacific. Zonal wind stress was strong in austral winter (July–September; Fig. 3.11d), as in the Northern Box. On the other hand,  $\partial S_m / \partial y$  exhibited an opposite seasonal variation, being large in austral summer–fall and small in austral winter (Fig. 3.11c), which was determined by the MLS variation near 5°–10°S on the equator side of the SSS front (Figs. 3.12c and 3.12d).

This resulted in the small seasonal variation of  $A_{Ek}$ .

Thus, the meridional Ekman advection was dominant as the surface process both in the North and South Pacific. However,  $A_{Ek}$  in the South Pacific did not show a clear seasonal variation.  $A_{Ek}$  in the North Pacific was large in boreal winter, although its peak (November–January) was a little different from that of BLs (February). Therefore, the seasonality of BL formation in the subtropical Pacific cannot be fully explained by Ekman advection. Although previous studies (e.g., Mignot et al. 2007) suggested that the seasonality of BLs can be explained by their growth from autumn to winter, their temporal scale estimated from Argo floats was too short (Sec. 3.3.1).

These observational facts suggest that BLs are formed due primarily to the tilting of SSS front, as pointed out by Cronin and McPhaden (2002) for the equatorial Pacific, because there is poleward Ekman flow near the sea surface across the zonal SSS front (Fig. 3.13). Tilting of an SSS front with sufficiently large ILD/MLD could produce salinity stratification in the isothermal layer and leave a BL in its lower part. If such mechanism is dominant, thicker BLs are likely to be formed above the base of deeper isothermal layer, which is consistent with the observed seasonality of BLs and the correspondence of BLT to ILD on seasonal time scale (Figs. 3.4 and 3.14). In the next subsection, the possibility of BL formation through the tilting of SSS front is examined.

### 3.4.3 Possibility of BL Formation through the Tilting of SSS Front

For the BL formation through the tilting of meridional SSS front, it is necessary that the contribution of the meridional SSS gradient to the meridional sea surface density gradient across the SSS front is much larger than that of the meridional SST gradient. In other words, meridional density ratio  $R_y$  (Tippins and Tomczak 2003) defined as

$$R_y = \frac{\alpha \partial T_s / \partial y}{\beta \partial S_s / \partial y} \quad (3.7)$$

must satisfy  $-1 < R_y < 1$  at the SSS front, where  $\alpha$  is thermal expansion coefficient,  $\beta$  is salinity contraction coefficient,  $T_s$  is SST and  $S_s$  is SSS. If this condition is satisfied, the mixed layer can become shallower than the isothermal layer as a result of the tilting of SSS front.

In the North Pacific, the magnitude of  $R_y$  was small in boreal winter in a zonal band with a meridional width of about  $5^\circ$  in  $10^\circ$ – $20^\circ$ N,  $120^\circ$ E– $150^\circ$ W (Fig. 3.15a). This band corresponded to both the SSS front and the BL distribution (Figs. 3.1a and 3.2a). In the South Pacific, the  $R_y$  condition was satisfied in austral winter in  $10^\circ$ – $18^\circ$ S,  $170^\circ$ – $100^\circ$ W (Fig. 3.15d), which also corresponded to both the SSS front and the BL distribution (Figs. 3.1d and 3.2d). These features imply that BLs were formed due to the tilting of SSS front.

The small  $R_y$  region also existed in association with the SSS front in summer in both the North and South Pacific (Figs. 3.15b and 3.15c), but BLs were formed infrequently there (Figs. 3.1b, 3.1c, 3.2b, and 3.2c). This is probably because the preexisting isothermal layers were too shallow. The seasonality of BLs corresponded well to that of ILD (Figs. 3.4 and 3.14); in the Northern (Southern) Box, BLs were most frequently observed in February (August) when the isothermal layer was deepest, and infrequently in boreal (austral) summer when the isothermal layer was shallow.

Thus, BL formation in the subtropical Pacific is attributable primarily to the tilting of the SSS front, and its seasonality is governed by that in the depth of isothermal layer, which preconditions the BL formation. After deepening of isothermal/mixed layers that typically occurs on a timescale of several days (e.g., de Boyer Montégut et al. 2004; Oka et al. 2007) in the SSS front region, the vertical shear of horizontal flow tilts the SSS front to produce BLs that mostly lasts for shorter than 10 days (Fig. 3.5). Such events are expected to occur intermittently throughout the SSS front region (Fig. 3.2) and emerge in the smoothed climatological pictures (Fig. 3.1; Sato et al. 2004; 2006).

#### **3.4.4 Verification of the Tilting of SSS Front by a High Resolution OGCM**

To further assess the BL formation through the tilting of SSS front, output data of COCO were analyzed. In the Northern Box, BLs showed the same seasonality as detected by Argo profiles (Fig. 3.16). In boreal winter, thick BLs are formed zonally in  $10^\circ$ – $15^\circ$ N along the SSS front, showing filamentary distribution (Figs. 3.16a and 3.16c). BLs with BLT = 20–40 dbar were also distributed patchily. These BLs were distributed adjacent to strong horizontal SSS gradient (Fig. 3.16e). In boreal summer, thick BLs disappeared and BLs were formed infrequently in association with locally strong SSS gradients (Figs. 3.16b, 3.16d, and 3.16f). This spatial distribution of BLs

is consistent with the suggestion by Sato et al. (2004, 2006) that spatial scale of BLs reflects that of sharp SSS fronts.

In the Southern Box, BLs also showed a consistent seasonality with Argo profiles as in the Northern Box (Fig. 3.17). In austral winter, they were formed zonally in 10°–15°S along the SSS front (Fig. 3.17b). Thick BLs were often associated with strong SSS gradients (Figs. 3.17d and 3.17f). These thick BLs disappeared in austral summer and patchy BLs are formed adjacent to sharp SSS fronts (Figs. 3.17a, 3.17c, and 3.17e). This correspondence of distribution between SSS fronts and BLs in the Southern Box was also consistent with Sato et al. (2004, 2006).

To check if SSS fronts were strong enough for BL formation through the tilting process, I calculated density ratio in the direction to which SSS front is strongest,  $R_\rho$ , as

$$R_\rho = \frac{\alpha \left( \nabla T_s \cdot \frac{\nabla S_s}{|\nabla S_s|} \right)}{\beta |\nabla S_s|}. \quad (3.8)$$

The value of  $|R_\rho|$  was small in almost the entire area in both boxes throughout a year as shown in MOAA\_GPV (Fig. 3.18), indicating that the vertical shear of salinity advection can lead to shallower salinity-stratified mixed layers than isothermal layers.

To further investigate whether BLs were associated with the tilting of SSS front, the difference in horizontal salinity advection between at 10 dbar and ILD ( $\Delta ADV$ ) was calculated as

$$\Delta ADV = -(\mathbf{u} \cdot \nabla S)_{10\text{dbar}} + (\mathbf{u} \cdot \nabla S)_{ILD}, \quad (3.9)$$

where  $\mathbf{u}$  is horizontal velocity, and  $S$  is salinity. Negative value of  $\Delta ADV$  means the vertical shear of salinity advection within the isothermal layer, which leads to salinity stratification through the tilting of SSS front.

In the Northern Box,  $\Delta ADV$  tended to show a large negative value within BL regions in association with strong SSS gradient, while it showed a small value where BLs were not formed (Figs. 3.19a and 3.19b). This tendency also can be seen in the Southern Box (Figs. 3.19c and 3.19d).  $\Delta ADV$  showed a large negative value where BLs were formed and a small value in the regions without BLs.

Vertical shear of velocity across SSS fronts ( $\Delta V$ ) can be divided into geostrophic ( $\Delta V^g$ ) and ageostrophic ( $\Delta V^a$ ) components as

$$\underbrace{(\mathbf{u}_{10dbar} - \mathbf{u}_{ILD})}_{\Delta V} \cdot \frac{\nabla S_s}{|\nabla S_s|} = \underbrace{(\mathbf{u}_{10dbar}^g - \mathbf{u}_{ILD}^g)}_{\Delta V^g} \cdot \frac{\nabla S_s}{|\nabla S_s|} + \underbrace{(\mathbf{u}_{10dbar}^a - \mathbf{u}_{ILD}^a)}_{\Delta V^a} \cdot \frac{\nabla S_s}{|\nabla S_s|} \quad (3.10)$$

using thermal wind relationship,

$$u_{10dbar}^g - u_{ILD}^g = \int_{h=ILD}^{10dbar} \frac{g}{f\rho_0} \frac{\partial \rho}{\partial y} dh, \quad v_{10dbar}^g - v_{ILD}^g = -\int_{h=ILD}^{10dbar} \frac{g}{f\rho_0} \frac{\partial \rho}{\partial x} dh \quad (3.11)$$

where  $g$  is the gravity constant,  $\rho$  is density,  $h$  is depth, and subscripts  $g$  and  $a$  denote geostrophic and ageostrophic components, respectively. In the Northern Box,  $\Delta V$  showed a fine spatial structure (Figs. 3.20a and 3.20b). The magnitude of  $\Delta V^g$  is small compared to  $\Delta V$  (Figs. 3.20c and 3.20d), and the spatial distribution of  $\Delta V$  corresponded well to that of  $\Delta V^a$  (Figs. 3.20e and 3.20f), indicating that vertical shear across SSS fronts is dominated by ageostrophic flow, that is Ekman flow. This dominant contribution of  $\Delta V^a$  to  $\Delta V$  was also seen in the Southern Box (Fig. 3.21). Thus, BLs tend to be formed where the strong vertical shear of salinity advection occurs, which results from the local strong SSS front and the vertical shear of velocity due to Ekman flow, strongly supporting the hypothesis of the subtropical BL formation through the tilting of SSS front due to Ekman advection in the previous subsection.

### 3.5 Interannual Variability of Winter Barrier Layer

Frequency and thickness of thick BLs in winter showed interannual variation both in the Northern Box and the Southern Box, with a different tendency between the two hemispheres (Fig. 3.22). In the Northern Box, the BL frequency was lowest in 2009, while BLT was largest in the same year (Figs. 3.22a and 3.22b). The two quantities showed a negative correlation (coefficient  $R = -0.53$ )<sup>1</sup>, a relation that was not seen on the seasonal timescale (Fig. 3.4). On the other hand, the two quantities showed a positive correlation ( $R = 0.73$ ) in the Southern Box (Figs. 3.22c and 3.22d). In other words, thicker BLs tend to be distributed sparsely in the Northern Box, while thicker BLs tend to be distributed densely in the Southern Box.

---

<sup>1</sup> Based on  $t$ -distribution, a correlation for sample size  $N = 10$  is significant on 90% and 95% confidence when the magnitude of  $R$  is larger than 0.55 and 0.63, respectively (Fisher 1950).

In the Northern Box, winter BLT showed a higher positive correlation with winter ILD ( $R = 0.78$ ) than with winter MLD ( $R = 0.26$ ; Figs. 3.22b and 3.23a). Since BLT is defined as the difference between MLD and ILD [Eq. (3.2)], these correlations indicated that interannual variation of winter BLT reflected that of winter ILD rather than winter MLD. On the other hand, the winter BL frequency showed a positive correlation with the intensity of winter SSS front ( $R = 0.63$ ; Figs. 3.22a and 3.23b), implying that when the SSS front is strong, BLs are formed frequently and distributed broadly.

In the Southern Box, both winter MLD and ILD showed a positive correlation with winter BLT ( $R = 0.57$  and  $0.87$ , respectively; Figs. 3.22d and 3.23c) as in the Northern Box, indicating dominant contribution of winter ILD to winter BLT on interannual time scale. Not as in the Northern Box, winter BL frequency did not show a correlation with the intensity of SSS front ( $R = -0.08$ ; Fig. 3.23d), while it was positively correlated with winter ILD ( $R = 0.55$ ; Fig. 3.23c). This means that when winter isothermal layers are deep, BLs are formed frequently and they tend to be thick.

The interannual variations in the Northern Box were likely to be related to the Pacific Decadal Oscillation (PDO; Mantua et al. 1997; Fig. 3.24). The winter BL frequency was highly correlated with the PDO index with a lag of one year ( $R = 0.81$ ; Fig. 3.24b). The intensity of SSS front also showed a positive correlation with the PDO index ( $R = 0.72$ ; Fig. 3.24b), implying that the interannual variation of winter BL frequency in the Northern Box may reflect the PDO-related variation of the SSS front. On the other hand, both winter BLT and winter ILD were negatively correlated with the PDO index ( $R = -0.62$ , and  $-0.66$  with a lag of one year; Fig. 3.24c). In addition,  $\tau^x$  in the Northern Box where the north-easterly trade wind is dominant was negative and showed a positive correlation with the PDO index ( $R = 0.59$ ; Figs. 3.25a and 3.25b). This is consistent with Carton et al. (2008), who demonstrated that winter ILD in the subtropical North Pacific tended to be small in association with weakening of the trade winds during the warm phase of the PDO.

Winter BLT and ILD in the Southern Box were negatively correlated with the Niño3 index ( $R = -0.31$  and  $-0.49$ ; Fig. 3.26c). This is consistent with Carton et al. (2008) demonstrating that ILD tended to be small (large) in the subtropical South Pacific during El Niño (La Niña) events. In the Southern Box where the south-easterly trade wind is dominant,  $\tau^x$  showed a positive correlation with the Niño3 index ( $R = 0.53$ ; Figs. 3.25c and 3.25d), as previous studies demonstrated that the trade wind is

stronger during La Niña events (e.g., Wang and McPhaden 2000). Thus, the interannual variation of winter BLs in the Southern Box may be affected by the ENSO through the intensity of easterly trade wind controlling winter ILD.

### **3.6 Discussion**

In Chapter 2, it was discussed that a part of subducted NPTW is entrained into the mixed layers above BLs south of its formation region, almost corresponding to subtropical BL region (Sec. 2.4; Fig. 2.18). On the other hand, high salinity water within BLs was not associated with the subduction of TWs, and BLs are formed intermittently through the tilting of SSS fronts within mixed layers (Sec. 3.4). When the entrainment term in Eq. (2.1) is calculated for the isothermal layer, it was also positive and increased isothermal layer salinity not only in the Northern Box but also in the Southern Box (not shown). Thus, the results in this chapter do not violate the discussion of the meridional overturning circulation of NPTW, and a part of subducted NPTW and SPTW is entrained into mixed layers within which shallow salinity stratification is formed intermittently.

This study proposed that formation and dissipation of BLs occur alternately within mixed layers on a short time scale in the subtropical Pacific. Since buoyancy is provided constantly within mixed layers, development of winter mixed layers will be greatly obstructed, and the exchange of heat and substances between surface and subsurface layers through entrainment will be reduced. This process can also modulate spiciness anomalies in the subsurface. To evaluate these effects, observation of mixing processes within BLs needs to be conducted in future.

### **3.7 Summary**

Seasonal and interannual variations and formation mechanisms of BLs in the subtropical North and South Pacific have been investigated using Argo profiles, MOAA\_GPV gridded Argo data, and the various surface flux data in 2003–12, hydrographic section data from the World Ocean Circulation Experiment Hydrographic Programme, and output data of an OGCM. BLs lying within the SSS fronts located on the equator side of SSS maxima were thickest and most frequent in winter, although they were observed by only about 35% of Argo profiles even in winter. In addition, a temporal scale of BLs was around 10 days. These features indicated that BLs in the

subtropical Pacific are transient phenomenon with small spatial scale.

To clarify the formation mechanisms of BLs in the subtropical Pacific, contribution of TW subduction and surface freshening suggested by previous studies were evaluated. Subduction of TWs has been considered as the subsurface salinification process, but the dissolved oxygen was saturated coherently within BLs. Poleward Ekman advection of fresher water was dominant as the surface freshening process, but cannot sufficiently explain the seasonality of BLs, particularly in the South Pacific. Temporal scale of BLs is also too short for their growth during cooling period. These facts suggested that BLs in the subtropical Pacific are formed primarily through the tilting of meridional SSS front due to the poleward Ekman flow near the sea surface. This idea was supported by the dominant contribution of meridional SSS gradient to the meridional sea surface density gradient and the correspondence between the BLT and ILD both on seasonal and interannual time scale. The analysis of OGCM also revealed that vertical shear of salinity advection within isothermal layers tends to occur where BLs are formed and that the vertical shear of flow results from that of ageostrophic one, supporting the BL formation through the tilting process caused by Ekman flow.

Interannual variation of BLs showed that thicker BLs tended to be distributed sparsely in the North Pacific, while they tended to be distributed densely in the South Pacific. In the North Pacific, winter BL frequency and BLT were related to the PDO through the intensity of SSS front and ILD, respectively. On the other hand, interannual variation of winter BLT in the South Pacific was related to that of winter ILD controlled by the ENSO-related easterly trade wind anomalies.

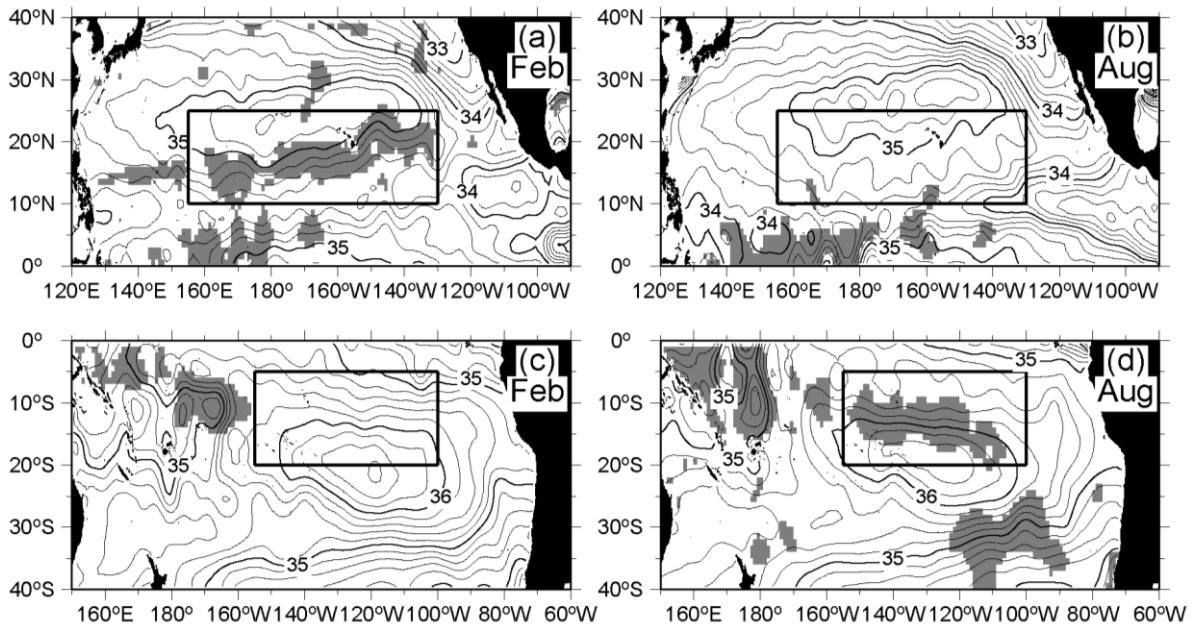


Fig. 3.1. Distributions of BLs thicker than 20 dbar (gray shading) and salinity at 10-dbar depth (contour) in February (a and c) and August (b and d) in the North Pacific (a and b) and the South Pacific (c and d), based on MOAA\_GPV averaged in 2003–12. Thick rectangles indicate the Northern Box (a and b) and the Southern Box (c and d). Note that a criterion of 20 dbar was used to detect BLs from MOAA\_GPV data (Figs. 3.1 and 3.3) and COCO (Figs. 3.16, 3.17, 3.18, 3.19, 3.20, and 3.21) and that of 10 dbar was used for Argo profiles (other figures). ©American Meteorological Society. Used with permission.

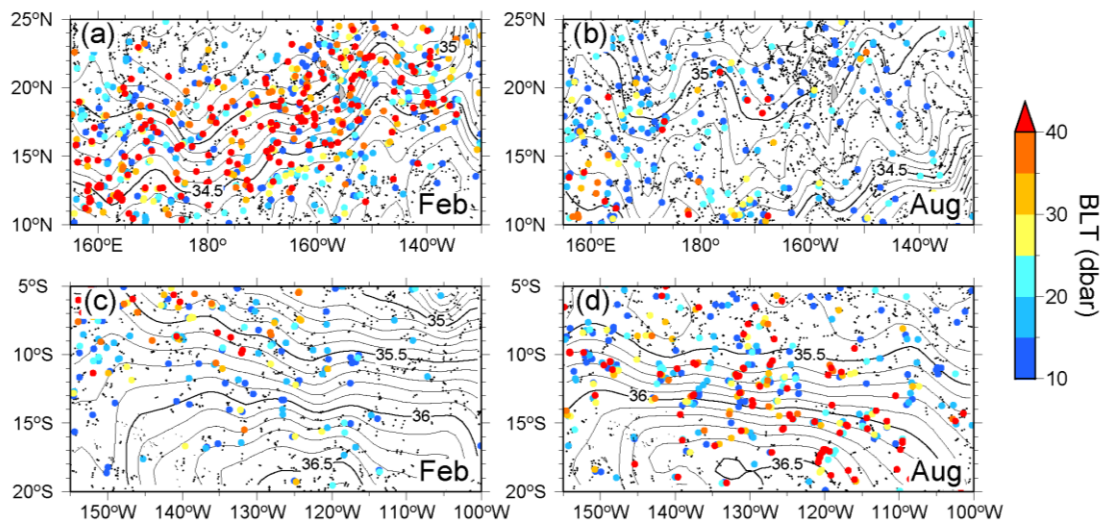


Fig. 3.2. Distributions of BLT (colored dots) from Argo profiles and salinity at 10-dbar depth (contour) from MOAA\_GPV in February (a and c) and August (b and d) of 2003–12 in the Northern Box (a and b) and the Southern Box (c and d). Small black dots indicate the position of Argo profiles without BLT > 10 dbar. ©American Meteorological Society. Used with permission.

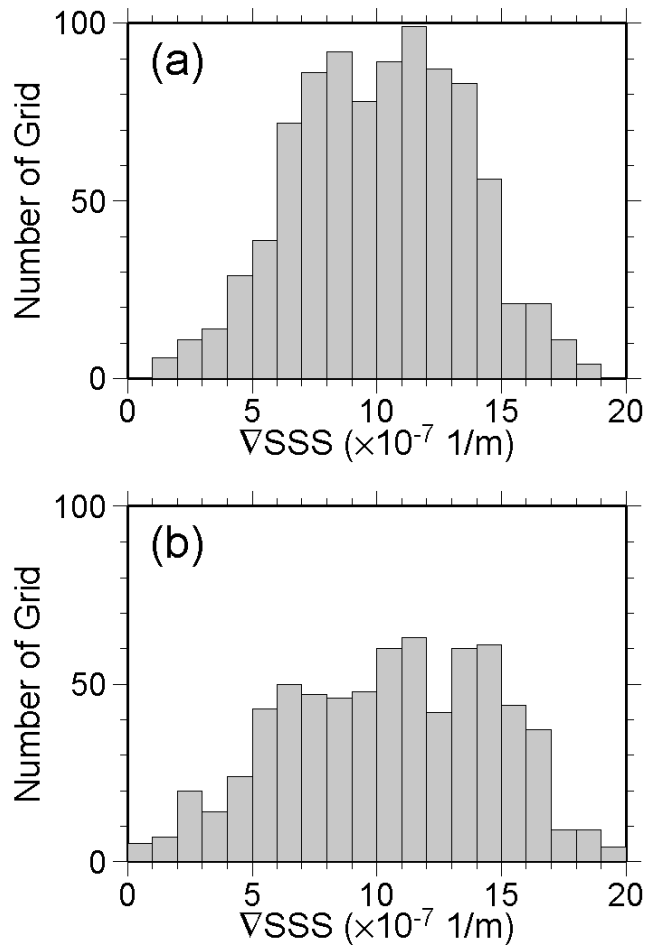


Fig. 3.3. Histogram of number of  $1^\circ \times 1^\circ$  grid points with BLT > 20 dbar with respect to the horizontal SSS gradient in (a) the Northern Box and (b) the Southern Box, calculated from average distributions from MOAA\_GPV in January–March (a) and July–September (b) during 2003–12. ©American Meteorological Society. Used with permission.

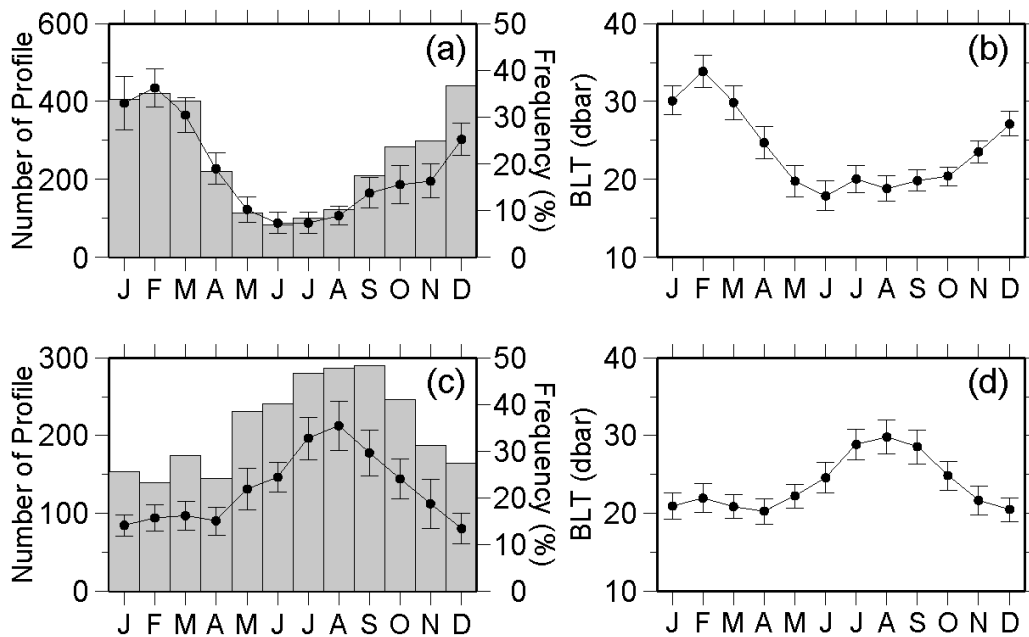


Fig. 3.4. (a) Monthly histogram (bars) of number of Argo profiles with BLT > 10 dbar and monthly average of their frequency (dots) and (b) monthly average of BLT from Argo profiles with BLT > 10 dbar, calculated for the SSS front in the Northern Box in during 2003–12. Vertical bars indicate the 95% confidence interval based on the standard deviation from Argo profiles with BLT > 10 dbar in each month during 2003–12. (c and d) Same as (a) and (b) but for the Southern Box. ©American Meteorological Society. Used with permission.

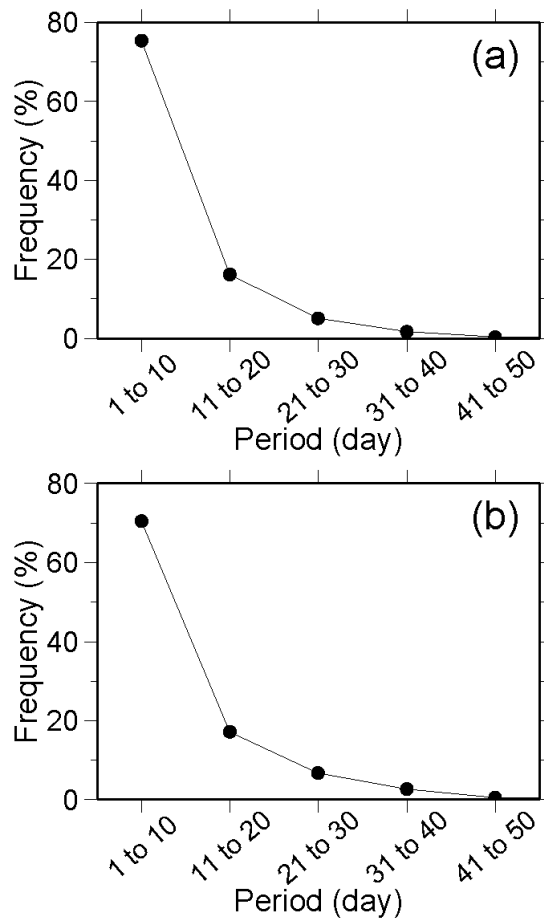


Fig. 3.5. Frequency of period for which each Argo float continuously observed BLT > 10 dbar in the SSS front in (a) the Northern Box and (b) the Southern Box during 2003–12. If, for example, an Argo float observes a BL on Jan. 1 for the first time and again on Jan. 11, and does not on Jan. 21, the period on the x axis is 11. ©American Meteorological Society. Used with permission.

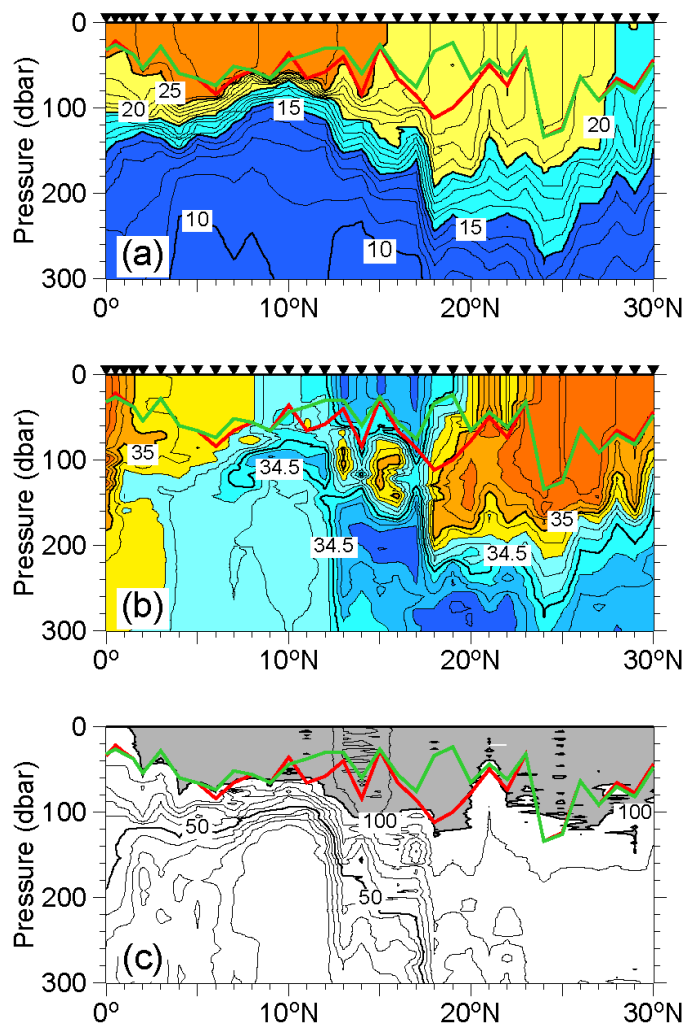


Fig. 3.6. Meridional distribution of (a) potential temperature ( $^{\circ}\text{C}$ ), (b) salinity, and (c) dissolved oxygen concentration (%) in WHP P16N section along  $152^{\circ}\text{W}$  observed in February to March, 2006. Thick green and red curves indicate MLD and ILLD, respectively. Triangles at the top of each panel indicate the locations of hydrographic stations. Gray shading in (c) denotes dissolved oxygen concentration higher than 100 %. ©American Meteorological Society. Used with permission.

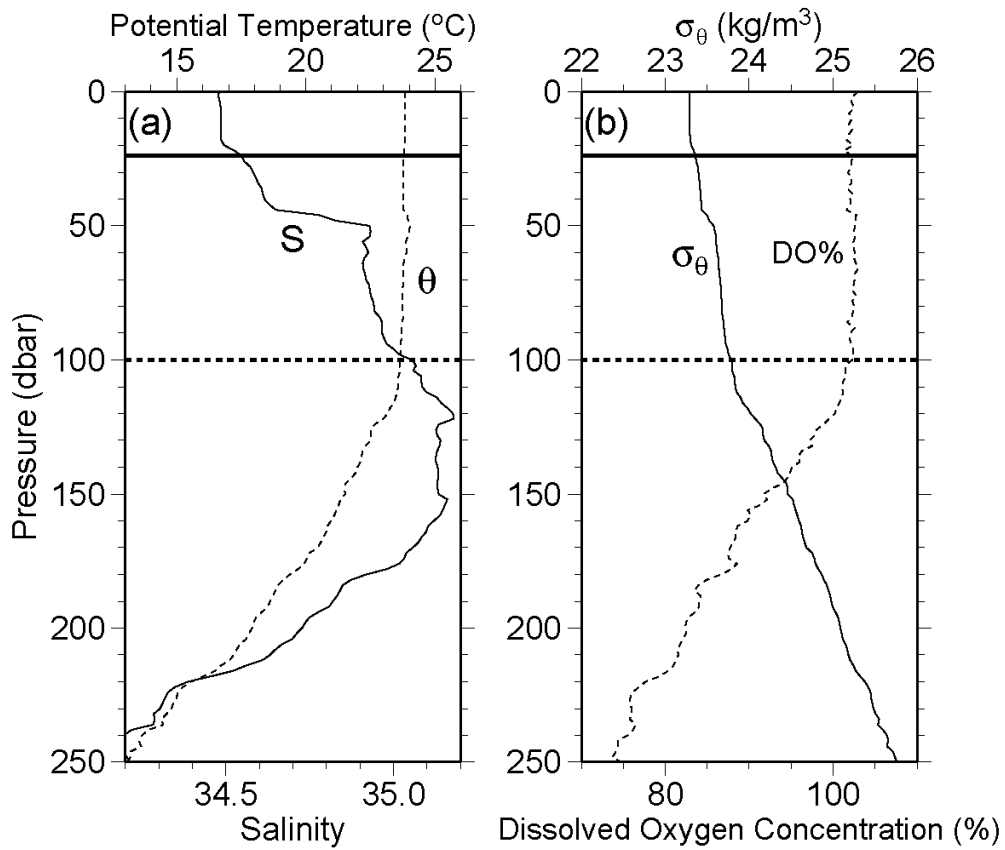


Fig. 3.7. Vertical profiles of (a) salinity (thin solid curve) and potential temperature (thin dashed curve) and (b) potential density (thin solid curve) and dissolved oxygen concentration (thin dashed curve) at 19°N in the P16N section. Thick solid and dashed lines denote MLD and ILD, respectively. ©American Meteorological Society. Used with permission.

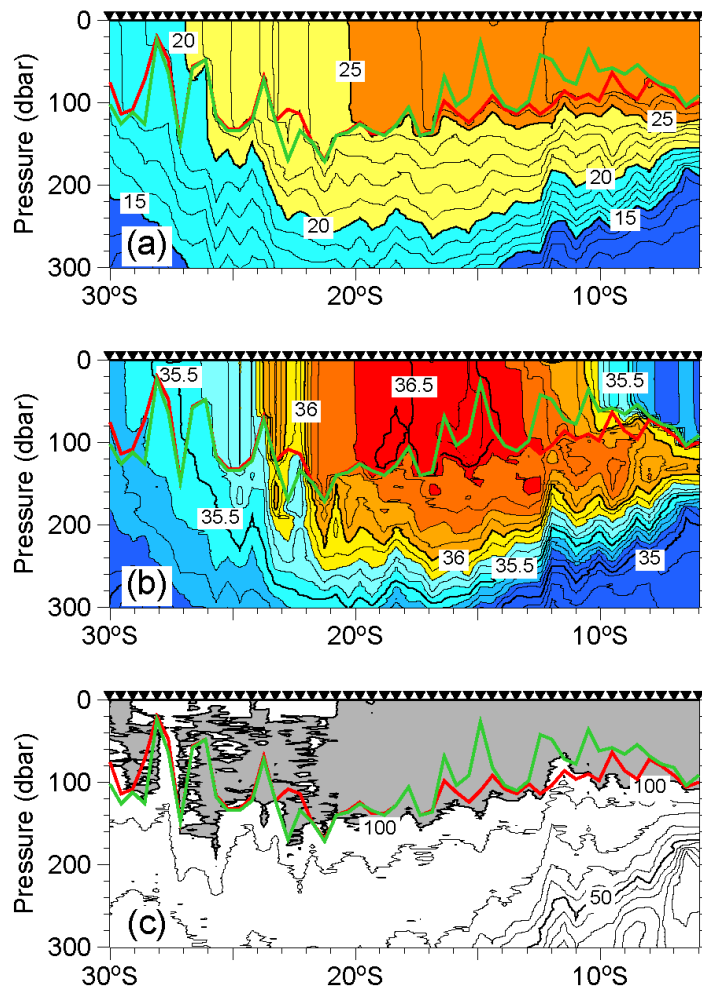


Fig. 3.8. As in Fig. 3.6, but for P17S section along 135°W observed in July to August, 1991. ©American Meteorological Society. Used with permission.

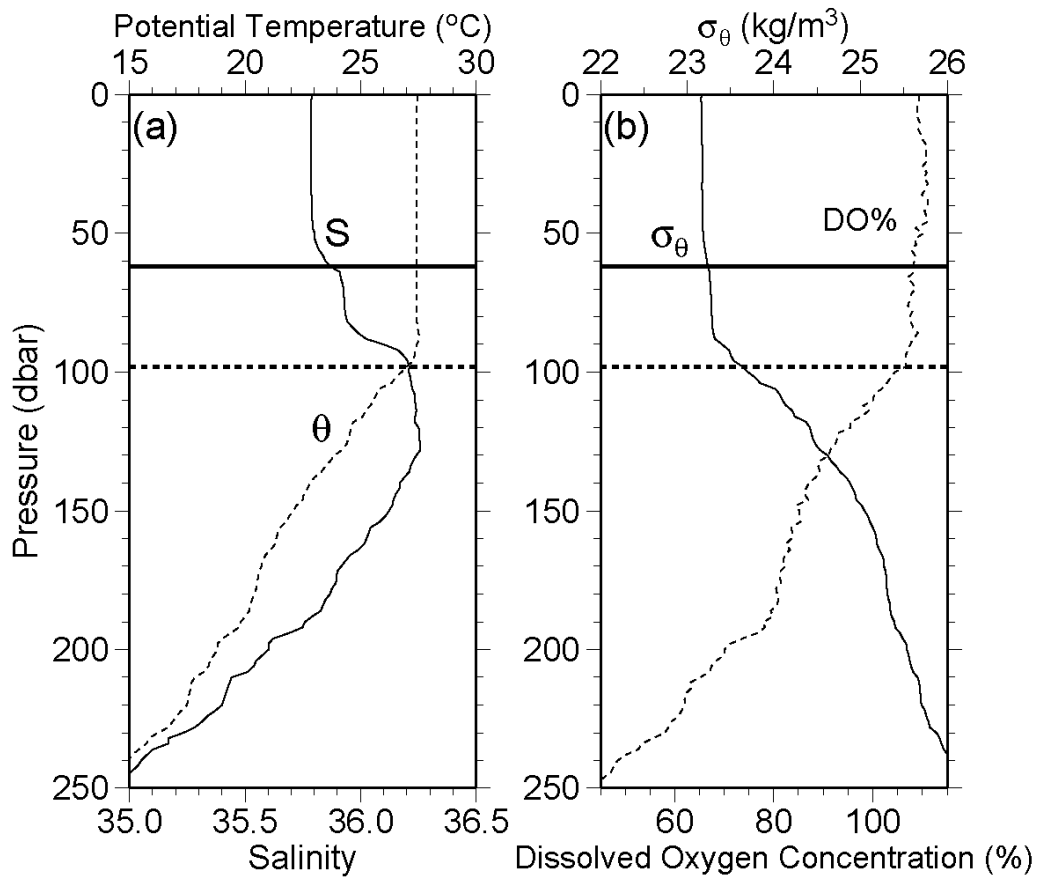


Fig. 3.9. As in Fig. 3.7, but for  $10^{\circ}\text{S}$  in the P17S section. ©American Meteorological Society. Used with permission.

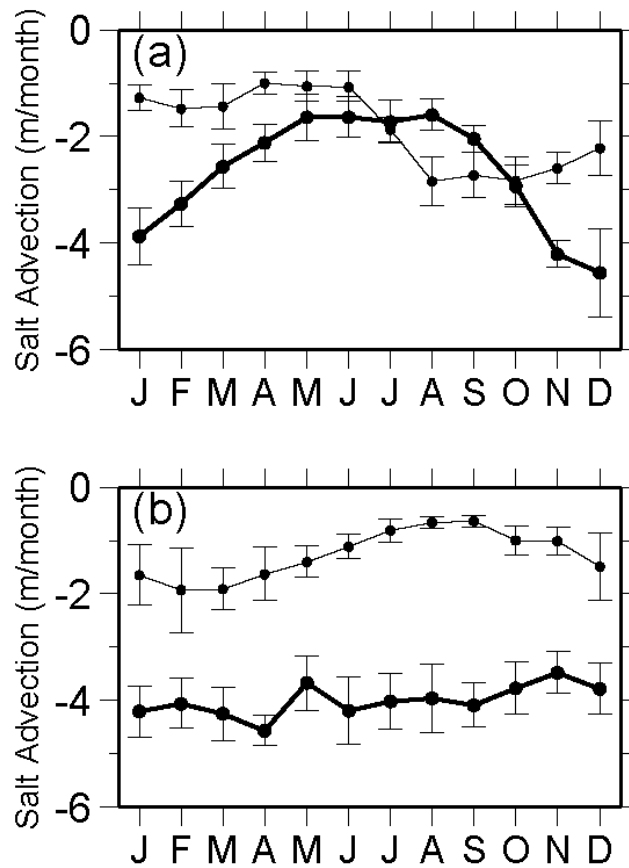


Fig. 3.10. Monthly average of  $A_{Ek}$  (thick curve) and  $A_{prec}$  (thin curve) in (a) the Northern Box and (b) the Southern Box during 2003–12. Vertical bars indicate the 95% confidence interval based on the standard deviation of each month during 2003–12. ©American Meteorological Society. Used with permission.

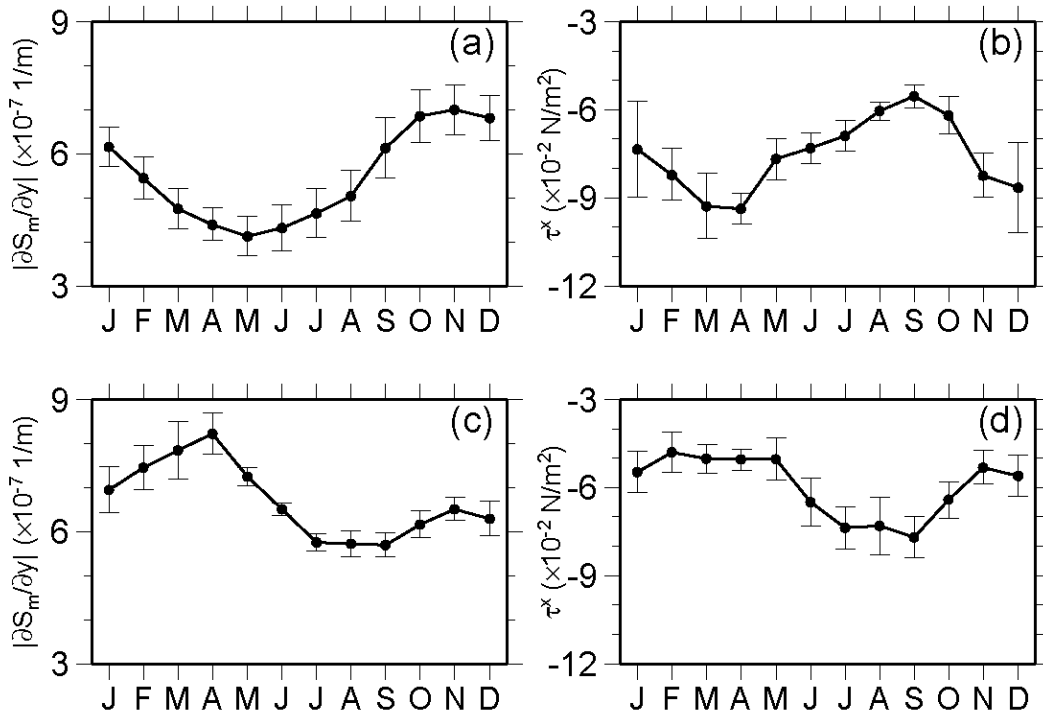


Fig. 3.11. (a) Monthly average of meridional MLS gradient magnitude from MOAA\_GPV and (b) zonal wind stress in the Northern Box during 2003–12. Vertical bars indicate the 95% confidence interval based on the standard deviation of each month during 2003–12. (c and d) Same as (a) and (b) but for the Southern Box. ©American Meteorological Society. Used with permission.

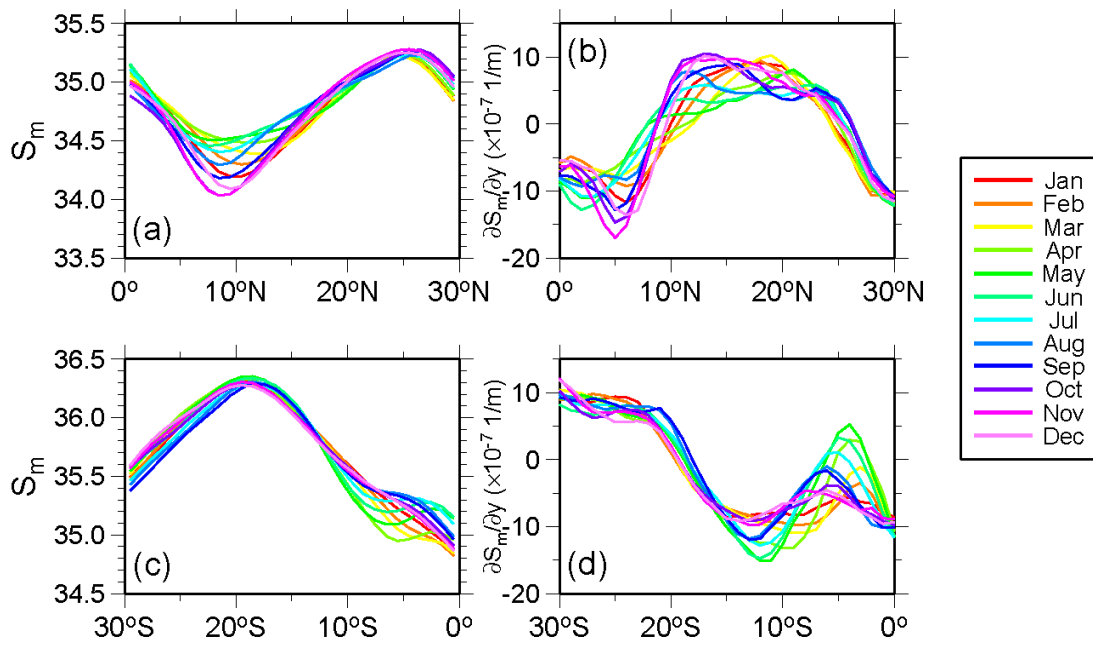


Fig. 3.12. (a and c) Meridional MLS variation during 2003–12 from MOAA\_GPV, averaged monthly at 155°E–130°W in the North Pacific (a) and at 155°–100°W in the South Pacific (c). (b and d) The same as (a) and (c), respectively, but for meridional MLS gradient. ©American Meteorological Society. Used with permission.

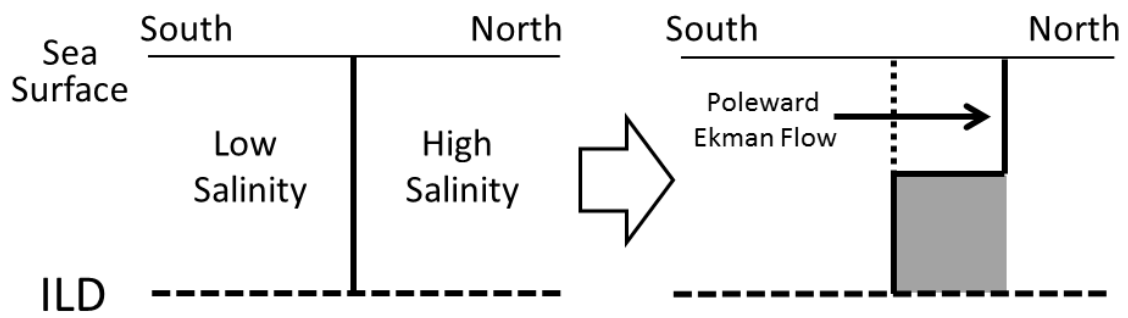


Fig. 3.13. Schematic diagram of BL formation through the tilting of SSS front in the North Pacific. Gray shading indicates formed BL. Thick line indicates an SSS front. ©American Meteorological Society. Used with permission.

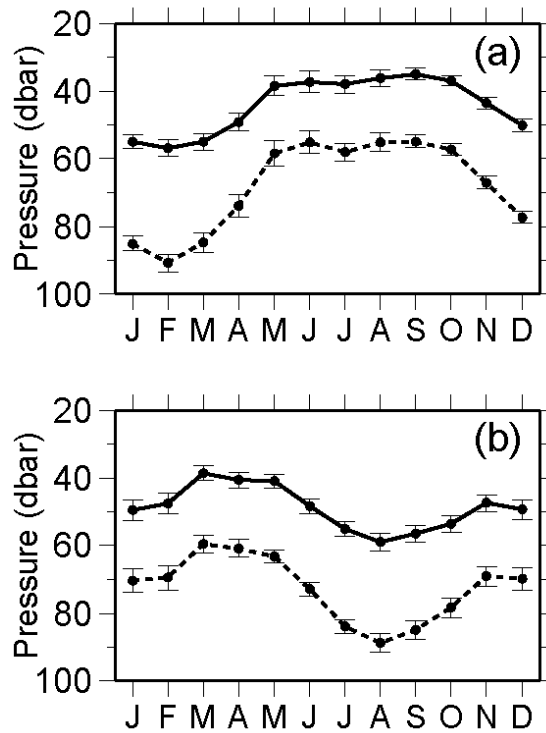


Fig. 3.14 Monthly average of MLD (solid curve) and ILD (dashed curve) observed by Argo floats in the SSS front in (a) the Northern Box and (b) the Southern Box during 2003–12. Vertical bars indicate the 95% confidence interval based on the standard deviation from Argo profiles with BLT > 10 dbar in each month during 2003–12. ©American Meteorological Society. Used with permission.

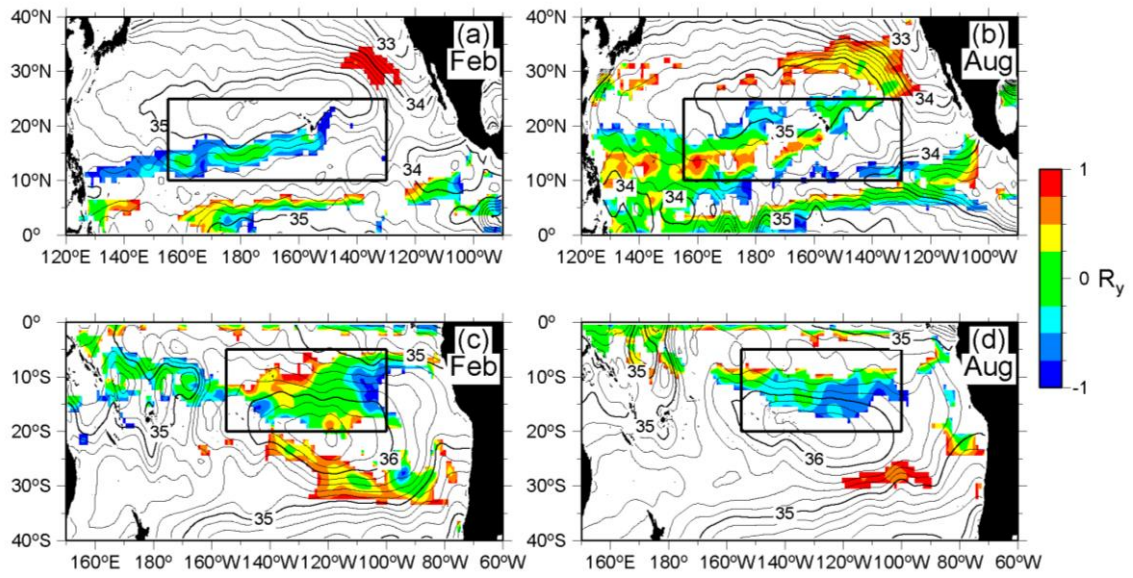


Fig. 3.15. Same as Fig. 3.1 except that color denotes  $R_y$  in regions where  $-1 < R_y < 1$  is satisfied. ©American Meteorological Society. Used with permission.

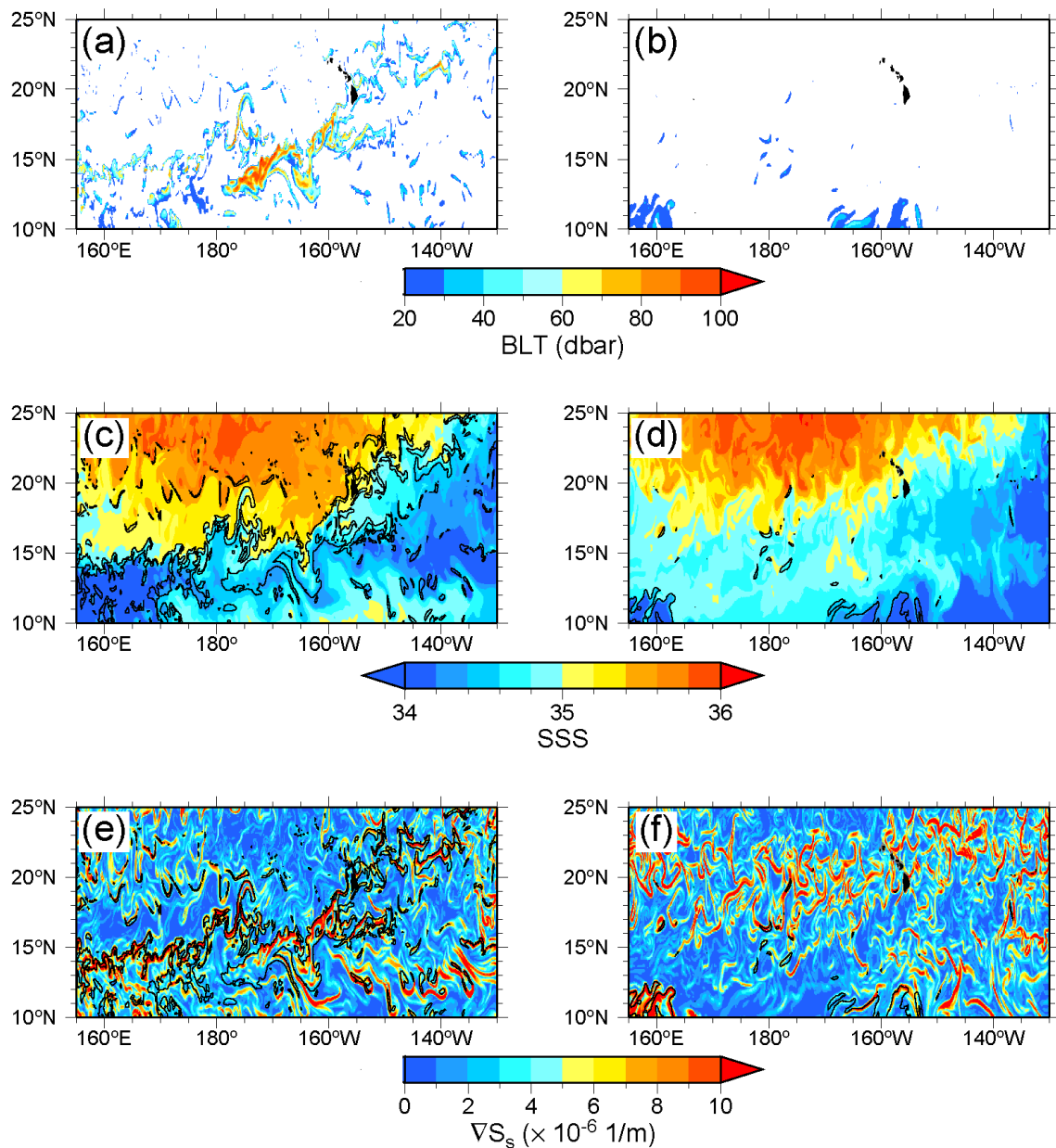


Fig. 3.16. (a, c, and e) Distribution of BLT where BLT > 10dbar (a), SSS (c), and  $\nabla S_s$  (e) in the Northern Box on Feb. 20, 2006 simulated by COCO. Contours in (c) and (e) indicate BLT = 20 dbar. (b, d, and f) Same as (a), (c), and (e), respectively, but for Aug. 19, 2006.

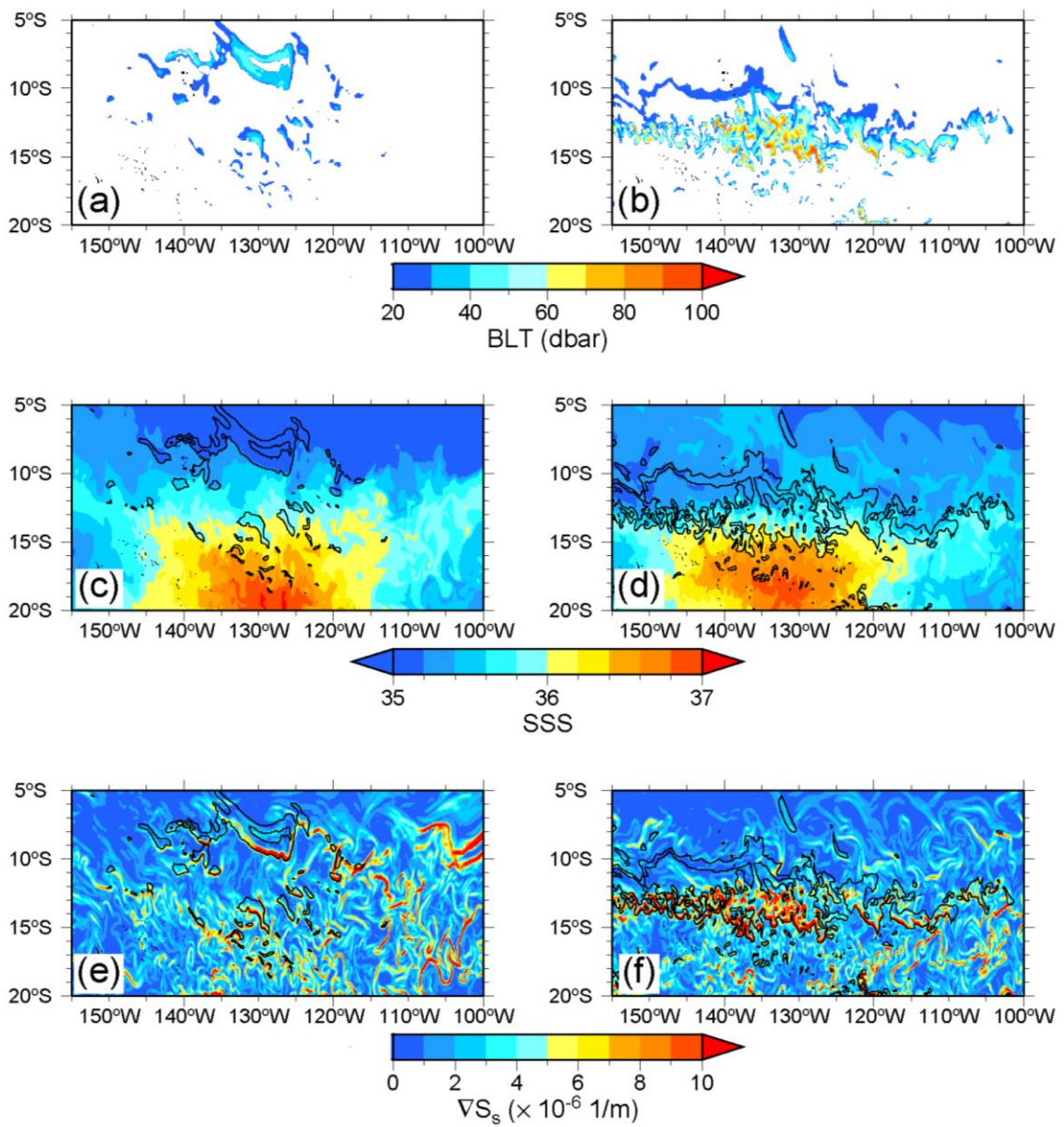


Fig. 3.17. As in Fig. 3.16 but for the Southern Box.

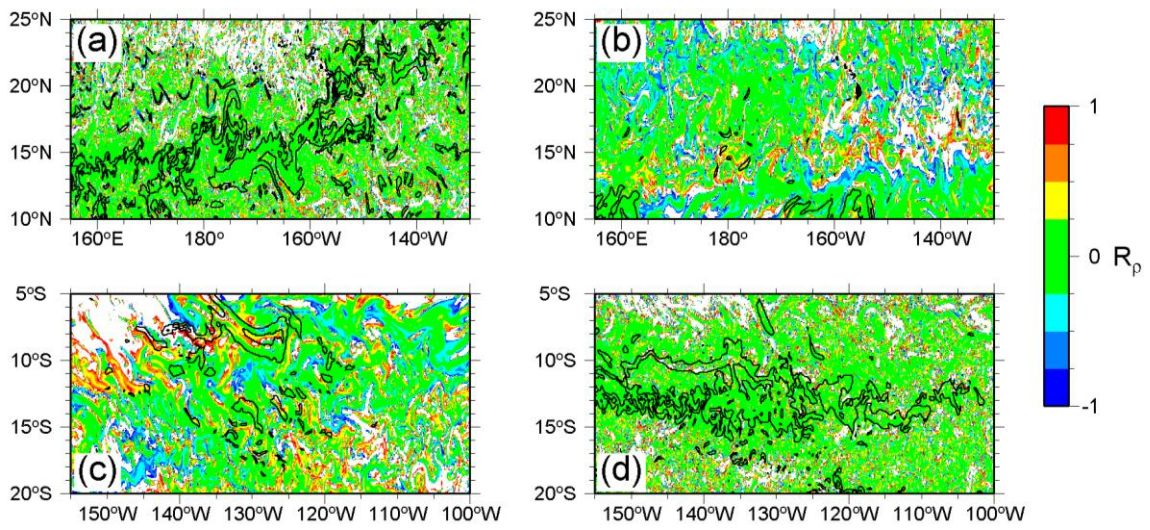


Fig. 3.18. Distribution of  $R_\rho$  (color) and contours of BLT = 20 dbar in the Northern Box (a and b) and the Southern Box (c and d) on Feb. 20 (a and c) and Aug. 19 (b and d), 2006 simulated by COCO.

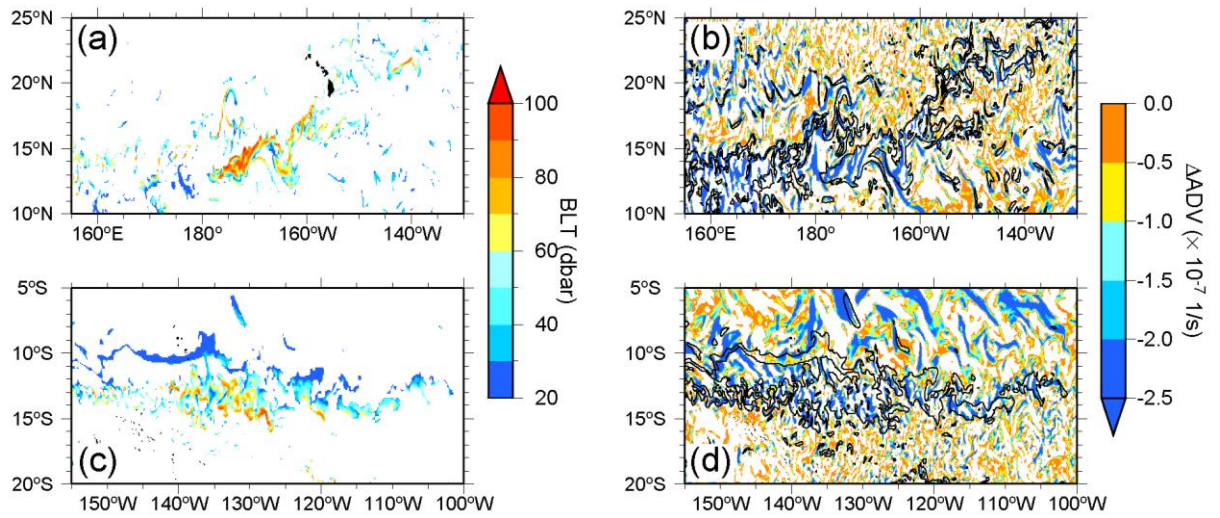


Fig. 3.19. (a and b) Distribution of BLT where  $BLT > 10\text{dbar}$  (a) and  $\Delta ADV$  where  $\Delta ADV < 0$  (b) in the Northern Box on Feb. 20, 2006 simulated by COCO. Contours in (b) indicate  $BLT = 20$  dbar. (c and d) Same as (a) and (b), respectively, but for the Southern Box on Aug. 19, 2006.

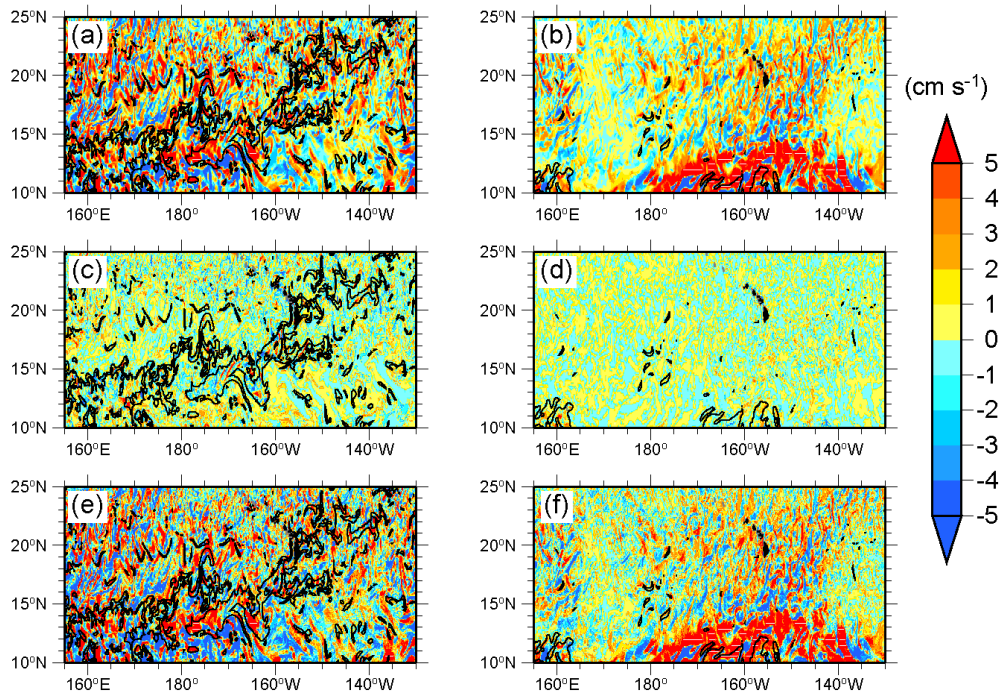


Fig. 3.20. (a, c, and e) Distribution of  $\Delta V$  (a),  $\Delta V^g$  (c), and  $\Delta V^a$  (e) in the Northern Box on Feb. 20, 2006 simulated by COCO (color). Contours indicate BLT = 20 dbar. (b, d, and f) Same as (a), (c), and (e), respectively, but for Aug. 19, 2006.

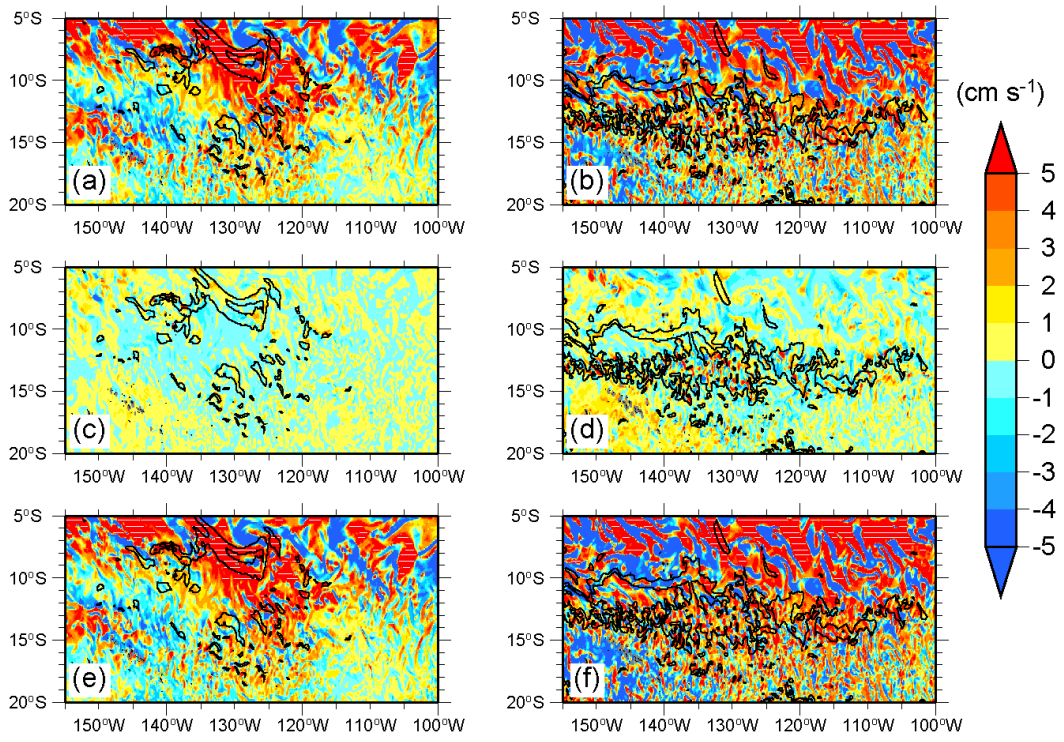


Fig. 3.21. As in Fig. 3.20 but for the Southern Box.

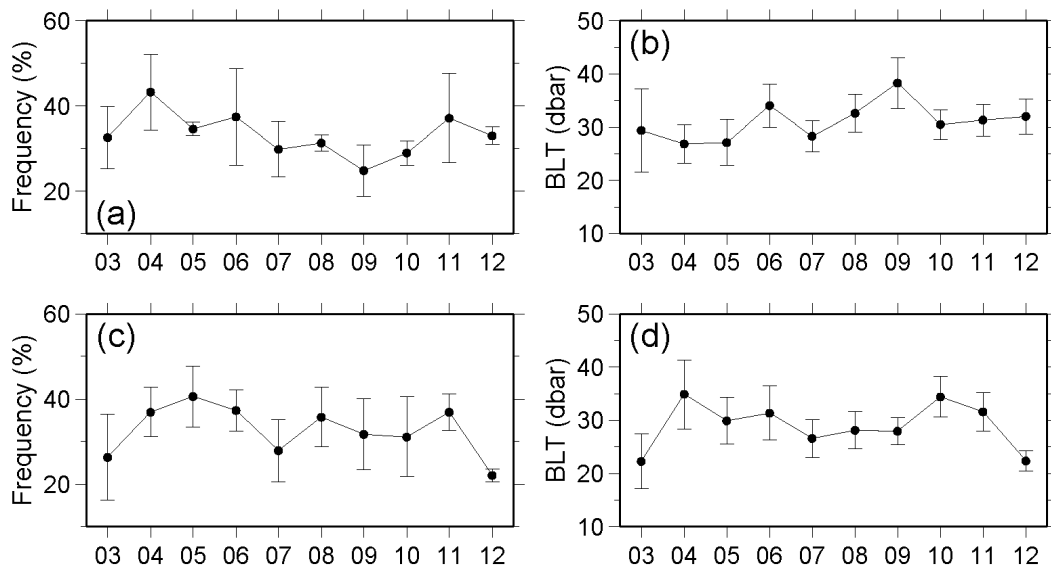


Fig. 3.22. Time series during 2003–12 of (a) frequency of Argo profiles with BLT > 10 dbar and (b) BLT from Argo profiles with BLT > 10 dbar, averaged in January–March in the SSS front in the Northern Box. Vertical bars in (a) and (b) indicate the 95% confidence interval based on the standard deviation of 3-month values of each year and from Argo profiles with BLT > 10 dbar during 3 months of each year, respectively. (c and d) Same as (a) and (b) but for July–September in the Southern Box. ©American Meteorological Society. Used with permission.

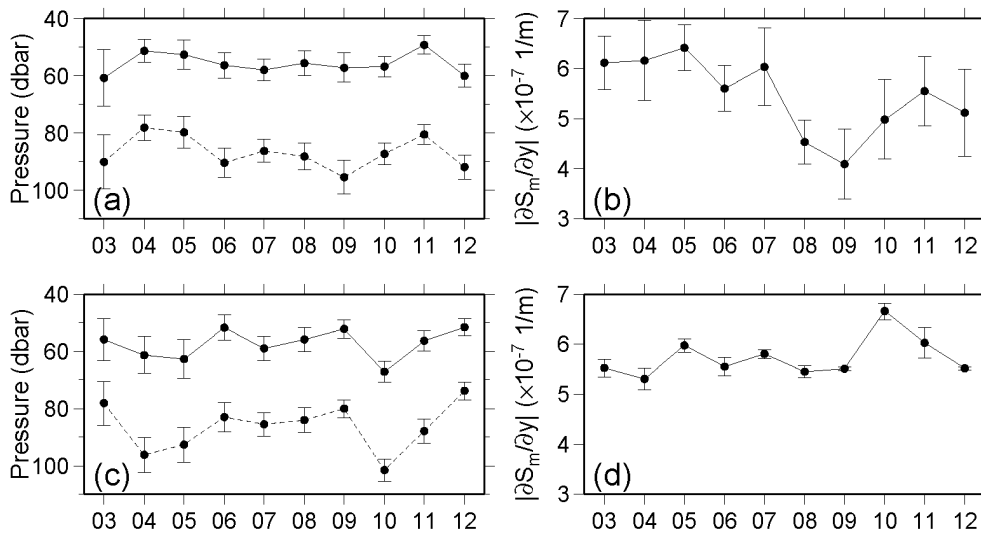


Fig. 3.23. Time series during 2003–12 of (a) MLD (solid curve) and ILD (dashed curve) from Argo profiles with BLT > 10 dbar in the SSS front and (b) meridional MLS gradient magnitude from MOAA\_GPV, averaged in January–March in the Northern Box. Vertical bars in (a) and (b) indicate the 95% confidence interval based on the standard deviation of 3-month values of each year and from Argo profiles during 3 months of each year, respectively. (c and d) Same as (a) and (b) but for July–September in the Southern Box. ©American Meteorological Society. Used with permission.

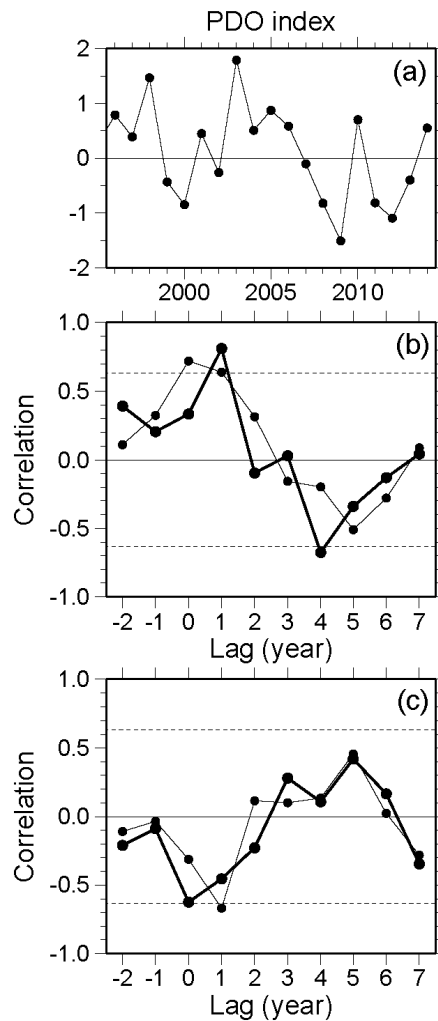


Fig. 3.24. (a) Time series of the PDO index, averaged in January–March. The PDO index is from the University of Washington website (<http://jisao.washington.edu/pdo/PDO.latest>). (b) Lag correlations between the PDO index and frequency of Argo profiles with BLT > 10 dbar, averaged in January–March in the SSS front in the Northern Box (thick curve) and meridional MLS gradient magnitude from MOAA\_GPV in the Northern Box (thin curve). (c) Lag correlations between the PDO index and BLT from Argo profiles with BLT > 10 dbar (thick curve) and ILD from Argo profiles with BLT > 10 dbar (thin curve), averaged in January–March in the SSS front in the Northern Box. A positive lag in (b) and (c) indicates that the PDO index leads. Horizontal dashed lines in (b) and (c) indicate 95% confidence value of non-correlation test based on  $t$ -distribution ( $R = 0.63$ ). ©American Meteorological Society. Used with permission.

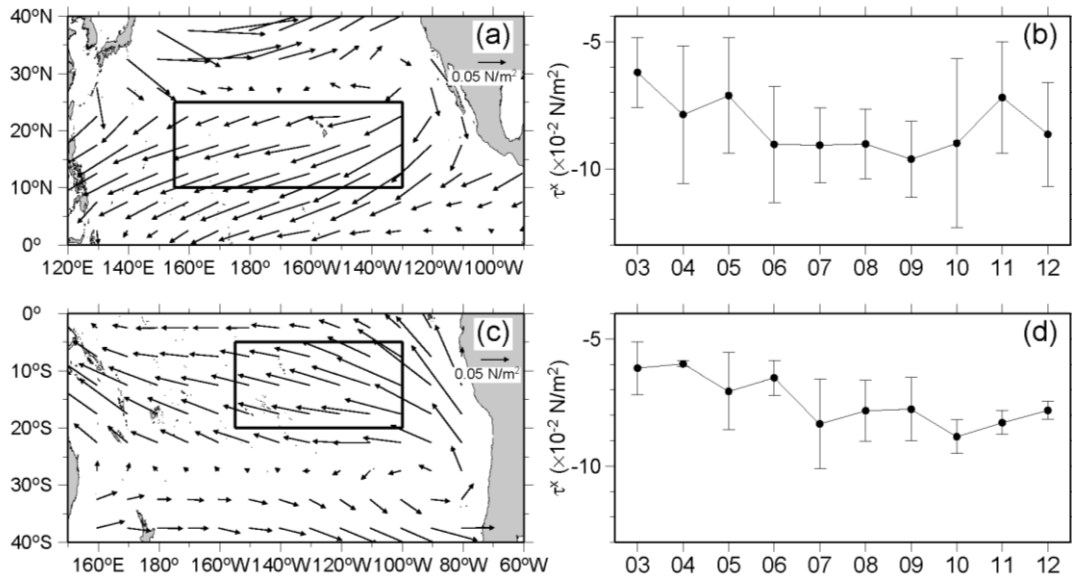


Fig. 3.25. (a and c) Distribution of wind stress during 2003–12 averaged in January–March in the North Pacific (a) and in July–September in the South Pacific. (b and d) Time series during 2003–12 of zonal wind stress averaged in January–March in the Northern Box (b) and in July–September in the Southern Box (d). Vertical bars indicate the 95% confidence interval based on the standard deviation of 3-month values of each year. ©American Meteorological Society. Used with permission.

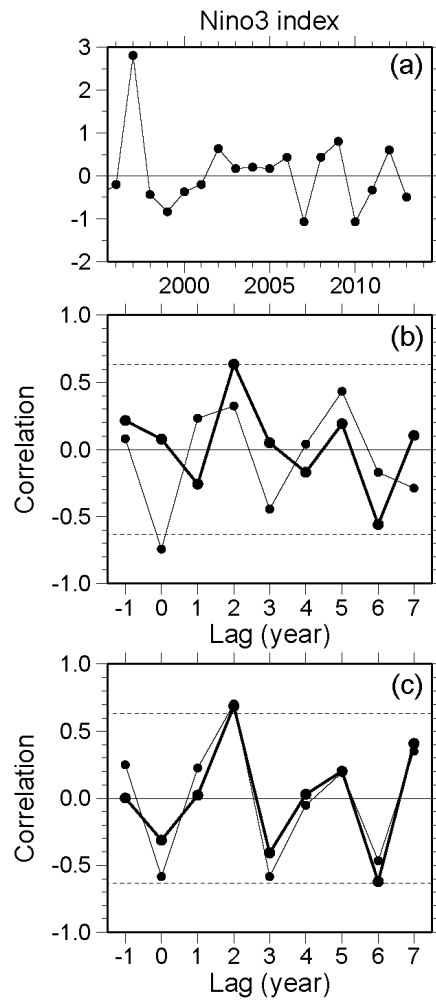


Fig. 3.26. (a) Time series of the Nino3 index, averaged in July–September. The Nino3 index is from the Japan Meteorological Agency website ([http://www.data.jma.go.jp/gmd/cpd/data/el\\_nino/index/nino3idx.html](http://www.data.jma.go.jp/gmd/cpd/data/el_nino/index/nino3idx.html)). (b) Lag correlations between the annual mean of the Nino3 index and frequency of Argo profiles with BLT > 10 dbar, averaged in July–September in the SSS front in the Southern Box (thick curve) and meridional MLS gradient magnitude from MOAA\_GPV in the Southern Box (thin curve). (c) Lag correlations between the annual mean of the Nino3 index and BLT from Argo profiles with BLT > 10 dbar (thick curve) and ILD from Argo profiles with BLT > 10 dbar (thin curve), averaged in the SSS front in the Southern Box. A positive lag in (b) and (c) indicates that the Nino3 index leads. Horizontal dashed lines in (b) and (c) indicate 95% confidence value of non-correlation test based on  $t$ -distribution ( $R = 0.63$ ). ©American Meteorological Society. Used with permission.

# Chapter 4

## General Conclusion and Discussion

### 4.1 Conclusion

In the subtropics, water is subducted from the winter mixed layer and partly advected to the tropics. It has been hypothesized that temperature and salinity anomalies subducted in the subtropics propagate to the tropics along isopycnal surfaces, modulate sea surface temperature there, and cause decadal climate variability (Gu and Philander 1997). To understand their formation, propagation, and impacts on climate variability, structure and variability of upper ocean salinity in the subtropics need to be clarified. In the subtropical Pacific, the North Pacific Tropical Water (NPTW) and the South Pacific Tropical Water (SPTW) are formed in the regions of maximum sea surface salinity (SSS). Barrier layers (BLs) are also formed in winter in association with SSS fronts located on the equator side of the SSS maxima. It has become possible to investigate seasonal and interannual salinity variation in most parts of the global ocean owing to the construction of Argo profiling float network. In this thesis, the structure and variability of NPTW and BL in the subtropical North and South Pacific were investigated mainly by analyzing Argo profiling float data.

Formation, subduction, and advection of NPTW, their interannual variability, and the associated mechanisms were investigated using gridded Argo profiling float data and various surface flux data (Chapter 2). The NPTW has two formation sites in the center of the North Pacific subtropical gyre, corresponding to two regional SSS maxima. Mixed layer salinity variations in these two NPTW formation sites were significantly different. While seasonal variation was prominent in the eastern formation site, interannual variation was dominant in the western site. The mixed layer salinity variation in the eastern site was controlled mainly by evaporation, precipitation, and entrainment of fresher water below the mixed layer, and was closely related to the

seasonal variation of the mixed layer depth. In the western site, the effect of entrainment is small due to small vertical difference in salinity across the mixed layer base, and excess evaporation over precipitation was likely to be balanced by eddy diffusion, whose strength may vary interannually in association with the Pacific Decadal Oscillation (PDO). After subduction, denser NPTW formed in the eastern site dissipated quickly, while the lighter one formed in the western site was advected westward as far as the Philippines Sea, transmitting the interannual variation of salinity away from its formation region.

Seasonal and interannual variations of BL and its formation mechanism, possibly in relation to the TW subduction, in the subtropical North and South Pacific were investigated by using raw and gridded Argo profiling float data and various surface flux data, hydrographic section data from the World Ocean Circulation Experiment Hydrographic Programme, and the output data of an ocean general circulation model (OGCM; Chapter 3). BLs detected by raw Argo profiles, which existed within the SSS front located on the equator side of SSS maxima, were thickest and most frequent in winter and had a temporal scale around 10 days, indicating their transient nature. Subsurface salinification due to the subduction of TWs and surface freshening suggested as formation mechanism of BLs by previous studies were evaluated. High salinity water within BL was not directly associated with the subduction of TWs. Meridional Ekman advection was dominant as surface freshening process, but it could not explain the seasonal variation of BLs. Temporal scale of BLs was also too short for their growth during cooling period. These results strongly suggest that BLs in the subtropical Pacific are formed mainly through tilting of the SSS front due to the poleward Ekman flow near the sea surface. This idea is supported by dominant contribution of the meridional SSS gradient to the meridional sea surface density gradient within the SSS front and the correspondence between the seasonal variations of BL and isothermal layer depth. It was also confirmed by the analysis of OGCM that the vertical shear of salinity advection within isothermal layers tends to occur where BLs are formed and that the vertical shear of flow results from that of ageostrophic one. On interannual time scale, the winter BL thickness in the North and South Pacific was related to the PDO and the El Niño-Southern Oscillation (ENSO), respectively, through their influence on the intensity of trade winds controlling isothermal layer depth.

## 4.2 Future Works

This study has revealed the significant zonal differences in the mixed layer salinity (MLS) variation and the associated mechanism within the NPTW formation region (Chapter 2; Fig. 4.1). Similar zonal difference in the SSS variation was reported in the equatorial Pacific (Delcroix and Hénin 1991); ENSO-related interannual variation is dominant in the western equatorial Pacific, while seasonal variation is dominant in the eastern equatorial Pacific. This indicates that MLS variation is significantly different both in zonal and meridional directions. Such zonal and meridional differences suggest a necessity of further regional studies on the MLS variation. Specifically, we need to clarify the contribution of horizontal and vertical processes quantitatively by using Argo data and various surface flux data in each part of the global ocean. Such studies would be useful for understanding not only climate and hydrological cycle but also SSS variations monitored by the SMOS/MIRAS and SAC-D/Aquarius satellites.

It is also indicated in this study that the subduction of TWs is not essential for the formation of BLs in the subtropical Pacific (Chapter 3; Fig. 4.2). Sprintall and Tomczak (1992) suggested that the subduction of TWs may play an important role in the maintenance of BL in the tropical region, particularly in the Atlantic where the existence of BL cannot be explained only by precipitation. The relationship between BLs in the tropical region and the subduction of TWs has not been investigated sufficiently. Such studies are needed for understanding of not only formation mechanism of BL but also its role in air-sea interaction in the tropical region.

The PDO-related spiciness anomalies propagated from NPTW formation region to the Philippines Sea (Chapter 2; Fig. 4.1). It is an important future task to examine whether these anomalies survive the intensive mixing in the Philippines Sea and how they are further advected and affect upper ocean processes in the equatorial Pacific and the Kuroshio Extension regions. On the other hand, it was also reported that the PDO-related spiciness anomalies propagated from SPTW formation region to the equatorial region (Zhang and Qu 2014). Hence, the PDO may affect the equatorial region from both hemispheres through the advection of NPTW and SPTW. It is necessary to investigate how the PDO-related spiciness anomalies affect SST in the equatorial region as a future work.

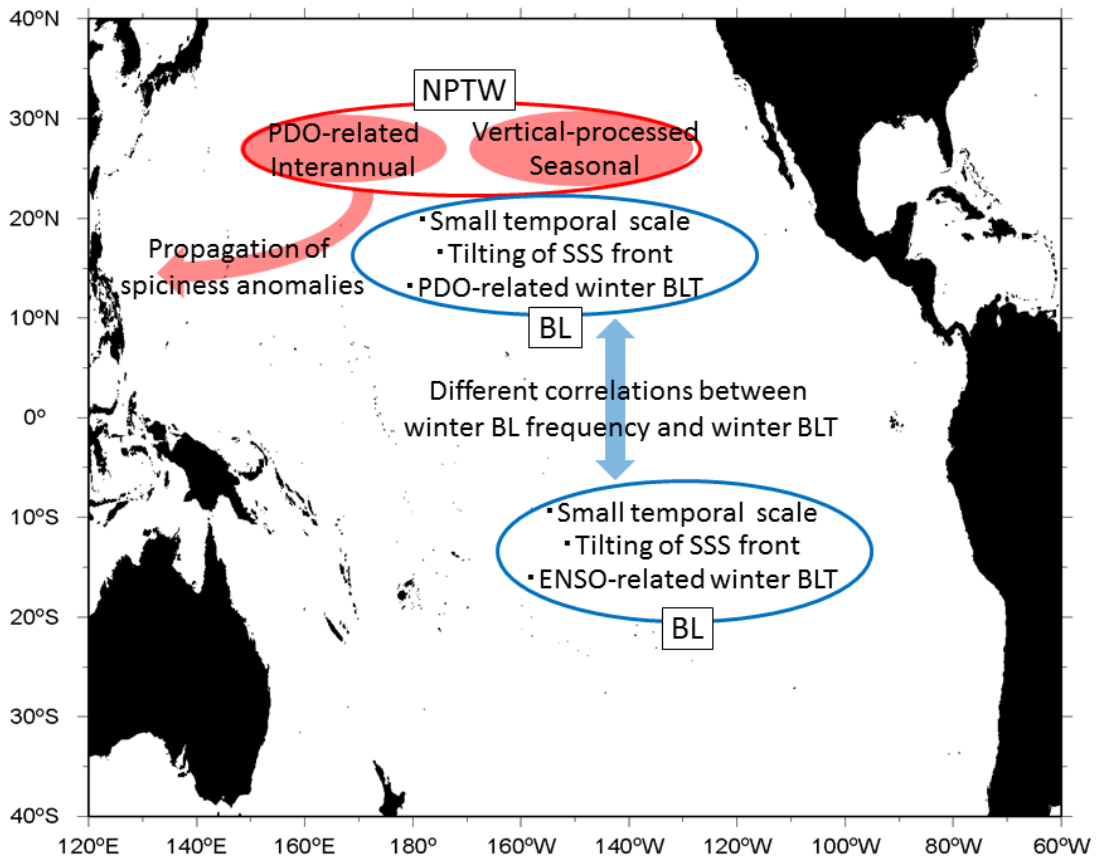


Fig. 4.1. Schematic of the results of this study.

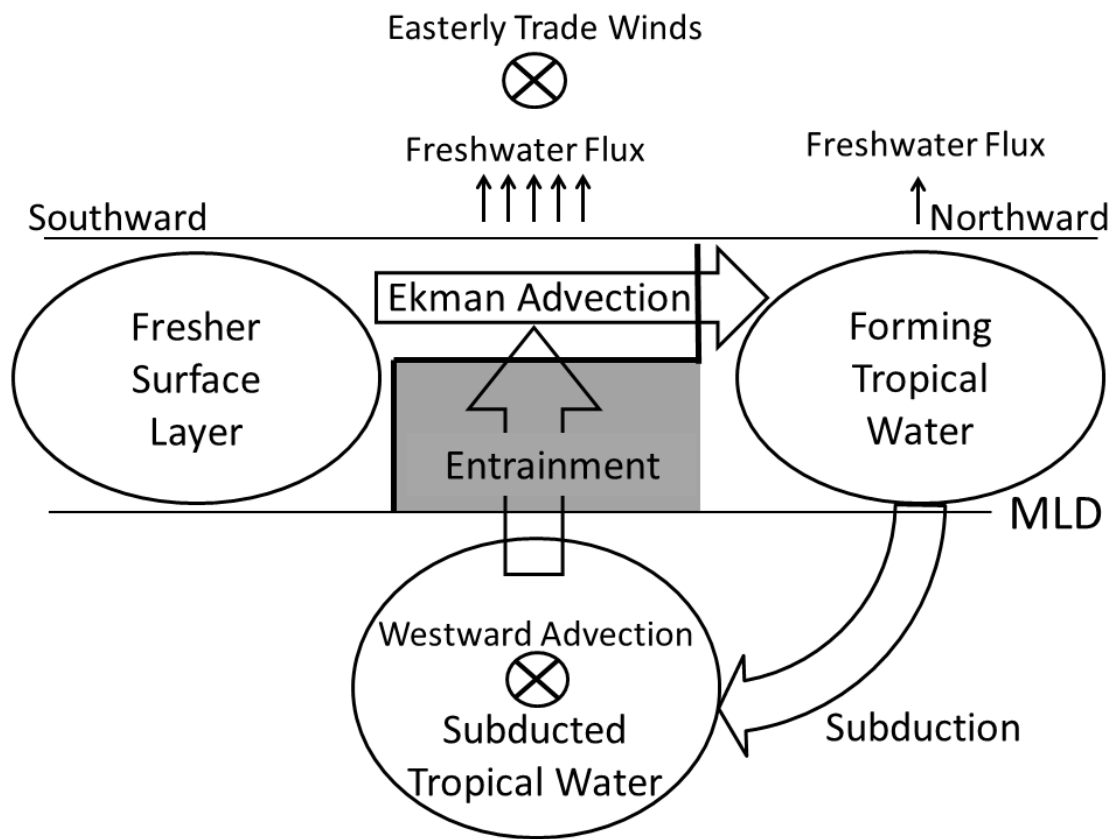


Fig. 4.2. Schematic diagram of the meridional-vertical structure of surface layer salinity and the meridional overturning circulation of TW in the subtropical North Pacific modified from Fig. 2.18. Gray shading and thick solid line indicate BL and tilted SSS front, respectively.

## Appendix

# Residual of the Mixed Layer Salinity Budget with the Usage of Various Freshwater Flux Data

In Sec. 2.4, it was discussed that the interannual variation of mixed layer salinity (MLS) in the western site of the North Pacific Tropical Water (NPTW) formation region may be controlled by eddy diffusion, based on the fact that the interannual variation of both the residual of MLS budget [ $A$ ; Eq. (2.5)] showed a positive correlation with that of eddy kinetic energy [EKE; Eq. (2.6); Fig. 2.19a] and  $-EKE \cdot \nabla^2 S$ . Here, it is assessed whether this discussion depends on the choice of various freshwater flux data or not.

In the all cases of various freshwater flux data ( $E$  from NCEP and OAFlux and  $P$  from CMAP, GPCP, and NCEP), residual  $A$  showed a similar interannual variation and a positive correlation with that of EKE (Fig. A.1). In addition, it was also highly correlated with  $-EKE \cdot \nabla^2 S$  on an interannual time scale in all cases except for the cases with precipitation from NCEP. Thus, the discussion in Sec 2.4 is not sensitive to the choice of freshwater flux data.

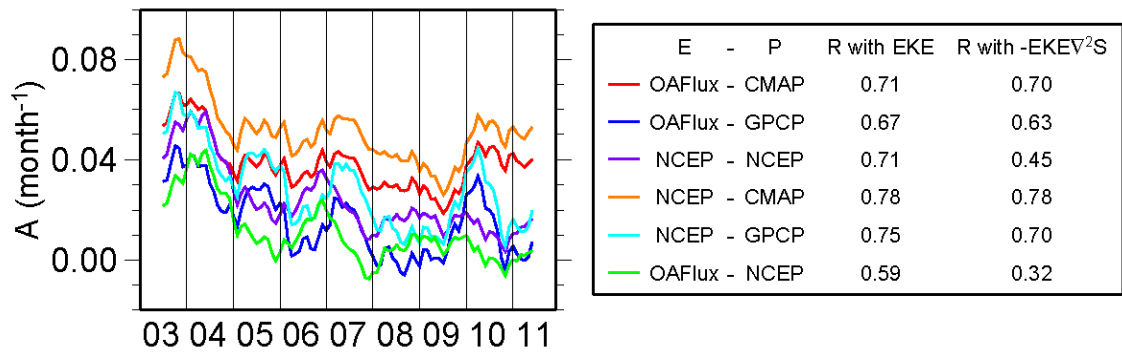


Fig. A.1. Time series of 12-month moving average in 2003–11 of  $A$  in the NW box in the cases of various freshwater flux data. Correlation coefficient  $R$  with the 12-month moving average of  $EKE$  and  $-EKE \cdot \nabla^2 S$  (Fig. 2.19a) are shown in right panel.

# Acknowledgements

First and foremost, I would like to express my gratitude to my principal advisor, Prof. E. Oka at the Atmosphere and Ocean Research Institute, The University of Tokyo for his many valuable suggestions and discussions throughout this study and over the past six years. Without his support, this study would not have been possible.

I greatly appreciate valuable comments of the examiners, Profs. T. Tozuka, Y. Masumoto, T. Hibiya, H. Hasumi, K. Iga, and E. Oka. In particular, I appreciate chief examiner, Prof. T. Tozuka, for his thorough suggestions and comments to the revision of the manuscript.

I am grateful to the members and ex-members of the Atmosphere and Ocean Research Institute, especially, Profs. I. Yasuda, H. Hasumi, S. Fujio, A. Oka, K. Tanaka, and D. Yanagimoto, and Drs. T. Kawasaki and T. Sakamoto for giving me valuable comments during our regular seminar. I also appreciate the members and ex-members of the Department of Physical Oceanography, the Atmosphere and Ocean Research Institute. Special thanks to Profs. H. Niino, K. Iga, and W. Yanase, Drs. T. Tanaka, E. Tochimoto, M. Ishizu, and S. Watanabe, Mrs. E. Fukumura, Mrs. H. Hibino, Mr. K. Sueki, Mr. K. Ando, Mr. M. Miyamoto, and Mr. Y. Goto for their continuous encouragement.

I appreciate Profs. B. Qiu, R. Lukas, and N. Schneider, and Dr. A. Belmadani at the University of Hawaii at Manoa for their lively discussion and important advices during my one-month visit to the University of Hawaii at Manoa in October 2012 under the Overseas Internship Program for Outstanding Young Earth and Planetary Researchers provided by the Department of Earth and Planetary Science, The University of Tokyo. Especially, I appreciate Profs. B. Qiu and N. Schneider for their important comments and suggestion for Chapter 2. I appreciate Prof. T. Hibiya, who operates this program.

I appreciate Drs. K. Sato, S. Kouketsu, S. Hosoda, M. Nonaka, and T. Hasegawa at JAMSTEC for their lively discussion and important advices. Especially, I appreciate

Dr. K. Sato for her helpful suggestion and discussion for Chapter 3.

I also thank participants at the "Research Meetings on Air-Sea Interaction" in 2011-15 held as a part of the Collaborative Research Program of Hydrospheric Atmospheric Research Center, Nagoya University, especially, Emeritus Prof. K. Takeuchi and Prof. Y. Tanimoto at Hokkaido University, Profs. T. Suga and S. Sugimoto at the Tohoku University, Profs. M. Kubota, K. Kutsuwada, and K. Uehara at Tokai University, Profs. N. Iwasaka and F. Kobashi at Tokyo University of Marine Science and Technology, Profs. Y. Yoshikawa and M. Konda at Kyoto University, and Prof. K. Ichikawa at Kyusyu University for their valuable comments and discussion.

I also thank all the scientists and crews who participated in KH-11-08, KT-12-16, KH-13-3, KS-14-7, and KS-15-14 cruise. Experiences on these cruises have greatly stimulated me. In particular, my first cruise greatly motivated me to be an oceanographer. I would like to express my gratitude to the late Prof. M. Kawabe who was the chief scientist of that cruise.

Part of this study was supported by the Sasakawa Scientific Research Grant from The Japan Science Society and by JSPS Research Fellowship.

## References

- Adler, R. F., and Coauthors, 2003: The Version-2 Global Precipitation Climatology Project (GPCP) monthly precipitation analysis (1979–present). *J. Hydrometeor.*, **4**, 1147–1167.
- Akima, H., 1970: A new method for interpolation and smooth curve fitting based on local procedures. *J. Assoc. Comput. Mech.*, **17**, 589–602.
- Ando, K., and M. J. McPhaden, 1997: Variability of surface layer hydrography in the tropical Pacific Ocean. *J. Geophys. Res.*, **102** (C10), 23 063–23 078.
- Balaguru, K., P. Chang, R. Saravanan, L. R. Leung, Z. Xu, M. Li, and J.-S. Hsieh, 2012a: Ocean barrier layers' effect on tropical cyclone intensification. *Proc. Natl. Acad. Sci. USA*, **109**, 14 343–14 347, doi:10.1073/pnas.1201364109.
- Bingham, F.M., T. Suga, and K. Hanawa, 2002: Origin of waters observed along 137E. *J. Geophys. Res.*, **107** (C7), <http://dx.doi.org/10.1029/2000JC000722>.
- Bingham, F. M., G. R. Foltz, and M. J. McPhaden, 2010: Seasonal cycles of surface layer salinity in the Pacific Ocean. *Ocean Sci.*, **6**, 775–787, doi:10.5194/os-6-775-2010.
- Bingham, F. M., G. R. Foltz, and M. J. McPhaden, 2012: Characteristics of the seasonal cycle of surface layer salinity in the global ocean. *Ocean Sci.*, **8**, 915–929, doi:10.5194/os-8-915-2012.
- Bosc, C., T. Delcroix, and C. Maes, 2009: Barrier layer variability in the western Pacific warm pool from 2000 to 2007. *J. Geophys. Res.*, **114**, C06023, doi:10.1029/2008JC005187.
- Boyer, T. P., J. I. Antonov, S. Levitus, and R. Locarnini, 2005: Linear trends of salinity for the world ocean, 1955–1998. *Geophys. Res. Lett.*, **32**, L01604, doi:10.1029/2004GL021791.
- Cannon, G. A., 1966: Tropical waters in the western Pacific Ocean, August–September 1957. *Deep-Sea Res.*, **13**, 1139–1148.

- Carton, J. A., S. A. Grodsky, and H. Liu, 2008: Variability of the oceanic mixed layer, 1960–2004. *J. Climate*, **21**, 1029–1047.
- Conkright, M. E., R. A. Locarnini, H. E. Garcia, T. D. O'Brien, T. P. Boyer, C. Stephens, and J. I. Antonov, 2002: World Ocean Atlas 2001: Objective Analyses, Data Statistics, and Figures. *CD-ROM Documentation*, **17**, NOAA Silver Spring, Md.
- Cronin, M. F., and M. J. McPhaden, 1998: Upper ocean salinity balance in the western equatorial Pacific. *J. Geophys. Res.*, **103**, 27 567–27 587.
- Cronin, M. F., and M. J. McPhaden, 2002: Barrier layer formation during westerly wind bursts. *J. Geophys. Res.*, **107** (C12), doi:10.1029/2001JC001171.
- Curry, R., B. Dickson, and I. Yashayaev, 2003: A change in the freshwater balance of the Atlantic Ocean over the past four decades. *Nature*, **426**, 826–829.
- de Boyer Montégut, C., J. Mignot, A. Lazar, and S. Cravatte, 2007: Control of salinity on the mixed layer depth in the World Ocean: 1. General description. *J. Geophys. Res.*, **112**, C06011, doi:10.1029/2006JC003953.
- de Boyer Montégut, C., G. Madec, A. S. Fischer, A. Lazar, and D. Iudicone, 2004: Mixed layer depth over the global ocean: An examination of profile data and a profile-based climatology. *J. Geophys. Res.*, **109**, C12003, doi:10.1029/2004JC002378.
- Delcroix, T., and C. Hénin, 1991: Seasonal and interannual variations of sea surface salinity in the tropical Pacific Ocean. *J. Geophys. Res.*, **96**, 22 135–22 150.
- Delcroix, T., and J. Picaut, 1998: Zonal displacement of the western equatorial Pacific fresh pool. *J. Geophys. Res.*, **103**, 1087–1098.
- Delcroix, T., and M. McPhaden, 2002: Interannual sea surface salinity and temperature changes in the western Pacific warm pool during 1992–2000. *J. Geophys. Res.*, **107** (C12), doi:10.1029/2001JC000862.
- Delcroix, T., C. Henin, V. Porte, and P. Arkin, 1996: Precipitation and sea surface salinity in the tropical Pacific Ocean. *Deep-Sea Res.*, **43**, 1123–1141.
- Delcroix, T., M. J. McPhaden, A. Dessier, and Y. Gouriou, 2005: Time and space scales for sea surface salinity in the tropical oceans. *Deep-Sea Res. I*, **52**, 787–813.
- Deser, C. M., A. Alexander, and M. S. Timlin, 1996: Upper-ocean thermal variations in the North Pacific during 1970–1991. *J. Climate*, **9**, 1840–1855.
- Dessier, A., and J. R. Donguy, 1994: The sea surface salinity in the tropical Atlantic

- between 10°S and 30°N—Seasonal and interannual variations (1977–1989). *Deep-Sea Res.*, **41**, 81–100.
- Dong, S., S. L. Garzoli, and M. Baringer, 2009: An assessment of the seasonal mixed layer salinity budget in the Southern Ocean. *J. Geophys. Res.*, **114**, C12001, doi:10.1029/2008JC005258.
- Donguy, J. R., and G. Meyers, 1996: Seasonal variations of sea-surface salinity and temperature in the tropical Indian Ocean. *Deep-Sea Res.*, **43**, 117–138.
- Durack, P. J., and S. E. Wijffels, 2010: Fifty-year trends in global ocean salinities and their relationship to broad-scale warming. *J. Climate*, **23**, 4342–4362.
- Feng, M., P. Hacker, and R. Lukas, 1998: Upper ocean heat and salt balances in response to a westerly wind burst in the western equatorial Pacific during TOGA COARE. *J. Geophys. Res.*, **103**, 10 289–10 311.
- Ffield, A., and A. L. Gordon, 1992: Vertical mixing in the Indonesian thermocline. *J. Phys. Oceanogr.*, **22**, 184–195.
- Fine, R. A., R. Lukas, F. M. Bingham, M. J. Warner, and R. H. Gammon, 1994: The western equatorial Pacific: A water mass crossroads. *J. Geophys. Res.*, **99**, 25 063–25 080.
- Fisher, R. A., 1950: Statistical methods for research workers. 11th ed., Edinburgh: Oliver & Boyd.
- Foltz, G. R., and M. J. McPhaden, 2005: Mixed layer heat balance on intraseasonal time scales in the northwestern tropical Atlantic Ocean. *J. Climate*, **18**, 4168–4184.
- Foltz, G. R., and M. J. McPhaden, 2008: Seasonal mixed layer salinity balance of the tropical North Atlantic Ocean. *J. Geophys. Res.*, **113**, C02013, doi:10.1029/2007JC004178.
- Foltz, G. R., and M. J. McPhaden, 2009: Impact of barrier layer thickness on SST in the central tropical North Atlantic. *J. Climate*, **22**, 285–299.
- Foltz, G. R., S. A. Grodsky, J. A. Carton, and M. J. McPhaden, 2004: Seasonal salt budget of the northwestern tropical Atlantic Ocean along 38°W. *J. Geophys. Res.*, **109**, C03052, doi:10.1029/2003JC002111.
- Godfrey, J. S., and E. J. Lindstrom, 1989: The heat-budget of the equatorial western Pacific surface mixed layer. *J. Geophys. Res.*, **94** (C6), 8007–8017.
- Gu, D. F., and S. G. F. Philander, 1997: Interdecadal climate variability that depends on exchanges between the tropics and extratropics. *Science*, **275**, 805–807.

- Hasumi, H., 2006: CCSR Ocean Component Model (COCO) version 4.0, *Rep. 25*, Cent. for Clim. Syst. Res., Univ. of Tokyo, Chiba, Japan.
- Hayes, S. P., P. Chang, and M. J. McPhaden, 1991: Variability of the sea surface temperature in the eastern equatorial Pacific during 1986-1988. *J. Geophys. Res.*, **96**, 10 553–10 566.
- Helm, K. P., N. L. Bindoff, and J. A. Church, 2010: Changes in the global hydrological - cycle inferred from ocean salinity. *Geophys. Res. Lett.*, **37**, L18701, doi:10.1029/2010GL044222.
- Hosoda, S., T. Ohira, and T. Nakamura, 2008: A monthly mean dataset of global oceanic temperature and salinity derived from Argo float observations. *JAMSTEC Rep. Res. Dev.*, **8**, 47–59.
- Hosoda, S., T. Suga, N. Shikama, and K. Mizuno, 2009: Global surface layer salinity change detected by Argo and its implication for hydrological cycle intensification. *J. Oceanogr.*, **65**, 579–586.
- Huffman, G. J., and Coauthors, 1997: The Global Precipitation Climatology Project (GPCP) combined precipitation dataset. *Bull. Amer. Meteor. Soc.*, **78**, 5–20.
- Johnson, G. C., and M. J. McPhaden, 1999: Interior pycnocline flow from the subtropical to the equatorial Pacific Ocean. *J. Phys. Oceanogr.*, **29**, 3073–3089.
- Kashino, Y., M. Aoyama, T. Kawano, N. Hendiarti, Syaefudi, Y. Anantasena, K. Muneyama, and H. Watanabe, 1996: The water masses between Mindanao and New Guinea. *J. Geophys. Res.*, **101**, 12 391–12 400.
- Katsura, S., E. Oka, T. Sato, 2015: Formation Mechanism of Barrier Layer in the Subtropical Pacific. *J. Phys. Oceanogr.*, **45**, 2790–2805, doi: 10.1175/JPO-D-15-0028.1
- Katsura, S., E. Oka, B. Qiu, and N. Schneider, 2013: Formation and subduction of North Pacific tropical water and their interannual variability. *J. Phys. Oceanogr.*, **43**, 2400–2415.
- Kerr, Y. H., P. Waldteufel, J.-P. Wigneron, J.-M. Martinuzzi, J. Font, and M. Berger, 2001: Soil moisture retrieval from space: The Soil Moisture and Ocean Salinity (SMOS) mission. *IEEE Trans. Geosci. Remote Sens.*, **39**, 1729– 1735.
- Kessler, W. S., 1999: Interannual variability of the subsurface high salinity tongue south of the equator at 1658E. *J. Phys. Oceanogr.*, **29**, 2038–2049.
- Kistler, R., and Coauthors, 2001: The NCEP–NCAR 50-Year Reanalysis: Monthly

- means CD-ROM and documentation. *Bull. Amer. Meteor. Soc.*, **82**, 247–267.
- Kolodziejczyk, N., and F. Gaillard, 2012: Observation of spiciness interannual variability in the Pacific pycnocline. *J. Geophys. Res.*, **117**, C12018, doi:10.1029/2012JC008365.
- Large, W. G., and S. G. Yeager, 2009: The global climatology of an interannually varying air-sea flux data set. *Climate Dyn.*, **33**, 341–364.
- Le Vine, D. M., G. S. E. Lagerloef, F. R. Colomb, S. H. Yueh, and F. A. Pellerano, 2007: Aquarius: An instrument to monitor sea surface salinity from space. *IEEE Trans. Geosci. Remote Sensing*, **45**, 2040–2050.
- Levitus, S., 1982: Climatological atlas of the world ocean, *NOAA Prof. Pap.*, **13**, 173 pp., U.S. Dep. of Commer., Washington, D. C., 1982.
- Levitus, S., R. Burgett, and T. P. Boyer, 1994: World Ocean Atlas 1994, Vol. 3: *Salinity*. NOAA/NESDIS/NODC, 99 pp.
- Li, Y., and F. Wang, 2012: Spreading and salinity change of North Pacific tropical water in the Philippine Sea. *J. Oceanogr.*, **68**, 439–452.
- Lindstrom, E., F. Bryan, and R. Schmitt, 2015: SPURS: Salinity Processes in the Upper-ocean Regional Study—The North Atlantic Experiment Introduction. *Oceanography*, **28**, 14–19, doi:10.5670/oceanog.2015.01.
- Liu, Z., 1999: Forced planetary wave response in a thermocline gyre. *J. Phys. Oceanogr.*, **29**, 1036–1055.
- Lukas, R., 2001: Freshening of the upper thermocline in the North Pacific subtropical gyre associated with decadal changes of rainfall. *Geophys. Res. Lett.*, **28**, 3485–3488.
- Lukas, R., and E. Lindstrom, 1991: The mixed layer in the western equatorial Pacific Ocean. *J. Geophys. Res.*, **96**, 3343–3357.
- Lukas, R., E. Firing, P. Hacker, P. L. Richardson, C. A. Collins, R. Fine, and R. Gammon, 1991: Observations of the Mindanao Current during the Western Equatorial Pacific Ocean Circulation Study. *J. Geophys. Res.*, **96**, 7089–7104.
- Maes, C., and S. Belamari, 2011: On the Impact of Salinity Barrier Layer on the Pacific Ocean Mean State and ENSO. *SOLA*, **7**, 97–100.
- Mantua, N. J., S. R. Hare, Y. Zhang, J. M. Wallace, and R. C. Francis, 1997: A Pacific interdecadal climate oscillation with impacts on salmon production. *Bull. Amer. Meteor. Soc.*, **78**, 1069–1079.

- Masson, S., J.-P. Boulanger, C. Menkes, P. Delecluse, and T. Yamagata, 2004: Impact of salinity on the 1997 Indian Ocean dipole event in a numerical experiment. *J. Geophys. Res.*, **109**, C02002, doi:10.1029/2003JC001807
- Masuzawa, J., 1967: An oceanographic section from Japan to New Guinea at 137°E in January 1967. *Oceanogr. Mag.*, **19**, 95–118.
- Mignot, J., C. de Boyer Montégut, and M. Tomczak, 2009: On the porosity of barrier layers. *Ocean Sci.*, **5**, 379–387.
- Mignot, J., A. Lazar, and M. Lacarra, 2012: On the formation of barrier layers and associated vertical temperature inversions: A focus on the northwestern tropical Atlantic. *J. Geophys. Res.*, **117**, C02010, doi:10.1029/2011JC007435.
- Mignot, J., C. de Boyer Montégut, A. Lazar, and S. Cravatte, 2007: Control of salinity on the mixed layer depth in the World Ocean: 2. Tropical areas. *J. Geophys. Res.*, **112**, C10010, doi:10.1029/2006JC003954.
- Munk, W., 1981: Internal waves and small-scale processes. *Evolution of Physical Oceanography*, B. A. Warren and C. Wunsch, Eds., The MIT Press, 264–291.
- Nitta, T., and S. Yamada, 1989: Recent warming of tropical sea surface temperature and its relationship to the Northern Hemisphere circulation. *J. Meteorol. Soc. Jpn.*, **67**, 375–382.
- Nonaka, M., and H. Sasaki, 2007: Formation mechanism for isopycnal temperature–salinity anomalies propagating from the eastern South Pacific to the equatorial region. *J. Climate*, **20**, 1305–1315.
- O’Connor, B. M., R. A. Fine, and D. B. Olson, 2005: A global comparison of subtropical underwater formation rates. *Deep-Sea Res.*, **52**, 1569–1590.
- O’Connor, B. M., R. A. Fine, K. A. Maillet, and D. B. Olson, 2002: Formation rates of subtropical underwater in the Pacific Ocean. *Deep-Sea Res.*, **49**, 1571–1590.
- Oka, E., 2009: Seasonal and interannual variation of North Pacific Subtropical Mode Water in 2003–2006. *J. Oceanogr.*, **65**, 151–164.
- Oka, E., and B. Qiu, 2012: Progress of North Pacific mode water research in the past decade. *J. Oceanogr.*, **68**, 5–20.
- Oka, E., T. Suga, and L. D. Talley, 2007: Temporal variability of winter mixed layer in the mid- to high-latitude North Pacific. *J. Oceanogr.*, **63**, 293–307.
- Oka, E., S. Kouketsu, K. Toyama, K. Uehara, T. Kobayashi, S. Hosoda, and T. Suga, 2011: Formation and Subduction of Central Mode Water Based on Profiling Float

- Data, 2003–08. *J. Phys. Oceanogr.*, **41**, 113-129.
- Qiu, B., and T.M. Joyce, 1992: Interannual variability in the mid- and low-latitude western North Pacific. *J. Phys. Oceanogr.*, **22**, 1062-1079.
- Qiu, B., and S. Chen, 2013: Concurrent decadal mesoscale eddy modulations in the western North Pacific subtropical gyre. *J. Phys. Oceanogr.*, **42**, 344-358.
- Qu, T., H. Mitsudera, and T. Yamagata, 1999: A climatology of the circulation and water mass distribution near the Philippine Coast. *J. Phys. Oceanogr.*, **29**, 1488–1505.
- Qu, T., T. Song, and C. Maes, 2014: Sea surface salinity and barrier layer variability in the equatorial pacific as seen from Aquarius and Argo. *J. Geophys. Res.*, **119**, 15–29, doi:10.1002/2013JC009375.
- Qu, T., L. Zhang, and N. Schneider, 2016: North Atlantic Subtropical Underwater and Its Year-to-Year Variability in Annual Subduction Rate during the Argo Period. *J. Phys. Oceanogr.*, **46**, 1901-1916, doi: 10.1175/JPO-D-15-0246.1
- Ren, L., and S. C. Riser, 2009: Seasonal salt budget in the northeast Pacific Ocean. *J. Geophys. Res.*, **114**, C12004, doi:10.1029/2009JC005307.
- Ren, L., and S. C. Riser, 2010: Observations of decadal time scale salinity changes in the subtropical thermocline of the North Pacific Ocean. *Deep-Sea Res. II*, **57**, 1161–1170.
- Ren, L., K. Speer, and E. P. Chassignet, 2011: The mixed layer salinity budget and sea ice in the Southern Ocean. *J. Geophys. Res.*, **116**, C08031, doi:10.1029/2010JC006634.
- Roemmich, D., and J. Gilson, 2009: The 2004–2008 mean and annual cycle of temperature, salinity, and steric height in the global ocean from the Argo Program. *Prog. Oceanogr.*, **82**, 81–100.
- Roemmich, D., S. Riser, R. Davis, and Y. Desaubies, 2004: Autonomous profiling floats: Workhorse for broad-scale observations. *Mar. Technol. Soc. J.*, **38**, 21–29, doi:10.4031/002533204787522802.
- Roemmich, D., O. Boebel, Y. Desaubies, H. Freeland, B. King, PY. LeTraon, R. Molinari, WB. Owens, S. Riser, U. Send, K. Takeuchi, and S. Wijffels, 2001: Argo: the global array of profiling floats. In: Koblinsky CJ, Smith NR (eds) Observing the oceans in the 21st century. *GODAE Project Office, Bureau of Meteorology, Melbourne*, pp 248–258.

- Sasaki, Y. N., N. Schneider, N. Maximenko, and K. Lebedev, 2010: Observational evidence for propagation of decadal spiciness anomalies in the North Pacific. *Geophys. Res. Lett.*, **37**, L07708, doi:10.1029/2010GL042716.
- Sato, K., and T. Suga, 2009: Structure and modification of the South Pacific Eastern Subtropical Mode Water. *J. Phys. Oceanogr.*, **39**, 1700–1714.
- Sato, K., T. Suga, and K. Hanawa, 2004: Barrier layer in the North Pacific subtropical gyre. *Geophys. Res. Lett.*, **31**, L05301, doi:10.1029/2003GL018590.
- Sato, K., T. Suga, and K. Hanawa, 2006: Barrier layers in the subtropical gyres of the world's oceans. *Geophys. Res. Lett.*, **33**, L08603, doi:10.1029/2005GL025631.
- Schmitt R. W., 1995: The ocean component of the global water cycle. *Rev. Geophys.*, **33** (S1), 1395–1410.
- Schneider, N., 2004: The response of the tropical climate to the equatorial emergence of spiciness anomalies. *J. Climate*, **17**, 1083–1095.
- Schneider, N., A. J. Miller, M. A. Alexander, and C. Deser, 1999: Subduction of decadal North Pacific temperature anomalies: Observations and dynamics. *J. Phys. Oceanogr.*, **29**, 1056–1070.
- Segschneider, J., M. Balmaseda, and D. L. T. Anderson, 2000: Anomalous temperature and salinity variations in the tropical Atlantic: Possible causes and implications for the use of altimeter data. *Geophys. Res. Lett.*, **27**, 2281–2284.
- Sprintall, J., and M. Tomczak, 1992: Evidence of the barrier layer in the surface layer of the tropics. *J. Geophys. Res.*, **97** (C5), 7305–7316.
- Sprintall, and M. J. McPhaden, 1994: Surface layer variations observed in multiyear time series measurements from the western equatorial Pacific. *J. Geophys. Res.*, **99**, 963–979.
- Steele, M., R. Morley, and W. Ermold, 2001: PHC: A global ocean hydrography with a high-quality Arctic Ocean. *J. Climate*, **14**, 2079–2087.
- Suga, T., A. Kato, and K. Hanawa, 2000: North Pacific Tropical Water: Its climatology and temporal changes associated with the climate regime shift in the 1970s. *Prog. Oceanogr.*, **47**, 223–256.
- Suga, T., K. Motoki, Y. Aoki, and M. A. Macdonald, 2004: The North Pacific climatology of winter mixed layer and mode waters. *J. Phys. Oceanogr.*, **34**, 3–22.
- Talley, L., G. Pickard, W. Emery, and J. Swift, 2011: *Descriptive Physical Oceanography: An Introduction*. Academic Press.

- Tippins, D., and M. Tomczak, 2003: Meridional Turner angles and density compensation in the upper ocean. *Ocean Dyn*, **53**, 332–342.
- Trenberth, K.E., 1990: Recent observed interdecadal climate changes in the Northern Hemisphere. *Bull. Am. Meteorol. Soc.*, **71**, 988–993.
- Tsuchiya, M., 1968: Upper waters of the intertropical Pacific Ocean. *Johns Hopkins Oceanographic Studies*, No. 4, Johns Hopkins University Press, 50 pp.
- Veneziani, M., A. Griffa, Z. Garraffo, and J. A. Menza, 2014: Barrier Layers in the Tropical South Atlantic: Mean Dynamics and Submesoscale Effects. *J. Phys. Oceanogr.*, **44**, 265–288.
- Vialard, J., and P. Delecluse, 1998a: An OGCM study for the TOGA decade. Part I: Role of salinity in the physics of the western Pacific fresh pool. *J. Phys. Oceanogr.*, **28**, 1071–1088.
- Vialard, J., and P. Delecluse, 1998b: An OGCM study for the TOGA decade. Part II: Barrier-layer formation and variability. *J. Phys. Oceanogr.*, **28**, 1089–1106.
- Wang, W., and M. J. McPhaden, 2000: The surface-layer heat balance in the equatorial Pacific Ocean. Part II: Interannual variability. *J. Phys. Oceanogr.*, **30**, 2989–3008.
- Wong, A. P. S., and G. C. Johnson, 2003: South Pacific Eastern Subtropical Mode Water. *J. Phys. Oceanogr.*, **33**, 1493–1509.
- Wong, A. P. S., N. L. Bindoff, and J. A. Church, 1999: Large - scale freshening of intermediate waters in the Pacific and Indian Oceans. *Nature*, **400**, 440–443.
- Xie, P., and P. A. Arkin, 1996: Analyses of global monthly precipitation using gauge observations, satellite estimates, and numerical model predictions. *J. Clim.*, **9**, 840–858.
- Xie, P., and P. A. Arkin, 1997: A 17-year monthly analysis based on gauge observations, satellite estimates and numerical model outputs. *Bull. Am. Meteorol. Soc.*, **78**, 2539–2558.
- Yu, L., 2011: A global relationship between the ocean water cycle and near-surface salinity. *J. Geophys. Res.*, **116**, C10025, doi:10.1029/2010JC006937.
- Yu, L., and R. A. Weller, 2007: Objectively Analyzed air - sea heat Fluxes (OAFlux) for the global ocean. *Bull. Am. Meteorol. Soc.*, **88**, 527–539.
- Yu, L., X. Jin, and R. Weller, 2008: Multidecade global flux datasets from the Objectively Analyzed Air - sea Fluxes (OAFlux) Project: Latent and sensible heat fluxes, ocean evaporation, and related surface meteorological variables. *OAFlux*

*Proj. Tech. Rep. OA - 2008 - 01*, 64 pp., Woods Hole Oceanogr. Inst., Woods Hole, Mass.

Zhang, L., and T. Qu, 2014: Low-frequency variability of South Pacific Tropical Water from Argo, *Geophys. Res. Lett.*, **41**, 2441–2446.

Zhurbas, V., and I. S. Oh, 2004: Drifter-derived maps of lateral diffusivity in the Pacific and Atlantic Oceans in relation to surface circulation patterns. *J. Geophys. Res.*, **109**, C05015, doi:10.1029/2003JC002241.